

POLITECNICO DI TORINO
Department of Energy - DENERG



Master Thesis in Electrical Engineering

Sensorless control of PM-assisted SyR motors

Author

Salvatore Domenico Mistretta

Supervisor

Prof. Gianmario Pellegrino

Advisor

Anantaram Varatharajan

March 2021

Abstract

During the last 50 years the global electricity consumption has grown by four times. Many sectors are involved in this trend: industrial, residential, transport, commercial, public services and so on. Following this trend, the global policy makers are encouraging the replacement of direct online low efficiency motors with variable speed drives of higher efficiency.

Moreover, all manufactures are moving on reduction of final price of VSD: the elimination of the speed/position transducer and the use of ferrite permanent magnets permit to achieve this target, improving also reliability.

This thesis discusses a sensorless controlled permanent magnet (PM)-assisted Synchronous Reluctance (SyR) motor drive, for general purpose variable speed applications. The sensorless control method is based on two stages: I-f control and sensorless FOC. The former is an open-loop speed control, used only to start and stop the drive, where the amplitude and the frequency of the imposed reference current vector are properly set: constant amplitude and ramp variation frequency. The latter is activated when motor speed is higher than a fixed threshold. It is a sensorless field oriented control (FOC) where the speed and position feedback are estimated by a flux and position observer based on the flux cross product sensorless method. In order to ensure a smooth transition from one speed region to the other, some precautions are adopted.

The developed sensorless techniques are fully validated with simulation and experimental results on ABB motor: in particular, they show good performance and robustness both at no load and under rated load.

Contents

1	Introduction	1
1.1	Global electricity consumption	1
1.2	Classification of motor types	2
1.3	Synchronous machines	2
1.4	PM-assisted synchronous reluctance motor	5
1.5	Control of AC motor drives	8
1.6	Goal of master thesis	10
2	Literature study	11
2.1	Why sensorless control?	11
2.2	Mathematical model of a PM-assisted SyR machine	12
2.3	Classification of sensorless control	14
2.4	Fundamental model sensorless techniques	15
2.4.1	Flux cross product method	15
2.4.2	Active Flux	16
2.4.3	Extended EMF	17
2.5	Saliency based sensorless techniques	19
2.5.1	Pulsating HF voltage injection	20
2.6	Summary	22
3	Proposed sensorless control strategy	24
3.1	Field oriented control	26
3.1.1	Torque control of the PM-SyR machine	27
3.1.2	Speed control of the PM-SyR machine	29
3.2	Sensorless FOC	30
3.2.1	Hybrid flux observer	31
3.2.2	Flux cross-product position observer	34
3.2.3	PLL	35
3.3	I-f control	37
3.4	Transition strategies	40
3.4.1	Up transition	41

3.4.2	Down transition	42
4	Simulation results	44
4.1	Motor data	44
4.1.1	Flux maps	48
4.1.2	MTPA and Torque locus	50
4.1.3	Motor inductance	51
4.1.4	Current loop	52
4.1.5	Challenges motor	54
4.2	Simulink environment	54
4.2.1	Simulation parameters	56
4.3	Simulation results	57
4.3.1	Acceleration and deceleration tests at no load	58
4.3.2	Reference current vector along d-axis	61
4.3.3	Dead-time compensation OFF	63
4.3.4	Nominal load test	65
5	Experimental results	69
5.1	Test bench overview	69
5.2	Summary of the settings	73
5.3	Experimental results	74
5.3.1	Acceleration and deceleration test at no load	75
5.3.2	Acceleration and deceleration test under load	83
5.3.3	Nominal load test	87
5.3.4	Overload test	96
5.3.5	Harmonics Analysis	99
6	Conclusions	105
A	Implemented control code	108
B	Harmonics analysis	113
B.1	No load	114
B.2	12.5Nm torque load	116

List of Figures

1.1	Global electricity consumption from 1990 to 2019	1
1.2	Torque - speed characteristic of asynchronous and synchronous motors, when line supplied	3
1.3	Design of different type of Synchronous machines	4
1.4	PM-assisted SyR rotor design	6
1.5	Basic circuit diagram for most AC motor controllers	8
2.1	Active Flux block diagram	17
2.2	Extended electromotive force block diagram	18
2.3	Classification of Saliency based sensorless techniques	19
2.4	High-frequency signal injection partial scheme	20
2.5	Complete block diagram High-frequency signal injection with PLL	22
3.1	Block diagram for sensorless control with open loop starting	25
3.2	Complete sensorless control architecture	26
3.3	Torque control scheme	27
3.4	Positive and negative torque in dq current axes	28
3.5	Torque control scheme using MTPA LUT	29
3.6	Speed Field-Oriented Control architecture using encoder	29
3.7	Speed sensorless FOC architecture	31
3.8	Sensorless hybrid flux observer	31
3.9	Timing of voltage and current samples	33
3.10	Hybrid flux observer implemented with flux cross-product position observer	35
3.11	PLL block scheme	36
3.12	PLL block scheme with trigonometric coordinates	37
3.13	I-f control vector diagrams	38
3.14	Relationship among stationary, rotor and arbitrary reference frame	39
3.15	I-f control scheme	40

3.16	Transition diagram vector	41
4.1	ABB-Baldor motor	45
4.2	External mounted magnetic encoder	45
4.3	Motor nameplate	46
4.4	ABB stator and rotor design	47
4.5	ABB motor flux maps	48
4.6	Diagram vector of a PM-assisted SyR motor	49
4.7	Flux locus	50
4.8	MTPA trajectory and torque locus	50
4.9	ABB speed locus	52
4.10	Current loop block diagram in dq coordinates	53
4.11	Simulink model	55
4.12	Digital control subsystem	56
4.13	Acceleration and deceleration test at rated speed and no load, with 1.25 Hz speed bandwidth	59
4.14	Acceleration and deceleration test at rated speed and no load, with 2.5 Hz speed bandwidth	60
4.15	Acceleration and deceleration test at rated speed and no load, using a reference current vector along d -axis during I-f control	61
4.16	Acceleration and deceleration test with no dead-time compen- sation ($2\mu s$)	63
4.17	Acceleration and deceleration test with no dead-time compen- sation ($3\mu s$)	64
4.18	Imposing rated torque load with 1.25 Hz speed bandwidth	65
4.19	Removing rated torque load with 1.25 Hz speed bandwidth	66
4.20	Imposing rated torque load with 2.5 Hz speed bandwidth	67
4.21	Removing rated torque load with 2.5 Hz speed bandwidth	68
5.1	Test bench	69
5.2	Autotransformer and custom-made inverter	70
5.3	dSPACE Controller board and DSP	71
5.4	RTI-1005 simulink model	71
5.5	dSPACE controldesk	72
5.6	ABB Selivector: inverter and machine load	73
5.7	Acceleration and deceleration test at no load	78
5.8	Acceleration and deceleration test at no load, using a reference current vector located on d -axis during I-f control	79
5.9	Acceleration and deceleration test, using 1.25 Hz speed band- width	80

5.10	Acceleration and deceleration test at no load with 1.25 Hz speed bandwidth, using a reference current vector located on d-axis during I-f control	81
5.11	Focus on deceleration test at no load with 1.25 Hz speed bandwidth, using a 800 rpm/s deceleration slew-rate	82
5.12	Acceleration and deceleration test at 900 rpm with 15% of rated torque load	84
5.13	Acceleration and deceleration test at 900 rpm with 27.5% of rated torque load	85
5.14	Acceleration and deceleration test at 900 rpm with 40.2% of rated torque load	86
5.15	Rated torque load imposition at rated speed	88
5.16	Rated torque load removal at rated speed	89
5.17	Rated torque load imposition at rated speed, using 1.25 Hz speed bandwidth	90
5.18	Rated torque load removal at rated speed, using 1.25 Hz speed bandwidth	91
5.19	Rated torque load imposition at 80% rated speed	92
5.20	Rated torque load removal at 80% rated speed	93
5.21	Rated torque load imposition at 80% rated speed, using 1.25 Hz speed bandwidth	94
5.22	Rated torque load removal at 80% rated speed, using 1.25 Hz speed bandwidth	95
5.23	Torque characteristic	96
5.24	Imposition of 43 Nm torque load at half rated speed	97
5.25	Removal of 43 Nm torque load at half rated speed	98
5.26	4.5 Nm torque load sensorless (left) vs sensed (right) control, with 1.25 Hz speed bandwidth	100
5.27	4.5 Nm torque load sensorless (left) vs sensed (right) control, with 2.5 Hz speed bandwidth	101
5.28	Rated torque load sensorless (left) vs sensed (right) control, with 1.25 Hz speed bandwidth	102
5.29	Rated torque load sensorless (left) vs sensed (right) control with, 2.5 Hz speed bandwidth	103
A.1	Control code	108
A.2	Control code	109
A.3	Control code	110
A.4	Control code	111
A.5	Control code	112

B.1	No load sensorless (left) vs sensed (right) control, with 1.25 Hz speed bandwidth	114
B.2	No load sensorless (left) vs sensed (right) control, with 2.5 Hz speed bandwidth	115
B.3	12.5 Nm torque load sensorless (left) vs sensed (right) control, with 1.25 Hz speed bandwidth	116
B.4	12.5 Nm torque load sensorless (left) vs sensed (right) control, with 2.5 Hz speed bandwidth	117

List of Tables

1.1	PM-assisted SyR machine: advantages vs drawbacks	7
4.1	ABB motor parameters with low voltage configuration	46
5.1	Experimental platform	73
5.2	I-f control and Sensorless FOC	74
5.3	Flux observer and PLL	74

Chapter 1

Introduction

The purpose of this chapter is to give an overview about the electrical machine drives. First of all, the trend of the global electricity consumption will be analysed. After that, various typologies of electric machines will be showed, focusing on the ones most used in industrial environment in the last years. Moreover, the most famous control strategies for AC machine drive will be presented. At the end of the chapter, an overview of main topics covered in this thesis is provided.

1.1 Global electricity consumption

The *Global Energy Statistical Yearbook 2020* [1] analysed the trend of the global electricity consumption from 1990 to 2019 (Figure 1.1). As it can be seen, in the last three decades the global electricity consumption has considerably grown and the trend is expected to continue into future. Hence, the industries, government and researchers are working in order to find a sustainable solution for this challenge.

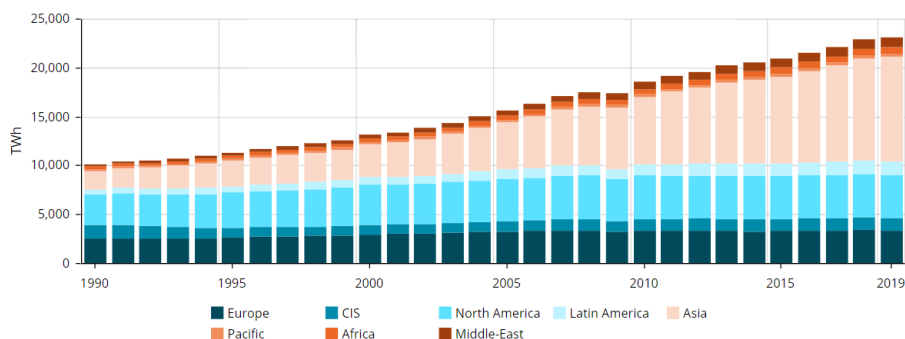


Figure 1.1: Global electricity consumption from 1990 to 2019 [1]

Electric motors are widely used all over the world, in particular in industries, where their size and also their losses cannot be trivial. For example, in [2], "Electric motors account for 42.9% (as of 2010) of electricity consumption in the Korean manufacturing sector, which represents 20.9% of total electric power demand in Korea". Therefore, increasing their efficiency can be a valid solution to reduce electricity consumption.

1.2 Classification of motor types

Electric motors are implemented in different fields of the industrial environment. In addition to the electric vehicles for traction, the electric motors find application in food processing machines, packing, pumps, spindle drives and so on. According to their final use, during the last 180 years different types of electric machines were developed. They can be grouped in two categories:

- **DC Motor:** these motors are supplied by a DC voltage and they can be divided in two big families:
 - Brushed DC motor: it uses the brushes to excite the rotor winding;
 - Brushless DC motor: the rotor is excited thanks to the permanent magnets allocated in its surface;
- **AC Motor:** these motors are supplied by an AC voltage and they can be divided in two big families:
 - Asynchronous motor: rotor rotates at a slower speed than the electromagnetic stator field under load;
 - Synchronous motor: the shaft's rotation is synchronized with the frequency of the supply electromagnetic field;

In the next section, the synchronous machines will be elaborated in detail.

1.3 Synchronous machines

Thanks to the advent of power electronics in the last years, the research and commercial interest in synchronous machines continue to increase. Unlike the asynchronous motor, these machines are not self-starting motors. In fact, in case of high rotor inertia, they cannot follow the magnetic field that rotates at higher speed than the starting one. A clear explanation can be provided taking into account *Torque curve* in the Figure 1.2.

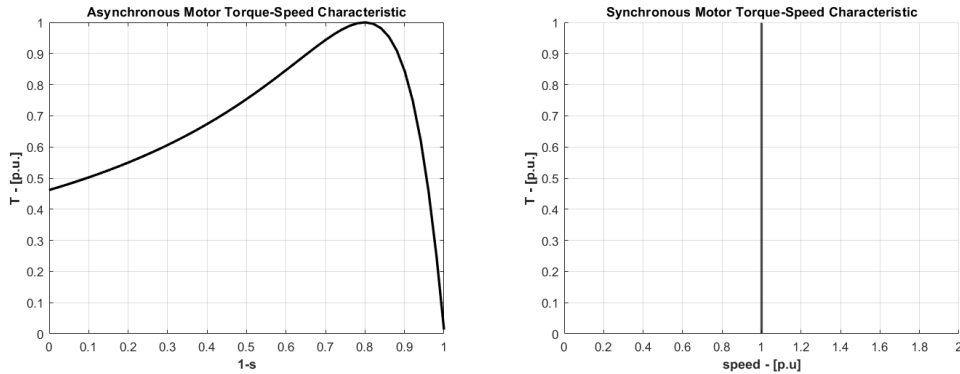


Figure 1.2: Torque - speed characteristic of asynchronous and synchronous motors, when line supplied

In the left figure, asynchronous motor presents a non zero torque at stand-still (slip $s = 1$): this permits to start the motor also without a converter used to control and regulate rotation magnetic field. In the right figure, synchronous motor can provide torque only at specific speed that depends on the frequency of the magnetic field: for this reason, a variable frequency drive (VFD) inverter capable of regulating magnetic field frequency from zero to the desired one is needed to correctly start the motor.

Synchronous motors are a broad category that includes permanent magnet motors with and without reluctance torque, and synchronous reluctance motors. They can be divided into five groups:

- **SPM**: surface permanent magnet. It is an isotropic sinusoidal brushless motor with no reluctance torque, where the PM are mounted on the surface of the rotor. The d -axis is aligned along the PM while the torque is controlled with current on q -axis and it is exactly proportional to the current.
- **IPM**: interior permanent magnet. It is a low anisotropic motor, where the PM are embedded inside the rotor, with reluctance and PM torque contribution: the first one is higher than the second one, due to the significant amount of PM located in the rotor. In order to minimize the amplitude of the current that provides a specific torque, d and q currents are usually located in maximum torque per ampere trajectory (MTPA).
- **PM-assisted SyR**: permanent magnet assisted synchronous reluctance. In this anisotropic motor, the permanent magnets are used

to improve the power factor (PF) and the speed range at constant power. The torque contribution of the permanent magnets is less than IPM. The torque is controlled with both d and q currents according to MTPA.

- **SyR**: synchronous reluctance. It is an high anisotropic motor with no PM, therefore only reluctance torque is provided.

Figure 1.3 shows stator and rotor design of the aforementioned machines. The grey areas represent steel, the white areas represent air or some non-magnetic material and black areas represent permanent magnets.

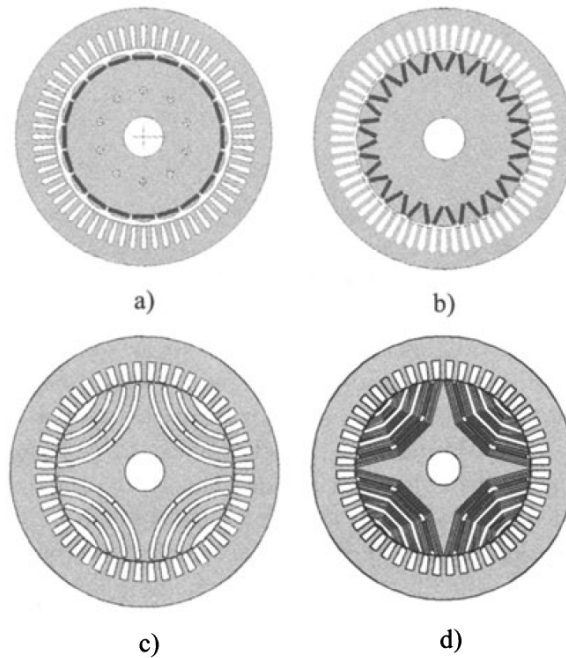


Figure 1.3: Design of: a) SPM, b) IPM, c) SyR d) PM-assisted SyR [3]

Moreover, synchronous motor, compared to DC and induction motor, presents the following advantages:

- Better efficiency: higher than 90%. In fact, lack of slip and rotor current are also a clear evidence of the less energy lost in converting between electrical energy and mechanical energy;
- Cold rotor: in case of permanent magnets synchronous machines (PMSM), no winding in the rotor permits to maintain its temperature very low. Indeed, no Joule losses are shown, while iron losses in the rotor are reduced;

- Wider air gaps: higher mechanical stability is reached;
- Constant speed irrespective of the loads: this feature is very useful in industrial drives where constant speed is independent required of the load it is driving.
- Better torque-to-inertia values;
- High power density and torque per unit volume;

The focus of the thesis is on PM-assisted SyR machine, therefore it will be analysed in depth in the following section.

1.4 PM-assisted synchronous reluctance motor

Applications of the synchronous motor are much broad. Indeed, changing quantity and position of the permanent magnets, the machine behaviour is modified.

In the last years, interest in using brushless synchronous AC machines, in particular in applications where previously asynchronous machines have been used, is increased a lot [4]. The PM-assisted synchronous reluctance motor, thanks to their synchronous rotation speed, possibility to use a sensorless control and other advantages that will be presented below, is a valid alternative among synchronous machines.

These drives present, as the most of AC machines, a quasi-sinusoidally distributed AC stator winding, controlled by a frequency converter (VFD) that provides a sinusoidal current to the driven machines.

PM-assisted SyR motor is the result of two motors mix: synchronous reluctance machine and internal permanent magnets machine. The same stator design as that of IPM and SyR is also compatible for PM-assisted SyR motors. What differs is the rotor. While SyR rotor is completely done with ferromagnetic material, the IPM one has an high quantity of permanent magnets. The PM-assisted synchronous reluctance motor has a discrete quantity of permanent magnets. In this way, cost of the motor is reduced. In addition, this motor has a good saliency and so a higher contribution of reluctance torque respect to magnets torque.

In this thesis, the reference frame used in PM-assisted SyR motor is not the same usually used in PM machines, where the d -axis is along the direction of PM flux. In fact, as it can be seen from Figure 1.4, the d -axis is defined along the low reluctance path and q -axis along the high reluctance path.

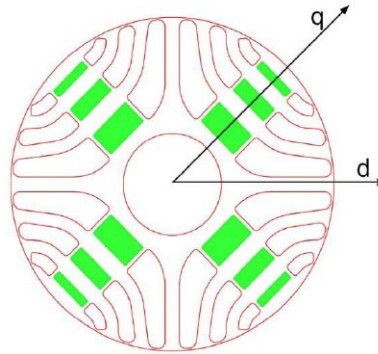


Figure 1.4: PM-assisted SyR rotor design with its reference frame [5]

The rotor presents air regions, called flux barriers, properly designed in order to increase machine's saliency. Permanent magnets are usually allocated in the central part of each flux barrier, aligned with q -axis.

The main advantages of this type of motor are:

- Respect to the synchronous reluctance motor, PM-assisted SyR machine presents an higher power factor (PF), inducing a reduction of stator ohmic losses [3], and so increasing also efficiency.
- Adding permanent magnets into barrier flux region leads also to a quite large constant power speed range. CPSR is the ratio between the maximum speed and the base speed for which the same power is obtained. This is a drawback of the SyR machines, where the power decrease quickly ($P \propto \frac{1}{\omega}$) if we are working on MTPV (maximum torque per volt) and the voltage limit is reached. Whereas, in PM-assisted SyR motor, adding the perfect amount of PM, we will never reach the MTPV. Thus, the power can be maintained constant until infinite speed. In the reality, magnetic characteristic depends on temperature and the PM is set for a specific load. Therefore, MTPV characteristic will be used at very limited high speed range.
- One of the main limitation of the IPM machine is the high voltage created at high speed with no load, in particular during fault converter condition [5]. In fact, high amount of PM create, under the conditions mentioned above, an high back-EMF at the terminals of the motor,

causing problems at converter and capacitors. In order to limit or eliminate this problem, machine must be suitably designed by reducing the quantity of PM and consequently increasing its anisotropy: PM-assisted SyR motor has these characteristics.

- Flux weakening capability: due to low PM quantity, it is easier to reduce flux at high speed because the permanent magnet flux is very poor. In this way, the demagnetizing current is also minimized [6]. Obviously, rotor design needs to be specific according to the application, but the main aspects are always the maximization of rotor anisotropy and reduction of PM amount.
- Suitability to sensorless control at standstill: injection of high-frequency signal is a valid low speed control strategies for this type of motor.

Magnetic behaviour of an electric motor is not linear but depends on the operating point. In addition, a common drawback that involves all the anisotropic motor is the cross-saturation effect: due to high saliency of the machine, d and q axes are not independent each other, but a condition in one axis influence the behaviour of the other one. To be clearer, with a fixed i_d , changing i_q , the flux along d -axis changes. For this reason, an accurate knowledge of flux maps is needed in order to obtain an efficient control [4].

Moreover, flux maps become fundamental in case of sensorless control. Elimination of speed/position sensor is a desirable feature in many applications for reducing costs and overall dimensions; machine with a good saliency are more suitable for sensorless control. In fact, at zero or low speed, an higher anisotropy allows to identify rotor position with a better precision [6].

In the following table 1.1 are resumed the main advantages and drawbacks of the PM-assisted SyR machine.

Table 1.1: PM-assisted SyR machine: advantages vs drawbacks

Advantages	Drawbacks
High efficiency and PF	-
High torque density and CPSR	-
Cold rotor	-
-	Higher cost
Minimization of demagnetizing current	-
-	Cross saturation effect
Simple flux weakening	-
Suitable to Sensorless control	-

1.5 Control of AC motor drives

AC motors convert the input electrical energy (alternating current) into output mechanical energy (torque and speed), available on the motor shaft. However, in order to obtain the desired output values, it is necessary to control it. AC motor controllers solve this problem by properly regulating the electrical input motor characteristics.

Every motor drives need a power supply that can be in DC or AC. Between the electrical supply and the motor there are different hardware components.

Figure 1.5 shows a generic block diagram for most motor drives.

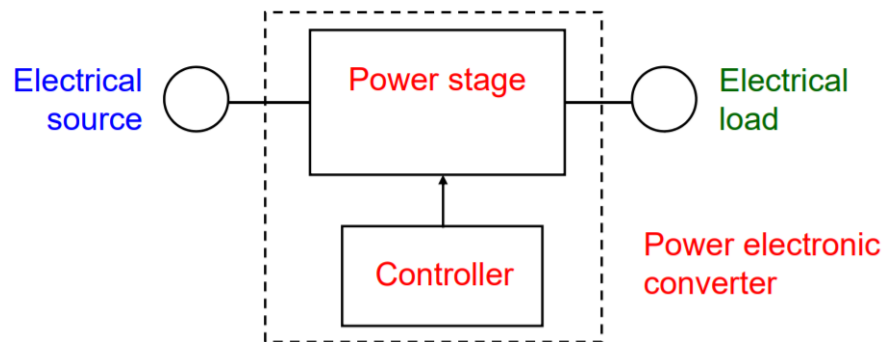


Figure 1.5: Basic circuit diagram for most AC motor controllers [7]

The power electronic converter is an interfacing element between an electrical energy source and an electrical load used to regular the input power according to the load characteristics [7].

As can be seen from Figure 1.5, the power electronic converter is made up of two elements: the power stage and the controller. In the first one flows the main power and there are usually one or more static converters, employing semiconductor power electronic devices. The second one is used to control the actions of the power stage.

In order to obtain a better regulation of electrical parameters, reduce complexity and costs, the power stage is made up of two devices: the AC/DC converter and the inverter. The first one transforms the AC supply to DC, and according to its circuit can also regulate its output voltage. The second one transforms the DC power into AC, setting the desired frequency.

The controller is usually composed by hardware devices that communicates with the power stage and the motor, in order to receive useful information (for example motor current and position angle) to properly control the

motor. The controller gives as output on/off signals to the semiconductor power electronic devices.

In addition, the controller includes a software interface used to manually set all the desired outputs (speed/torque) of the motor. Thanks to this software interface, it is possible to write the algorithm for the chosen control strategy.

During the last 40 years, thanks to the coming of digital control and increasing of computing power, a lot of control strategies were developed. Here there are the most commonly used control schemes:

- **FOC**: field oriented control. It is a technique used to control a broad AC motor drives. It consists of control the stator currents in the synchronous rotating $d - q$ reference frame: hence, FOC implementation requires transformation of stator currents from the stationary reference frame to the rotor flux reference frame (for IM) and electrical rotor position frame (for synchronous machine).
- **DTC**: direct torque control. It is a method used in variable-frequency drives to control the torque of AC motor drives. It is based on the direct regulation of the stator flux linkage vector amplitude and phase angle through the application of the instantaneous inverter states according to two bang-bang (hysteresis) regulators and one switching table [8].
- **DFVC**: direct flux vector control. It is a torque control strategy similar to DTC which adopts PI regulators and constant frequency PWM. DFVC is implemented on the stator flux coordinates. The flux amplitude and torque are closed loop controlled. Furthermore, the current vector amplitude is easily limited to avoid overcurrent [9].
- **MPC**: model-based predictive control. It is an advanced method to obtain the control actions of the motor by solving at each sampling time a control problem based on mathematical model and an estimation of current state, in order to know one step before what will be required. For instance, DeadBeat control is a predictive control scheme where, if model parameters are well-know, the transient response is faster than classical PI regulator based control and no steady state error. This is possible by compensating the execution delay of the digital control, thanks to the prediction of the current of the next PWM interrupt [10].

A more detailed description will be provided for the control strategies that will be used in this thesis.

1.6 Goal of master thesis

The purpose of this master thesis is to present a valid sensorless control strategy for a PM-assisted synchronous reluctance motor. The work is divided, including the introduction, in 6 chapters:

- **Chapter 1:** overview about the main motor typologies and control strategies, focusing on the synchronous machine;
- **Chapter 2:** overview of the different sensorless control strategies developed in the last 30 years;
- **Chapter 3:** exhaustive explanation of the sensorless control strategy adopted in this thesis, focusing also on the transition strategy;
- **Chapter 4:** after a brief description of the ABB-Baldor motor's characteristics, simulation results in *Simulink* environment are presented, using a simplified model system;
- **Chapter 5:** experimental results, obtained with the real setup and testing the motor in different conditions, are presented;
- **Chapter 6:** this chapter will present a conclusive review of the obtained results, showing benefits and drawbacks.

Chapter 2

Literature study

The purpose of this chapter is to give a clear overview of the most famous and useful sensorless techniques researched and developed in the last three decades, starting from the mathematical model of PM-assisted SyR machine in synchronous rotating $d - q$ reference frame.

The sensorless control is based on rotor position/speed detection methods, in order to be able to drive machines without a speed or position sensor device located in the shaft of the motor.

2.1 Why sensorless control?

Due to the interest of industries and universities, an intense research activity has been carried out to eliminate need of a position sensor in electrical drives. But what are the main drawbacks of position/speed sensor?

- Cost: in order to sell cheaper motor drives, reduce the number of components is the best way to achieve this target. Elimination of speed/position sensor implies also the cut out of cables connecting sensor and converter;
- Sensor location is not a trivial aspect: the given space is often tight or irregularly shaped, with cables and connections in competition for any available space;
- Losing accuracy at high speed: it strongly depends from the type of sensor used and from the number of division n_{div} (resolution);
- Position/speed sensor has to be supplied by a low voltage, different from the one used for the motor. Moreover, information signal has to be insulated from the main power;

- Unfriendly environment: this sensor is mounted in the shaft of the motor, thus vibrations and oscillations can modify the alignment between the two devices, causing a wrong position information. In addition, motors can reach high temperature: remembering that the most common and cheapest sensors are made of plastic materials, they can be damaged if the environment is not properly cooled;
- Mechanical connection: in some cases, sensor is not mounted inside the machine, hence an external fixing is needed. This requires extra costs and also the reliability of the system cannot be so high: external encoders which are connected by belts or couplings are not recommended because of elasticity and backlash of such elements;
- In case of sensor fault or cable disconnection, it is necessary that a suitable protection has to intervene in order to avoid mechanical or electrical problem to the motor.

Obviously, sensorless controls presents some drawbacks, depending by the method used. One of the most common and important disadvantage is the limitation of speed and position bandwidth. Therefore, sensorless controls present a lower speed control bandwidth than encoder one.

2.2 Mathematical model of a PM-assisted SyR machine

The analysis will be conducted considering a three phase PM-assisted SyR machine. In order to retrieve a simpler machine model, Eddy current and hysteresis losses are neglected.

Taking into account magnetic saturation phenomena, the dq rotor synchronous reference frame voltage equations of the PM-assisted SyR can be expressed as:

$$\begin{cases} v_d = R_s i_d + \frac{d\lambda_d}{dt} - \omega \lambda_q \\ v_q = R_s i_q + \frac{d\lambda_q}{dt} + \omega \lambda_d \end{cases} \quad (2.1)$$

where:

- v_d, v_q are the stator voltages [V] in dq frame;
- i_d, i_q are the stator currents [A] in dq frame;
- R_s is the stator resistance [Ω];

- λ_d, λ_q are the flux linkage [Vs] in dq frame;
- ω is the electrical rotor pulsation [rad/s];

Considering the self-axis magnetic saturation, motor's magnetic model is non-linear. In addition, cross-coupling between d and q axes is taken into account. Therefore, the relation between machine current and flux can be synthesized as:

$$\begin{cases} \lambda_d = \lambda_d(i_d, i_q) \\ \lambda_q = \lambda_q(i_d, i_q) \end{cases} \quad (2.2)$$

In this thesis the convention used for the dq rotor reference frame is the one exploited for synchronous reluctance machines. These axes rotate with the rotor, in particular the negative q direction follows the permanent magnets flux while the d axis point to the direction of maximum inductance, as it can be seen from Figure 1.4. Therefore, contribution of the PM flux (λ_m) is hidden into q axis flux:

$$\lambda_q(i_d, i_q) = \lambda_{q0}(i_d, i_q) - \lambda_m \quad (2.3)$$

where $\lambda_{q0}(i_d, i_q)$ is the q axis flux linkage related to machine current. The motor torque can be written as:

$$T = \frac{3}{2}p(\lambda_d i_q - \lambda_q i_d) \quad (2.4)$$

where T [Nm] is the produced torque by the machine and p is its pole-pairs. The mechanical equation of the motor can be expressed by:

$$T - T_l - B\omega_r = J \frac{d\omega_r}{dt} \quad (2.5)$$

where T_l is the load torque, J is the moment of inertia [$kg \cdot m^2$], ω_r [rad/s] is the mechanical rotor speed and B [$Nm \cdot s$] the friction coefficient.

Moreover, relation between mechanical rotor position (θ_r) and speed (ω_r) can be expressed as:

$$\omega_r = \frac{d\theta_r}{dt} \quad (2.6)$$

The same equation is valid also considering the electrical rotor position (θ) and electrical speed (ω). Mechanical position and electrical position are obviously related by machine pole-pairs:

$$\theta = p\theta_r \quad (2.7)$$

2.3 Classification of sensorless control

In this chapter, different existing sensorless control methods for synchronous motor drives will be analysed and discussed. Position/speed estimation methods can be divided into three approaches [11]:

- **Fundamental model sensorless techniques:** this category works properly only at medium-high speed because it is based on back-EMF. In fact, at low speed, back electromotive force is very low, thus voltage SNR (signal to noise ratio) cannot be sufficiently high for a correct detection of position angle. However, this approach is widely diffused for its simplicity and reliability at medium-high speed. In particular, the most popular fundamental model sensorless techniques are:
 - Flux cross-product position observer;
 - Extended EMF;
 - Active flux.
- **Saliency based sensorless technique:** this category overcomes the limitation of fundamental model sensorless technique, obtaining very good results at low speed and standstill. These techniques are based on tracking the saliency position in electric motor thanks to the high frequency signal injection. This approach includes different methods and according to the type of high-frequency excitation, they can be divided in:
 - Rotating voltage or current injection;
 - Pulsating voltage or current injection.
- **Open loop start sensorless control:** it is a very simple method, with a modest dynamics due to absence of speed loop. However, the purpose of this technique is to start the motor and reaches a threshold speed after which the fundamental model sensorless technique can work. The most popular open loop control strategy are:
 - **V/Hz control:** it is a very simple control used for induction machines (IM) where imposed voltage and frequency are strictly correlated;
 - **I-f control:** it essentially uses FOC for current control, where a constant reference current vector at a given reference frequency is imposed. It can be used for a broad types of motors where there is the need to make a parking or alignment. Moreover, it can be used as a starting method for sensorless control.

2.4 Fundamental model sensorless techniques

The idea of fundamental model sensorless technique is to use electrical model equations of the machine to estimate the induced back-EMF and thus the rotor speed and position [12]. Techniques based on this method are the most adopted in sensorless control strategies thanks to their simplicity and reliable performance. However, these sensorless techniques give good results only above a minimum speed, that is necessary to have sufficient back-EMF in the motor: low speed estimation is not so accurate. Therefore, other types of sensorless methods have to be used. Another disadvantage of these methods, in particular at low speed, are: sensitivity against parameter uncertainties (for example the stator resistance and deadtime) and measurement noise (for example stator currents) [13].

This approach involves the voltage model (stator equation) and the current model. In particular, many fundamental model sensorless techniques are based on estimation or observation of the stator flux linkage in $\alpha\beta$ frame, using machine model equations: it is the case of a sensorless version of Hybrid Flux Observer (HFO) [11]. For a clearer explanation see section 3.2.1.

In the following three subsections, flux cross product position observer, active flux and extended EMF model sensorless techniques will be briefly described.

2.4.1 Flux cross product method

One of easiest method used to estimate the electrical rotor position is the flux cross product position observer: in fact, it can be immediately implemented with only two lines of C-code. As other sensorless techniques, this method is also based on the knowledge of the motor flux linkage. Therefore a flux observer has to be coupled with this sensorless technique. The relation which permits to retrieve the sine and cosine of the rotor position estimation ($\hat{\theta}_{cr}$) can be expressed as:

$$\begin{cases} \sin(\hat{\theta}_{cr}) = \frac{\hat{\lambda}_d^i \hat{\lambda}_\beta^i - \hat{\lambda}_\alpha^i \hat{\lambda}_q^i}{\lambda^2} \\ \cos(\hat{\theta}_{cr}) = \frac{\hat{\lambda}_d^i \hat{\lambda}_\alpha^i + \hat{\lambda}_\beta^i \hat{\lambda}_q^i}{\lambda^2} \end{cases} \quad (2.8)$$

As it can be seen, it is needed the knowledge of the flux linkage both in dq and $\alpha\beta$ frames. In addition, this method could provide a wrong position estimation if the motor flux is zero. Therefore, simple precautions will be adopted.

A detailed analysis of flux cross-product position observer is shown in section 3.2.2.

2.4.2 Active Flux

The active flux concept is to turn a salient-pole machine into an equivalent nonsalient-pole one [13]. The method that will be here described is valid only if PM is in d -axis: therefore it cannot be applied to PM-assisted SyR motors. The active flux λ_d^a can be defined as the flux that is multiplied by q -current to calculate the torque of AC machines in rotor reference frame [14]:

$$T = 1.5p\lambda_d^a i_q \quad (2.9)$$

where T is the electromagnetic torque and λ_d^a is the active flux along d -axis.

One of the main advantage of this method is the active flux vector is independent of the reference frame (dq axes, $\alpha\beta$ axes, etc):

$$\boldsymbol{\lambda}^a = \boldsymbol{\lambda} - L_q \cdot \mathbf{i} \quad (2.10)$$

The active flux falls along d -axis [15]. Therefore, active flux vector rotates with the rotor, providing information on rotor electrical position. Now, taking into account the PM-Style convention, where PMs are along d -axis, it can be written [11]:

$$\boldsymbol{\lambda}_{dq}^a = \boldsymbol{\lambda}_{dq} - L_q \mathbf{i}_{dq} \quad (2.11)$$

$$\begin{cases} \lambda_d^a = (L_d - L_q)i_d + \lambda_m \\ \lambda_q^a = 0 \end{cases} \quad (2.12)$$

where L_d and L_q are the apparent inductances in d and q axes; Otherwise, considering $\alpha\beta$ frame:

$$\boldsymbol{\lambda}_{\alpha\beta}^a = \boldsymbol{\lambda}_{\alpha\beta} - L_q \mathbf{i}_{\alpha\beta} \quad (2.13)$$

$$\begin{bmatrix} \lambda_\alpha^a \\ \lambda_\beta^a \end{bmatrix} = [(L_d - L_q)i_d + \lambda_m] \begin{bmatrix} \cos \hat{\theta} \\ \sin \hat{\theta} \end{bmatrix} = \lambda^a \begin{bmatrix} \cos \hat{\theta} \\ \sin \hat{\theta} \end{bmatrix} \quad (2.14)$$

where $\hat{\theta}$ is the estimated d -axis electrical rotor angle. Therefore it is easy to retrieve sine and cosine of the angle:

$$\begin{cases} \cos \hat{\theta} = \frac{\lambda_\alpha^a}{\lambda^a} \\ \sin \hat{\theta} = \frac{\lambda_\beta^a}{\lambda^a} \end{cases} \quad (2.15)$$

Figure 2.1 shows the block diagram of the active flux method, providing as output the sine and cosine of the estimated electrical rotor angle.

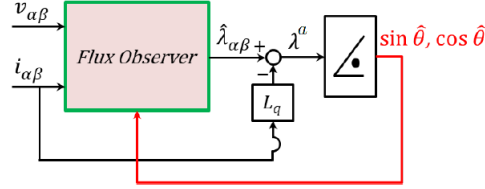


Figure 2.1: Active Flux block diagram [11]

Obviously, an accurate hybrid flux observer (HFO) is necessary to know the observed flux $\hat{\lambda}_{\alpha\beta}$, current measurement $i_{\alpha\beta}$ and inductance along q axis.

2.4.3 Extended EMF

A very common fundamental model sensorless technique used in the last decades is the Extended Electromotive Force (EEMF). This method can be applied to all PMSM, but with a difference: whereas for SMPM machines position information is contained in the flux or EMF term, in IPM machines it is contained also in inductance, due to their saliency [16].

For simplicity, linear magnetic model will be used, ignoring saturation. Therefore, considering the dq rotating frame of IPM machine, the state equation is:

$$\begin{bmatrix} v_d \\ v_q \end{bmatrix} = \begin{bmatrix} R_s + sL_d & -\omega L_q \\ \omega L_d & R_s + sL_q \end{bmatrix} \begin{bmatrix} i_d \\ i_q \end{bmatrix} + \begin{bmatrix} 0 \\ \omega \lambda_m \end{bmatrix} \quad (2.16)$$

where:

- $[v_d \ v_q]^T$ is voltage on rotating frame;
- $[i_d \ i_q]^T$ is current on rotating frame;
- s is the differential operator.

Moving in stator coordinates, tracking EMF signal is not very easy:

$$\begin{bmatrix} v_\alpha \\ v_\beta \end{bmatrix} = \begin{bmatrix} R_s + sL_0 & 0 \\ 0 & R_s + sL_0 \end{bmatrix} \begin{bmatrix} i_\alpha \\ i_\beta \end{bmatrix} + \omega \lambda_m \begin{bmatrix} -\sin(\theta) \\ \cos(\theta) \end{bmatrix} + sL_1 \begin{bmatrix} \cos(2\theta) & \sin(2\theta) \\ \sin(2\theta) & -\cos(2\theta) \end{bmatrix} \begin{bmatrix} i_\alpha \\ i_\beta \end{bmatrix} \quad (2.17)$$

where:

- $L_0 = \frac{L_d + L_q}{2}$ is the common mode inductance, representing the non-saliency of the machine;
- $L_1 = \frac{L_d - L_q}{2}$ is the differential mode inductance, representing the saliency of the machine;

As it can be seen in above equation 2.17, the last part (proportional to L_1) prevents the tracking of EMF. However, it can be manipulated by mathematical operation in dq reference frame, shifting the content of impedance matrix in EMF matrix, obtaining:

$$\begin{bmatrix} v_d \\ v_q \end{bmatrix} = \begin{bmatrix} R_s + sL_d & -\omega L_q \\ \omega L_d & R_s + sL_q \end{bmatrix} \begin{bmatrix} i_d \\ i_q \end{bmatrix} + \begin{bmatrix} 0 \\ \omega \lambda_m + (L_d - L_q) \cdot (\omega i_d - s i_q) \end{bmatrix} \quad (2.18)$$

Returning to $\alpha\beta$ stator coordinates:

$$\begin{bmatrix} v_\alpha \\ v_\beta \end{bmatrix} \begin{bmatrix} R_s + sL_d & \omega(L_d - L_q) \\ -\omega(L_d - L_q) & R_s + sL_d \end{bmatrix} \begin{bmatrix} i_\alpha \\ i_\beta \end{bmatrix} + [\omega \lambda_m + (L_d - L_q) \cdot (\omega i_d - s i_q)] \begin{bmatrix} -\sin(\theta) \\ \cos(\theta) \end{bmatrix} \quad (2.19)$$

The last term, aligned to q axis, represents the estimated back electromagnetic force in $\alpha\beta$ coordinates ($\hat{e}_{\alpha\beta}$). Therefore, implementation of extended electromotive force is straightforward: starting from the measured current and knowledge of voltage, frequency and other parameters (R_s, l_d, l_q), the EMF can be retrieved as:

$$\hat{e}_{\alpha\beta} = \begin{bmatrix} v_\alpha \\ v_\beta \end{bmatrix} - \begin{bmatrix} R_s + sL_d & \omega(L_d - L_q) \\ -\omega(L_d - L_q) & R_s + sL_d \end{bmatrix} \begin{bmatrix} i_\alpha \\ i_\beta \end{bmatrix} \quad (2.20)$$

Figure 2.2 shows the block diagram of the EEMF method, giving as output the estimated electrical rotor angle.

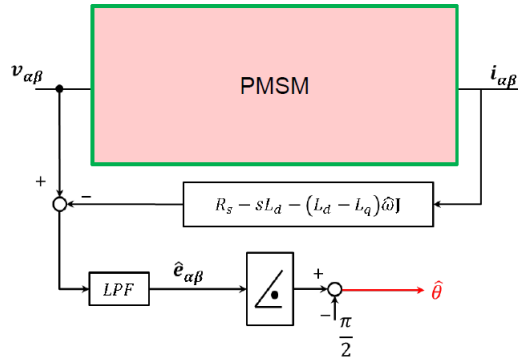


Figure 2.2: Extended electromotive force block diagram [11]

As said before, $\hat{e}_{\alpha\beta}$ contains itself electrical rotor position information, therefore once it is filtered and extrapolated, it is sufficient to subtract $\frac{\pi}{2}$ to obtain the estimated direction of rotor d-axis.

2.5 Saliency based sensorless techniques

As said before, the fundamental model sensorless methods fail at standstill and low speed due to the poor amount of back-EMF produced. Therefore, in the last years, a lot of researches were conducted in order to find a new useful technique running at low speed: saliency based sensorless techniques overcome low speed limitation, tracking the position of saliencies (asymmetries) in electric machines and so finding the direction of maximum or minimum incremental inductance [17].

But how do they work? These methods are based on the same physical principles: an high frequency signal, different from the fundamental one used to torque production, excites the machine via inverter and a HF response is demodulated to obtain the rotor position estimation. Many methods are developed and the main differences among them are[18]:

- Type of HF signals injection;
- Type of signals measured;
- Signal demodulation and manipulation to estimate rotor position.

Figure 2.3 illustrates a clear classification of the main methods belonging to saliency based sensorless techniques.

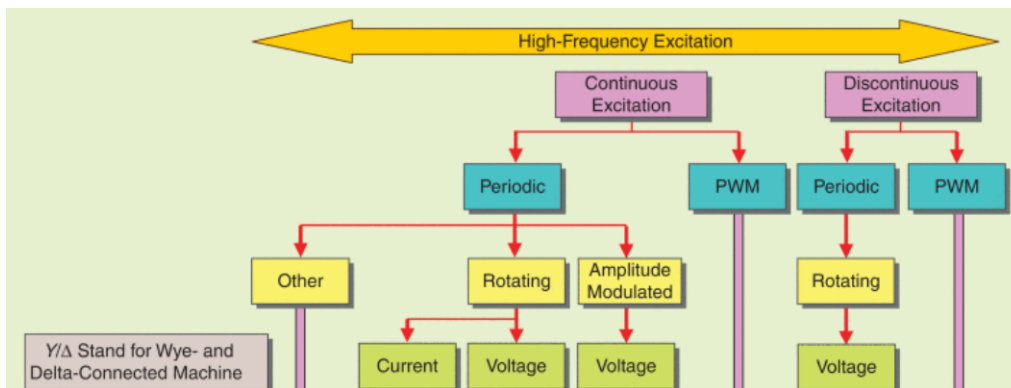


Figure 2.3: Classification of Saliency based sensorless techniques [18]

Different method could provide different results in the same machine drive due to parasitic effect on the cables, non-sinusoidal distributed winding and non-ideal environment of the inverter.

As the name of technique suggests, these methods work well in all motors presenting a relevant incremental anisotropy ($l_d \neq l_q$): IPM, PM-assisted synchronous machines and synchronous reluctance motors are adequate for this application. However, saliency based sensorless techniques are unreliable for SPM machine and IM.

2.5.1 Pulsating HF voltage injection

One of the most common saliency based sensorless techniques is based on the injection of pulsating HF voltage. Remember: this voltage injection is local, that is around the working point.

The author of the the paper [19] shows a partial scheme (Figure 2.4) of a high-frequency signal injection method, where inverter provides both fundamental and HF components.

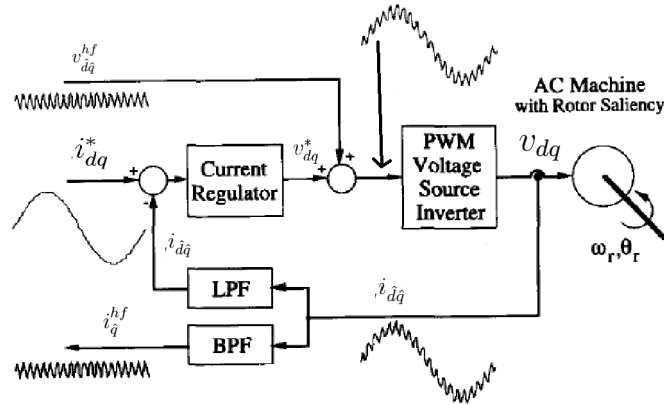


Figure 2.4: High-frequency signal injection partial scheme utilizing a PWM voltage source inverter [19]

A sinusoidal HF voltage is injected into the estimated \hat{d} axis [11]:

$$\begin{cases} v_{\hat{d}}^{hf} = u_c \cos(\omega_c t) \\ v_{\hat{q}}^{hf} = 0 \end{cases} \quad (2.21)$$

where:

- $v_{\hat{d}}^{hf}$ and $v_{\hat{q}}^{hf}$ are the injected voltages;

- u_c is the peak of injected voltage;
- ω_c is the pulsation of injected voltage.

It can be retrieved that high frequency current component in estimated rotating frame is equal to [20]:

$$i_{\hat{d}\hat{q}}^{hf} = e^{\mathbf{J}\tilde{\theta}} L_{\delta}^{-1} e^{-\mathbf{J}\tilde{\theta}} \boldsymbol{\lambda}_{\hat{d}\hat{q}}^{hf} \quad (2.22)$$

where:

- The orthogonal rotational matrix is $\mathbf{J} = \begin{bmatrix} 0 & -1 \\ 1 & 0 \end{bmatrix}$
- $\tilde{\theta}$ is the position error;
- $L_{\delta} = \begin{bmatrix} l_d & l_{dq} \\ l_{dq} & l_q \end{bmatrix}$ is the incremental inductance matrix, including cross-saturation term (l_{dq});
- $\boldsymbol{\lambda}_{\hat{d}\hat{q}}^{hf}$ is the HF flux component in estimated rotating axis;

In particular:

$$i_{\hat{q}}^{hf} = \frac{-l_{\Delta} \sin(2\tilde{\theta}) - l_{dq} \cos(2\tilde{\theta})}{l_d l_q - l_{dq}^2} \frac{u_c \sin(\omega_c t)}{\omega_c} \quad (2.23)$$

where $l_{\Delta} = \frac{l_d - l_q}{2}$.

Remembering the injected voltage in estimated q axis was equal to zero ($v_{\hat{q}}^{hf} = 0$), $i_{\hat{q}}^{hf} = 0$ is expected. However, as it can be seen from equation 2.23, $i_{\hat{q}}^{hf}$ is null, only in the absence of cross-saturation, at $\tilde{\theta} = 0$. If $\tilde{\theta} \neq 0$, it means estimated dq axes are different from the real one.

Now, considering absent the cross-saturation ($l_{dq} = 0$), $i_{\hat{q}}^{hf}$ contains itself information about position error. Therefore, in order to obtain $\hat{\theta} = \theta$, minimization of $i_{\hat{q}}^{hf}$ is desired. It can be possible using a PLL (Phased-Locked Loop) with $i_{\hat{q}}^{hf}$ as input. In fact, PLL's aim is to force the position error signal to zero, obtaining a converge between θ and $\hat{\theta}$. Figure 2.5 shows a complete block diagram of the above mentioned method.

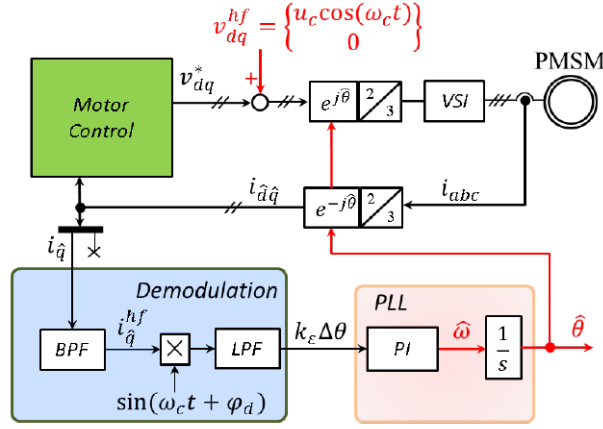


Figure 2.5: Complete block diagram High-frequency signal injection with PLL [11]

In conclusion, HF response method are used only at low speed because, comparing to fundamental model sensorless techniques, they presents the following drawbacks:

- Due to the amplitude of HF signal voltage injection, the one used for the main power is abruptly reduced;
- Cross-saturation effect ($I_{dq} \neq 0$) could induce a steady state position error (see equation 2.23) and possible instability;
- HF injection increase losses;
- HF current and flux produced by HF voltage create torque ripple.

2.6 Summary

To conclude, fundamental model sensorless techniques are always preferable thanks to their simplicity and reliability at high speed. Saliency based sensorless techniques are a valid solution in application where motor will work at low speed or standstill.

However, in order to achieve high speed, machine drives need always to go across low speed region. Therefore, the methods that can be used, as long as sufficient speed is reached, are:

- Saliency based sensorless techniques;
- Open loop start sensorless control.

In case that the low speed is not a working point in the considered drive application, an open loop control strategy can be used in low speed region, until enough motor velocity is reached. After that, the control system strategy will move to the fundamental model sensorless techniques. Particular attention is needed in the jump from open-loop control to closed-loop control and viceversa. A clear explanation will be provided in the next chapter.

Chapter 3

Proposed sensorless control strategy

The aim of this chapter is to present a useful sensorless control strategy for PM-assisted SyR motors. First of all, in-depth analysis about the proposed sensorless control strategy will be conducted, showing the main aspects that characterize the control. After that, an exhaustive description about transition strategy will be provided.

The method proposed to control a PM-assisted SyR motor, without any position/speed sensor, is based on I-f starting method and a fast jump from open-loop speed control to close-loop sensorless field oriented control (FOC). Therefore, there are only two stages:

- I-f control;
- Sensorless FOC.

One of the easiest way used to assist the motor start is the I-f control: it is a open-loop speed control, while current is closed loop regulated with FOC. Once a sufficient reference speed (ω_{up}) is reached, the system automatically switch to closed loop sensorless FOC. During deceleration to stop the motor or speed reversal, another jump from sensorless FOC to I-f control will happen at a specific estimated speed (ω_{down}). Figure 3.1 illustrates philosophy of the proposed sensorless control method.

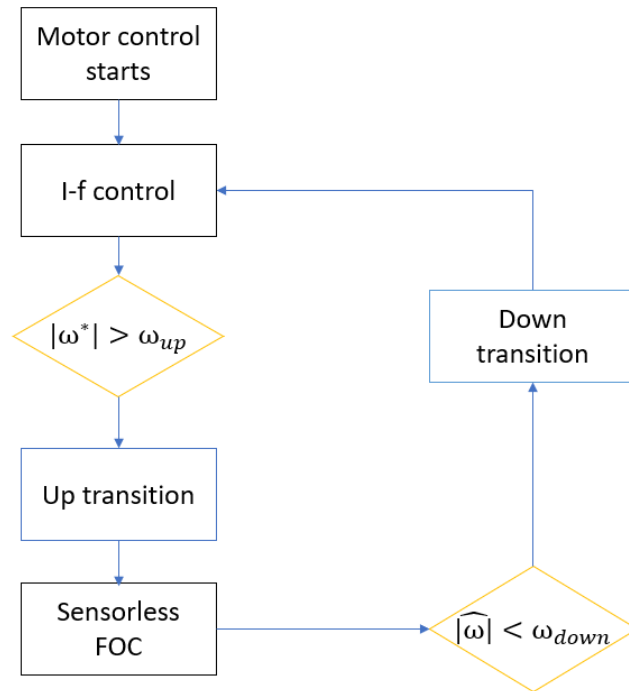


Figure 3.1: Block diagram for sensorless control with open loop starting

A particular attention is needed during the transition between the two controls: it must be as smooth as possible, avoiding discontinuities in the control. Moreover, transition strategy can include [11]:

- Hysteresis control: threshold speed for transition from I-f control to sensorless FOC is set higher than the transition from FOC to I-f control;
- Auxiliary compensation angle: a compensation angle is progressively driven to zero during transition, in order to avoid abrupt discontinuities;
- Fusion strategy: the two control methods are fused in a unique control where, according to speed, prevails one or the other.

In the proposed sensorless control, hysteresis technique will be adopted for the up and down transition. To avoid chattering between the two models around the threshold speed, a hysteresis speed window is adopted such that the two transitions occur at different speeds.

In order to clarify how the proposed strategy works, the complete block diagram is presented in Figure 3.2.

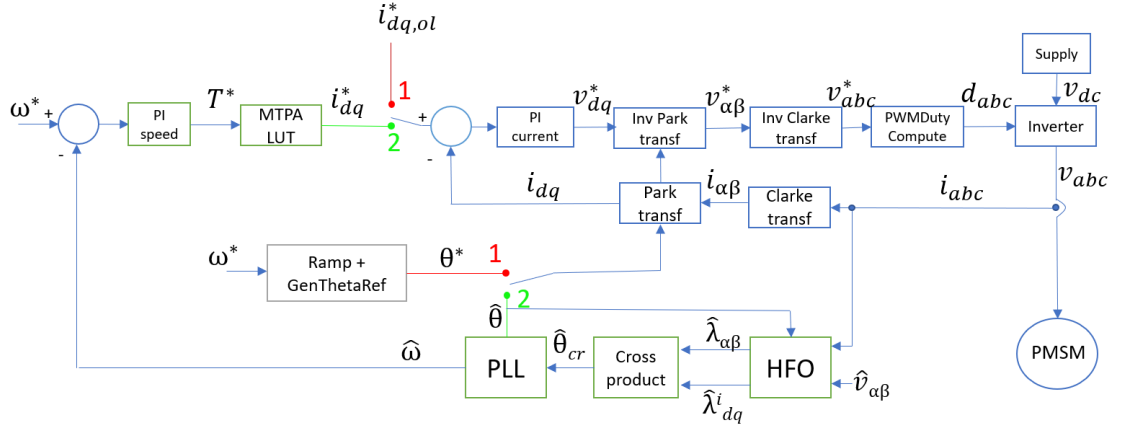


Figure 3.2: Complete sensorless control architecture

Switching to position 1, the I-f control is active, whereas switching to position 2, the sensorless FOC is active. Moving from one position to another depends from the reference or estimated speed: it will be explained in section 3.4.

3.1 Field oriented control

Thanks to its higher degrees of freedom for each desired torque and speed value, field oriented control has better stability and higher efficiency due to MTPA operation with respect to I-f control. The first FOC control was proposed by F. Blascke for controlling an induction motor in 1971 [21].

The aim of this section is to provide an overview of the field oriented control, using position encoder. While in induction machines the reference d -axis is aligned along the rotor flux, in synchronous machines it is aligned either along PMs, in the case of SPM and IPM machines, or along the maximum inductance path, in the case of synchronous reluctance and PM-assisted synchronous reluctance motors.

Due to progress in power electronics, this type of control became very popular for AC machines in industries. Thanks to Park and Clarke transformation, induction motor drives behaves as DC motor: it is realizable due to the improved performance of the microprocessors developed since 1970. In particular, comparing induction machines to the DC ones, the rotor winding is the field winding whereas the stator winding is the armature winding [22].

The principle behind this control for a induction machine is a separate excitation DC motor: the armature current control the torque, while the excitation current regulates magnetizing flux generation [23]. The equivalent

of FOC in PM-assisted SyR machines is achieved by aligning along the d -axis (maximum inductance path).

AC control strategy can be made up of three cascaded control loops in different layers:

- Current or flux loop: inner layer;
- Speed loop: middle layer;
- Position loop: outer layer.

Obviously, each internal loop influences the others: for example, the current loop response affects the dynamics of the outer speed loop and so on. Therefore, a high-bandwidth current tuning is required in order to achieve a better dynamic of the machine drive.

The aim of this thesis is to control motor speed, thus position loop is not requested. The analysis starts with the internal torque control scheme, illustrated in Figure 3.3, giving as output the duty cycle (d_{abc} or d_{uvw}).

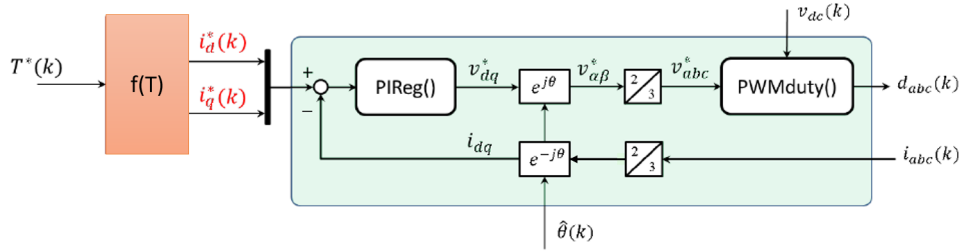


Figure 3.3: Torque control scheme [22]

3.1.1 Torque control of the PM-SyR machine

Substituting the magnetic model of the machine (equation 3.1) into λ_d and λ_q of equation 2.4, it is possible to retrieve a new torque equation in a SyR convention:

$$\begin{cases} \lambda_d = L_d i_d \\ \lambda_q = L_q i_q - \lambda_m \end{cases} \quad (3.1)$$

$$T = \frac{3}{2} p \left(\lambda_m i_d + (L_d - L_q) i_d i_q \right) = T_{PM} + T_{rel} \quad (3.2)$$

The PM torque (T_{PM}) is proportional to i_d while reluctance torque (T_{rel}) is proportional to $i_d i_q$, therefore relation between current and torque is not linear in dq -plane.

As it can be seen from above equation, if a positive torque is required, i_d and i_q must be positive, while if a negative torque is required, i_d must be negative and i_q positive. Therefore, a PM-assisted SyR machine, using the SyR convention, works in the first and second quadrants (Figure 3.4).

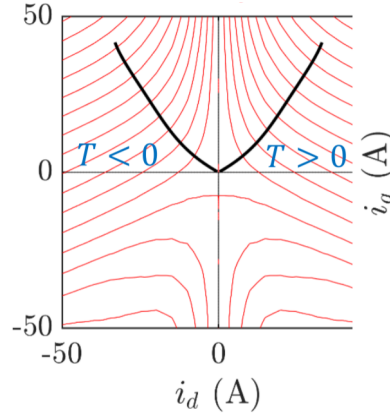


Figure 3.4: Positive and negative torque in dq current axes [24]

Controlling i_d and i_q current components, it is possible to obtain the desired torque. But there are different current combinations that provide the requested torque. In order to minimize the current needed for a specific torque and thus minimizing the copper losses, the main methods to retrieve the best current components are:

- Approximated MTPA;
- Correct MTPA.

In the first method, amplitude of the reference current vector is calculated knowing the constant torque factor (\hat{k}_t) and desired torque T^* :

$$|\mathbf{i}_{dq}^*| = \frac{T^*}{\hat{k}_t} \quad (3.3)$$

Once the amplitude is calculated, it is necessary to impose a constant current phase angle γ respect to the d -axis, in order to calculate the reference dq current components:

$$\begin{cases} i_d^* = |\mathbf{i}_{dq}^*| \cos(\gamma) \\ i_q^* = |\mathbf{i}_{dq}^*| \sin(\gamma) \end{cases} \quad (3.4)$$

Finding the best approximation of the two parameters (\hat{k}_t and γ) is not easy: the constant torque factor is sometimes retrieved from the datasheet,

The control procedure of this control system can be described as: firstly, preset the reference value of input speed (ω^*). This speed is compared with measured one, retrieved thanks to the block *speed compute* which has as input the position signal that comes from position sensor mounted in the shaft of the motor. Difference between the two speeds goes to a PI controller that, according to the tuning, gives as output the reference torque. This signal, as mentioned above, is processed with a linear interpolation of MTPA LUT, retrieving the appropriate *dq* reference currents (i_d^*, i_q^*). Then, by properly scaling the measured current i_a, i_b, i_c , the Clarke and Park transformation are carried out, obtaining values of currents in *dq* rotor frame. These currents are compared with the reference ones and the resulting error is supplied to the two PI current regulators that determine new reference voltage values (v_d^*, v_q^*). These voltages are subjected to inverse Park and Clarke transformation in order to become the input for *PWMDuty compute* block, which computes the 3-phase duty cycles according to the reference voltage signals (v_a^*, v_b^*, v_c^*) and the dc-link voltage. Moreover, duty cycles are distorted by the common mode voltage in order to exploit the entire dc voltage supply: this technique is called *balancing of envelopes (BEM)*. After that, these signals are provided to the inverter and appropriately converted in order to control power modules: they produce three-phase voltages with desired amplitudes and phase shift to properly control the motor.

3.2 Sensorless FOC

As it can be seen from the last section, the speed/position information to properly control the motor is provided by a sensor. However, the aim of this thesis is to control the drive machine without any position or speed transducer. Therefore, the control scheme will be modified.

The proposed sensorless control technique is based on flux cross-product position observer: starting from a sensorless version of hybrid flux observer (HFO), flux in $\alpha\beta$ and $\hat{d}\hat{q}$ axes are retrieved and then the estimated electrical rotor angle is calculated with cross-product method. At the end, this information is supplied to PLL in order to filter it and also retrieve electrical rotor speed estimation. Summarizing, the elements that need attention are:

- Hybrid flux observer;
- Flux cross-product based position error signal;
- PLL;

The Sensorless FOC speed control scheme is shown in Figure 3.7.

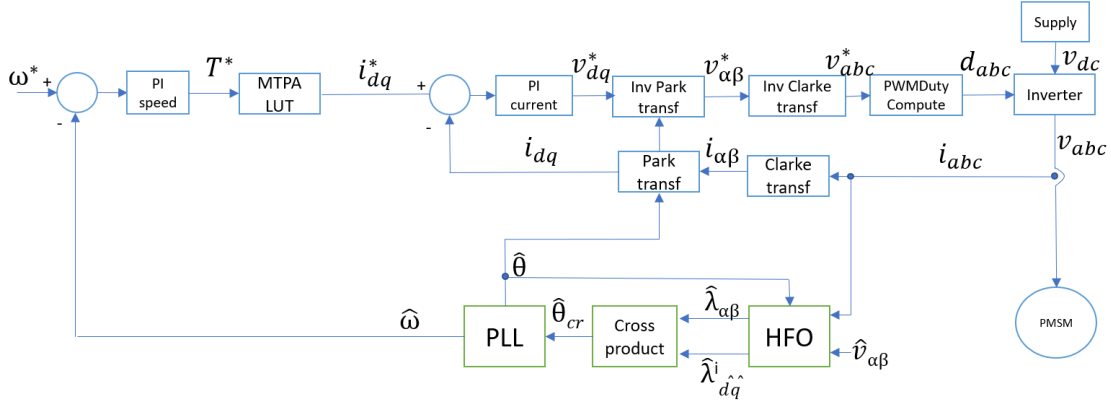


Figure 3.7: sensorless FOC architecture

Next subsections will provide a carefully description of the above listed elements.

3.2.1 Hybrid flux observer

As said before, the proposed sensorless control is based on the knowledge of the machine flux linkage. There are different methods that can be applied: the one used in this thesis is a sensorless version of a hybrid flux observer for synchronous machines, showed in Figure 3.8.

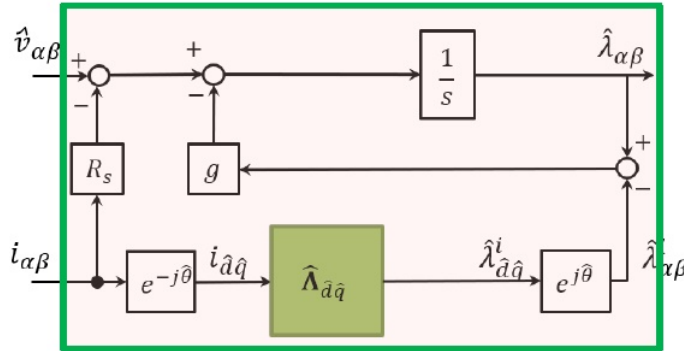


Figure 3.8: Sensorless hybrid flux observer [11]

This method is a linear combination of two models estimates:

- **Voltage model estimate:** flux linkage in stationary $\alpha\beta$ frame is retrieved integrating the back-EMF:

$$\hat{\lambda}_{\alpha\beta} = \frac{\hat{v}_{\alpha\beta} - R_s i_{\alpha\beta}}{s} \quad (3.5)$$

where $\hat{v}_{\alpha\beta}$ is the estimated voltage starting from dc-link voltage, current measurements, inverter states (d_{abc}), voltage drop in the diode (ΔV_d) and dead-time compensation (ΔV_{d-t}). This voltage ($\hat{v}_{\alpha\beta}$) is retrieved from Clarke transformation of the estimated voltage in three-phase system:

$$\hat{v}_{abc} = v_{dc} \cdot \left(d_{abc} - ((1 - d_{abc})\Delta V_{d-t} + d_{abc}\Delta V_d) \right) \quad (3.6)$$

- **Current model estimate:** flux linkage in estimated rotor frame $\hat{d}\hat{q}$ is retrieved using flux maps information and measured currents:

$$\hat{\lambda}_{\hat{d}\hat{q}}^i = \Lambda_{dq}(i_{\hat{d}\hat{q}}) \quad (3.7)$$

This approach is based on the back-EMF integral, compensated by the difference between the two estimated flux from the two model estimates [26], multiplied by crossover angular frequency g [rad/s]: it is a scalar and not a gain matrix in order to simplify the control, in fact improvements will be trivial.

As it can be seen from Figure 3.8, flux observer requires knowledge of rotor angle, useful for the Park transformation in the current model estimate. On the other hand, voltage model estimate does not require rotor position information.

The transfer function of the flux observer is:

$$\hat{\lambda}_{\alpha\beta} = \frac{s}{s+g} \left(\frac{\hat{v}_{\alpha\beta} - R_s i_{\alpha\beta}}{s} \right) + \frac{g}{s+g} \hat{\lambda}_{\alpha\beta}^i \quad (3.8)$$

The voltage model estimate is high-pass filtered, while the current model one is low-pass filtered. Therefore:

- if electrical rotor speed ω is higher than g , voltage integration prevails;
- if ω is less than g , the current model prevails.

As a consequence, they both give best performance, since the first method fails at low speed due to poor voltage amount while the current model at high speed is affected by core losses [27]. The parameter g is a trade-off between accuracy of magnetic model and back-EMF in the machine: it establishes

a threshold from which the voltage quantity is sufficient for the success of voltage model estimate.

Nowadays all the controls are implemented in digital environment, so it is important to pay attention on sampling time: supposing to estimate flux linkage at k sampling instant and remembering that the discretized integral is one step ahead of the integrating signal (it is calculated at time (k) but indicates the area at time $(k + 1)$), the output of the flux observer at k time instant is:

$$\hat{\lambda}_{\alpha\beta}(k) = \hat{\lambda}_{\alpha\beta}(k-1) + T_{sw} \left(\hat{v}_{\alpha\beta}(k-1) - R_s i_{\alpha\beta}(k) - g(\hat{\lambda}_{\alpha\beta}(k-1) - \hat{\lambda}_{\alpha\beta}^i(k-1)) \right) \quad (3.9)$$

where T_{sw} is the switching period of the power modules in the inverter. The flux observed at time k is executed after current sampling and before the evaluation of $\hat{v}_{\alpha\beta}(k)$. The estimated voltage refers to the previous sampling instant, therefore one step early duty cycles are used in order to take into account the execution delay (Figure 3.9).

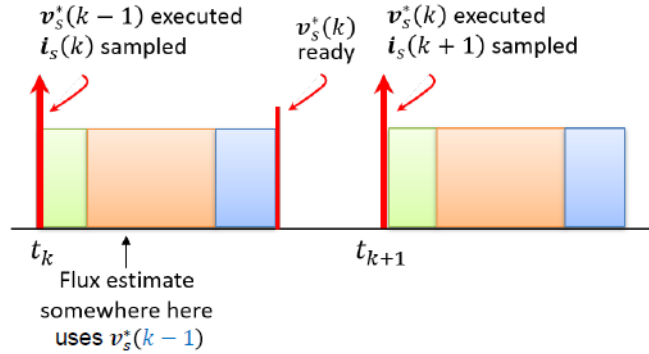


Figure 3.9: Timing of voltage and current samples [28]

In order to obtain a useful flux observer, knowledge of magnetic model machine is requested. Cross saturation effect is a common phenomena in electric motors, in particular in the ones that present anisotropy. Therefore, current and flux cannot be easily related by a constant inductance value but it changes according to working point. A wrong evaluation of flux linkage in dq frame means an inaccurate valuation in rotor position. Therefore, a detailed knowledge of the magnetic model of the machine is required when high performance of sensorless control are wanted.

Retrieving the magnetic model of the machines and so also the flux maps LUTs can be done by different methods. Paper [25] proposes an experi-

mental approach for the identification of the magnetic model of synchronous electrical machines.

As said before, it seems that, knowing accurate flux maps and integrating the back-EMF, this flux observer works well from zero to maximum speed. This is true only if the correct rotor position signal (θ) from sensor is provided to the Park transformation of the current model estimate. However, a sensorless control does not present a position/speed transducer, so the above flux observer has some limitations. In fact, in order to obtain a feasible position estimation, flux information has to come from integration of back-EMF, where rotor position is not requested. As a consequence, this method works at high speed, when back-EMF is enough. On the contrary, at low speed, current model estimate became predominant but the knowledge of θ is a prerequisite, so it will not provide the correct flux information: this is the main limitation of this flux observer.

In conclusion, the HFO is reliable only at pulsation higher than g , in the absence of closed loop position estimation at low speeds, as is the case when using the open loop I-f start. Therefore, the speed thresholds (ω_{up} and ω_{down}) must be set accordingly, imposing higher values with respect to g .

3.2.2 Flux cross-product position observer

Once flux estimation in $\alpha\beta$ and in $\hat{d}\hat{q}$ reference frames are obtained from hybrid flux observer, rotor position information can be retrieved with different methods. The one used in this thesis is the flux cross-product position observer: it is a simple but strongly reliable method.

The idea behind this method is very basic: estimating the flux linkage from back-EMF integration ($\hat{\lambda}_{\alpha\beta}$) in stationary reference frame and from current method ($\hat{\lambda}_{\hat{d}\hat{q}}$) in estimated rotating reference frame thanks to the knowledge of motor current and flux maps, it is possible to calculate the sine and cosine of the angle between the two reference coordinate with the following formulation:

$$\begin{cases} \sin(\hat{\theta}_{cr}) = \frac{\hat{\lambda}_{\hat{d}}^i \hat{\lambda}_{\beta} - \hat{\lambda}_{\alpha} \hat{\lambda}_{\hat{q}}^i}{\lambda^2} \\ \cos(\hat{\theta}_{cr}) = \frac{\hat{\lambda}_{\hat{d}}^i \hat{\lambda}_{\alpha} + \hat{\lambda}_{\beta} \hat{\lambda}_{\hat{q}}^i}{\lambda^2} \end{cases} \quad (3.10)$$

where λ^2 is the squared amplitude of the observed flux in $\hat{d}\hat{q}$ or $\alpha\beta$ frames. In fact, when the estimated angle and the real one are the same, estimated flux in $\alpha\beta$ and $\hat{d}\hat{q}$ frames have the same module λ , ignoring other errors (measurements and modelling) [27]. Particular attention is needed when

the motor is starting: initially, the estimated flux λ could be near zero. Therefore, $\frac{1}{\lambda}$ will go to a very high value, causing the loss of convergence. In order to avoid this situation, $\frac{1}{\lambda}$ is limited to an imposed maximum value, chosen according to motor characteristics.

Figure 3.10 shows the entire flux observer scheme, assembled with the flux cross-product position observer and giving as output sine and cosine of the estimated angle $\hat{\theta}_{cr}$.

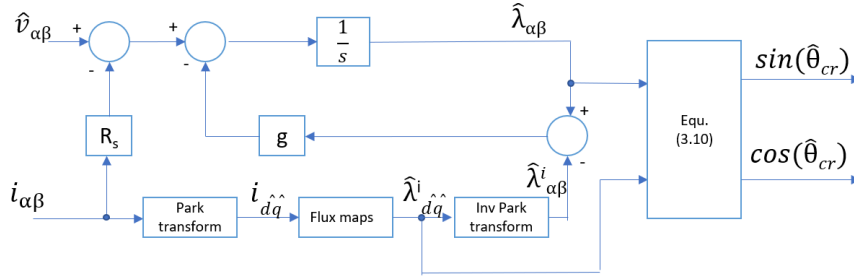


Figure 3.10: Hybrid flux observer implemented with flux cross-product position observer

Considering the digital control, this method converges to the correct angle. In fact, if difference between the real and the estimated angles is not zero, at the next sampling time the error will be reduced [27]. However, due to digital control, if the imposed sampling frequency is too low with respect to rotating speed of the motor, electrical quantities cannot be considered much faster than mechanical ones, in particular at high speed. For example, considering a motor with two pole pairs, a rated speed (n_{rat}) equal to $1800rpm$ and a sampling frequency (f_s) of $5kHz$, the magnitude of discretization will be:

$$\Delta\theta = \frac{n_{rat}\pi}{30 \cdot f_s} = 0.0376rad/s \quad (3.11)$$

This quantity corresponds to 4.32° , that is not trivial. What is important is the ratio between sampling frequency and electrical speed frequency of the motor: increasing it, $\Delta\theta$ becomes lower.

3.2.3 PLL

The estimated rotor position $\hat{\theta}_{cr}$ by flux cross-product position observer is usually noisy, therefore this signal is processed by a filter in order to eliminate some disturbing frequencies and so reducing the signal noise. Most of sensorless control methods use phased locked loop (PLL). It is located in

cascade to the hybrid flux observer with flux cross-product position observer, in fact it receives as input the difference between the estimated angle $\hat{\theta}_{cr}$ and the main output of PLL $\hat{\theta}$:

$$\epsilon = \hat{\theta}_{cr} - \hat{\theta} \quad (3.12)$$

The PLL reduces the noise of $\hat{\theta}_{cr}$ and it gives stability to the position observer.

If the estimated position angle is known, estimated speed can be retrieved from the derivative of position information. However, in digital control it is not recommended to differentiate signal since its noise is amplified. The main advantage of PLL is the possibility to retrieve the observed speed $\hat{\omega}$ in a intermediate process, integrating and not differentiating. This is a useful information since the proposed sensorless control needs a speed feedback signal. Moreover, the output angle $\hat{\theta}$ is adopted, instead of $\hat{\theta}_{cr}$, for motor control in particular for the Park transformations in the sensorless control algorithm. Figure 3.11 shows the basic PLL scheme.

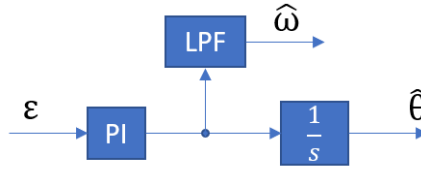


Figure 3.11: PLL block scheme

The control procedure of this scheme can be described as: the position error signal ϵ is the input of the scheme (in the next paragraph it will be discussed the adopted procedure to retrieve it). Then, this information is supplied to the properly tuned PI regulator, which gives as output the observed speed. Moreover, speed is filtered by a low-pass filter (LPF) with a cut-off frequency higher than PLL bandwidth, in order to obtain a smoother feedback speed signal. At the end, integrating the not-filtered speed signal, observed position angle $\hat{\theta}$ is obtained: it goes both to the motor control and feedback to the input of PLL.

The position error can suffer a $\pm\pi$ discontinuity, if it is simply calculated by equation 3.12. In order to avoid this problem, it is suggested to use trigonometric coordinates rather than their values in radians. Therefore, the input can be approximated to:

$$\epsilon = \hat{\theta}_{cr} - \hat{\theta} \cong \sin(\hat{\theta}_{cr} - \hat{\theta}) \quad (3.13)$$

Using the exterior product, equation 3.13 can be expressed as:

$$\sin(\hat{\theta}_{cr} - \hat{\theta}) = \begin{bmatrix} \cos(\hat{\theta}_{cr}) \\ \sin(\hat{\theta}_{cr}) \end{bmatrix} \wedge \begin{bmatrix} \cos(\hat{\theta}) \\ \sin(\hat{\theta}) \end{bmatrix} = \sin(\hat{\theta}_{cr}) \cos(\hat{\theta}) - \cos(\hat{\theta}_{cr}) \sin(\hat{\theta}) \quad (3.14)$$

However, PLL converges both with equation 3.12 and 3.14. PLL implementation with second choice is shown in Figure 3.12.

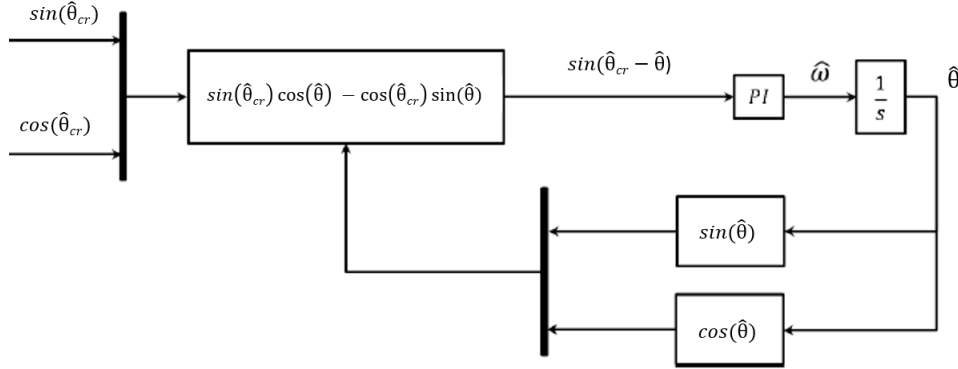


Figure 3.12: PLL block scheme with trigonometric coordinates

Different behaviors can be chosen for the tuning of the PI regulator of the PLL. The one used in this thesis is critical damping, obtained setting:

$$\begin{cases} k_{p,PLL} = 2\Omega_w \\ k_{i,PLL} = \Omega_w^2 \end{cases} \quad (3.15)$$

In particular, Ω_w corresponds to the pole position of the PLL intrinsic filter.

3.3 I-f control

As said before, the I-f control is implemented for fast and smooth transition to the sensorless field oriented control. It is widely used for its simplicity, good performance and robustness. In particular, this control is recommended for PM machines: due to the stator current control, this technique prevents the PM demagnetization [29].

The idea behind I-f control scheme is to impose a current vector with an arbitrary amplitude and frequency f^* . If this two degrees of freedom are properly set, the rotor engages with the rotating vector and they turn in synchronism.

Current references are used to produce a rotating vector of amplitude I_s [A]:

$$|\mathbf{i}_{ol}| = \sqrt{2}I_s \quad (3.16)$$

where I_s is the rms value of the imposed current vector.

There is no closed speed loop but the mechanical speed of the motor is related to the imposed frequency of the current vector. For this reason, I-f control cannot guarantee an elevate speed dynamic.

Current can be imposed both in d and q axes: according to the motor characteristics and application, some choices could produce better results. For example, in order to ensure a smooth transition from sensorless FOC to I-f control, it will be necessary to impose a reference current located in *zero torque locus*. A clearer explanation will be provided in section 3.4.2.

Figure 3.13a shows a vector diagram of the I-f control in which q reference current is imposed to zero: thus, current vector is aligned with d^* axis. If q current is not equal to zero, current vector will be always synchronous with the reference imposed d^*q^* frame and aligned with the reference angle but with the addition of an extra angle (γ_z) due to q current component (Figure 3.13b).

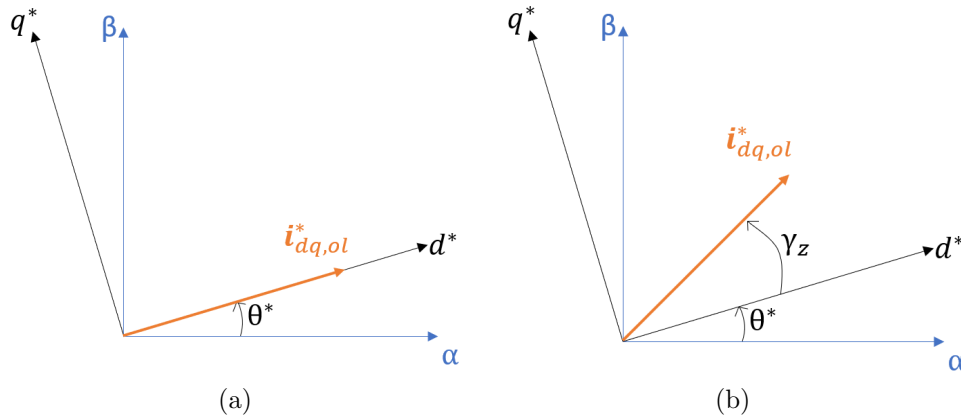


Figure 3.13: I-f control vector diagrams

In this method the d^*q^* reference frame is different from the one used for FOC, where it follows the rotor position: in I-f control, the reference frame is arbitrary and not related to the rotor position. To be clear, Figure 3.14 shows the relationship among stationary, rotor and arbitrary reference frame.

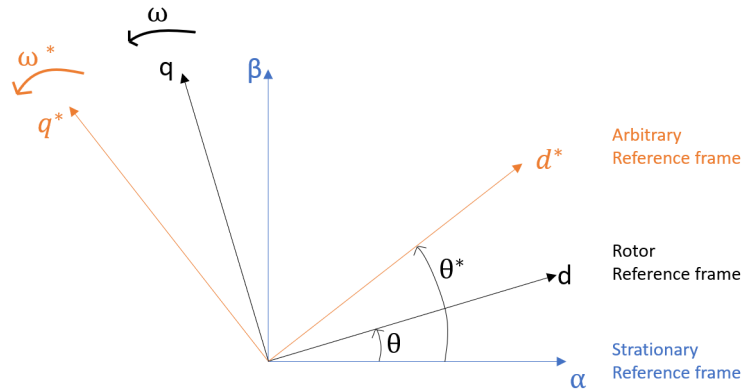


Figure 3.14: Relationship among stationary, rotor and arbitrary reference frame

The dq axes are the one used in field oriented control: its speed (ω) is equal to the electrical rotor speed, while θ represents the electrical rotor position respect to the $\alpha\beta$ stationary frame. Unlike, the d^*q^* axes are the one used in I-f control: they rotate at ω^* , which could be marginally different from ω during transients and not aligned with the rotor reference frame.

As said before, I-f control consists in ramping the stator current frequency, maintaining constant its amplitude [30]. The frequency time variation can be chosen arbitrary, according to the application. However, it is strongly recommended to impose a limited slew-rate frequency in order to ensure the correct success of the control. In fact, if it is too high, the motor will not be able to follow the rotor speed with respect to the reference speed, particularly for high inertial loads. As can be easily deduced, limitation of imposed slew-rate frequency depends from machine parameters, for example inertia has a huge impact. In this thesis, it is chosen to implement a linear ramping frequency variation (as shown in Figure 3.15):

$$f^* = k_f \cdot t \quad (3.17)$$

where k_f is the slew-rate coefficient and t is the time.

Once the reference frequency is imposed, the electrical arbitrary reference angle θ^* can be retrieved:

$$\theta^* = \int 2\pi f^* dt \quad (3.18)$$

This is a fundamental information because θ^* establishes the position of the d^* axis with respect to the the α axis of the stationary frame. In addition, this information is essential for the Park transformation of the stator currents. Figure 3.15 illustrates the control scheme of a I-f control.

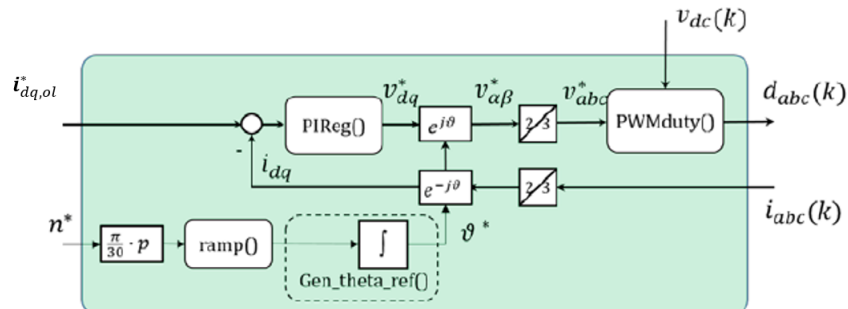


Figure 3.15: I-f control scheme [28]

To conclude, the main drawbacks of this control are:

- Underdamped dynamic response;
- Limited capacity to withstand the load torque because the current cannot increase in amplitude: if the required torque corresponds to a current amplitude greater than the reference one, the motor loses reference speed and it diverges.

Appendix A presents the algorithm for a correct implementation of I-f control.

3.4 Transition strategies

The control strategy uses I-f control for start-up and low speed operating points. When the motor reaches the threshold speed (ω_{up}), the control automatically jump from I-f control to sensorless FOC. This transition needs to be as smooth as possible, in order to avoid discontinuities in speed. In literature, this problem is widely discussed and different solutions are found in these years: papers [31]-[32]-[33] are only some examples that can be used.

However, this thesis proposed a different method that consists in a fast jump between the two types of control described in 3.3 and 3.2, taking into account some precautions in order to obtain a smooth speed transition and avoid divergence of the control. A clear explanation is provided in the next subsections.

The proposed sensorless strategy uses hysteresis technique for transition rule: speed threshold ω_{up} (transition I-f \rightarrow FOC) and ω_{down} (transition FOC \rightarrow I-f) are such that $\omega_{up} > \omega_{down}$.

3.4.1 Up transition

I-f control and sensorless FOC are based on different reference frame (respectively arbitrary and estimated rotor position from the flux cross-product position observer), not directly connected each other. For this reason, when the jump occurs the electric characteristics (current, voltage and flux) move, in a sampling time, from imposed d^*q^* reference frame to estimated synchronous rotor $\hat{d}q$ frame. Therefore, current and voltage vectors before and after the jump could be different, causing respectively a voltage and current vector discontinuity in amplitude, as well as in phase. Figure 3.16 highlights this concept, showing the reference current vector just before the jump ($k-1$ sampling time) and after the jump (k sampling time).

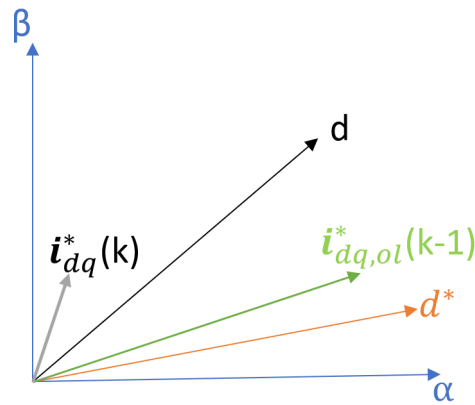


Figure 3.16: Transition diagram vector

When the jump occurs, motor current reference vector moves, in a sampling time, from $i_{dq,ol}^*$ (I-f control) to i_{dq}^* (Sensorless FOC), causing a reference current discontinuity. But, if properly precautions are adopted, these events will not cause divergence of the control:

- Hybrid flux observer and PLL need to be always active, but if reference speed (ω^*) is lower than an imposed threshold (ω_{act}), PLL is partially active:
 - Position error ϵ is imposed to zero;
 - estimated electrical angle from PLL is imposed equal to reference phase angle: $\hat{\theta} = \theta^*$;
 - integrative part of PLL is fixed to the reference speed ω^* .

As a consequence, the PLL is adequately initialized with a good real rotor position estimate before transition to the high speed model. If

speed slew-rate is small enough and the I-f control is properly tuned, the real motor speed will be almost equal to the reference one, during starting procedure. Therefore, the estimated speed will be almost the same of the real one ($\hat{\omega} = \omega^* \cong \omega$).

- When the jump occurs, the initial value of the integrative part of the PI speed regulator is properly setted in order to avoid torque discontinuity in the control. The best initial condition is $T^* = \hat{T}$, where \hat{T} is the estimated torque, retrieved using the observed flux (HFO's output):

$$\hat{T} = \frac{3}{2}p(\hat{\lambda}_\alpha i_\beta - \hat{\lambda}_\beta i_\alpha) \quad (3.19)$$

Thanks to these precautions, the drive could present, for a sampling time, a discontinuity in reference current while the estimated speed will have a smooth waveform: the control does not diverge.

3.4.2 Down transition

Restrictions in down transition are more severe than up transition. As before, also in jump from sensorless FOC to I-f control the two reference frame (respectively $\hat{d}q$ and d^*q^*) are completely unrelated. Therefore, during the jump instant, there could be the discontinuity problem, in phase and amplitude, of the current and voltage vectors. In order to obtain a speed transition as smooth as possible, the following precautions need to be adopted:

- Impose in I-f control a reference current vector located in *zero torque locus*. In fact, I-f control is inherently unstable for dq operating points on and over the MTPA trajectory. This is because we are keeping the current magnitude constant, so when a small load increment is applied at MTPA, the control moves ahead where the torque in fact decreases and eventually loses control. As we use MTPA at high speed, it is desirable to move as far away from MTPA as possible when jumping to I-f and here, zero torque locus provides a safe solution. Moreover, speed slew-rate during deceleration is set quite low, in particular around ω_{down} . Therefore, the needed torque to reduce the motor's speed is really low (around $0Nm$). In order to avoid torque disturbances during the transition between sensorless FOC and I-f control, the best solution is to choose d and q currents that provide a null torque. This solution complicates the control strategy because, starting from the flux maps used in HFO, the magnetic data of the machine need to be elaborated

in order to retrieve *torque maps*, where the torque values are correlated to d and q currents. In conclusion, tuning of I-f control is much complicated due to the aforementioned restriction: the reference current needs to be properly chosen according to the magnetic model of each machine. This argumentation will be validated by simulation and experimental results.

- The reference angle θ^* is initialized to the estimated angle $\hat{\theta}$ just before the jump. In this way, the two rotating reference frame will be almost synchronized after the jump. This precaution is successful only if the reference speed and the estimated speed are the same before the jump. For this reason the speed slew-rate cannot be too high in proximity of the threshold speed ω_{down} , otherwise synchronization will be lost after jump, causing oscillation and acoustic noise in the drive system. As a consequence, in order to guarantee the control success, it is strongly suggested to use the desired speed slew-rate during sensorless FOC, but reduce it to a quite low value (according to machine's characteristics) near the threshold speed ω_{down} .

In the simulation and experimental results, the same reference current components located in *zero torque locus* for the down transition are used also for the up transition.

The aforementioned consideration about the partially PLL activation below a certain speed ω_{act} is also applied for down transition. This choice will guarantee a successful up transition, if the user wants to return to high speed after a stop of the motor.

Chapter 4

Simulation results

The content of this chapter can be divided in two arguments:

- **Motor data:** description of the main characteristics of the motor under test, focusing on machine details that concern the sensorless control strategy (torque map, MTPA trajectory and so on);
- **Simulation results:** preliminary tests in *simulink* environment are carried out in order to understand benefits and limitations of the flux cross-product position observer.

4.1 Motor data

The machine used in this thesis is produced by ABB-Baldor. It is an IE5 (Ultra Premium Efficiency) motor of the EC-Titanium family [34]. In order to obtain a high efficiency, ensuring low cost, the chosen typology is a PM-assisted synchronous reluctance motor, with a small quantity of permanent magnets allocated inside the rotor.

It is a three phase machine with 7.5 hp and a rated speed equal to 1800 rpm. As it can be seen from Figure 4.1, the electric machine has a total enclosed fan cooled (TEFC) and it does not inherently have a speed/position transducer: a magnetic encoder was later externally mounted (Figure 4.2) by laboratory technicians in order to check the correct operation of the sensorless control strategy.



Figure 4.1: ABB-Baldor motor

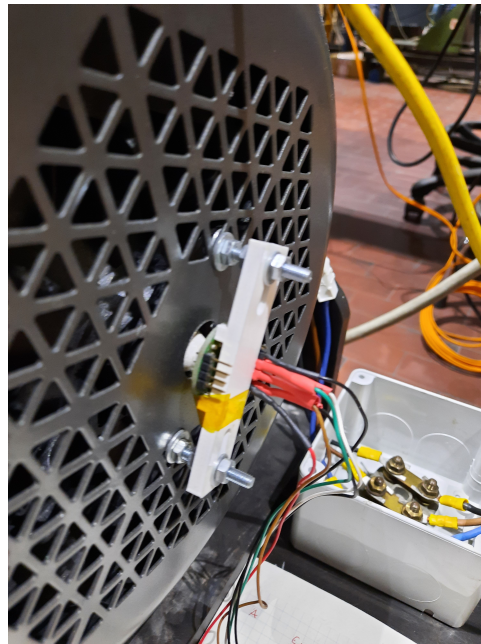
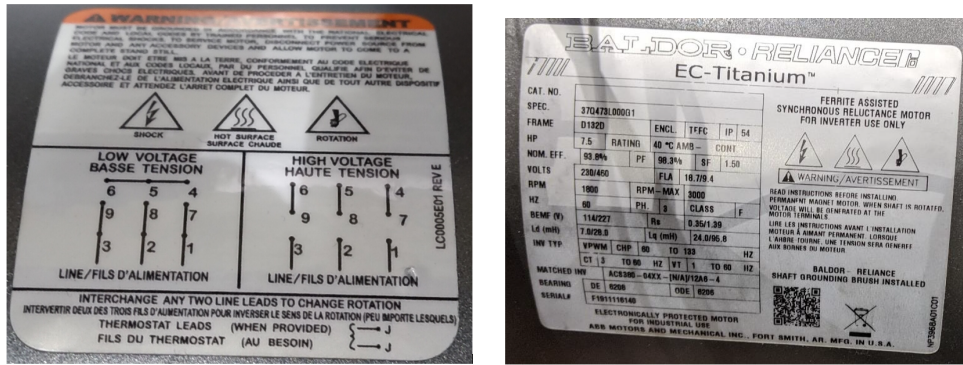


Figure 4.2: External mounted magnetic encoder

The motor can work in two configurations: high voltage (460V) and low voltage (230V). Figure 4.3a illustrates the difference between these two connections. The one used in this thesis is the low voltage configuration. Figure 4.3b shows the nameplate allocated on the motor. The number of turns is $N_s = 94$.



(a) HV and LV motor configuration

(b) Motor parameters

Figure 4.3: Motor nameplate

Table 4.1 contains all the main motor parameters, taking into account the low voltage configuration. These results are also validated by comparison of experimental and FEA derived flux maps.

Table 4.1: ABB motor parameters with low voltage configuration

Parameter	Value
Rated Power (P)	5.52 kW
Rated Torque (T)	29.8 Nm
Rated Current (I_r)	16.3 A
Rated Voltage (V)	260.3 V
SF	1.5
Rated speed (n)	1800 rpm
Rated frequency (f)	60 Hz
Pole pairs (p)	2
Stator resistance (R_s)	0.46Ω
L_d	0.024 H
L_q	0.007 H
Power factor (PF)	98.3%
Efficiency	93.8%

The friction coefficient B and motor inertia J are not provided in the nameplate or motor documentation. However, they are important parameters to properly tune the control.

- Friction coefficient is retrieved from no-load measures on this machine. The only problem is due to the PMs: no load loss are equal to me-

chanical loss (friction, windage) and iron loss due to PM flux linkage. By the way, this error can be neglected. Moreover, this parameter depends from the motor speed, but for a preliminary analysis it can be considered constant and equal to $0.0015 \text{ Nm} \cdot \text{s}$.

- The rotor inertia has been computed from FEMM simulation and it can be assumed equal to $0.0244 \text{ kg} \cdot \text{m}^2$. However, the test bench includes another electric machine used as load and coupled to the motor under test. For this reason, the total inertia is estimated to $J = 0.0544 \text{ kg} \cdot \text{m}^2$.

The aforementioned ABB motor presents an anisotropic stator, characterized by a cut for each pole (Figure 4.4). This could cause disturbances in electrical waveforms, introducing higher harmonic content: a second harmonic contribution is expected. In order to improve motor behaviour, ABB chose to step-skewed the motor to cancel the 18° electrical harmonic, corresponding to the stator slots. This is beneficial for the 2nd harmonic too, reducing its intensity. However, a 2nd harmonic effect is still expected at low-load condition, where a poorly stator flux amount could saturate the back-iron in a non-homogeneous way, according to its location.

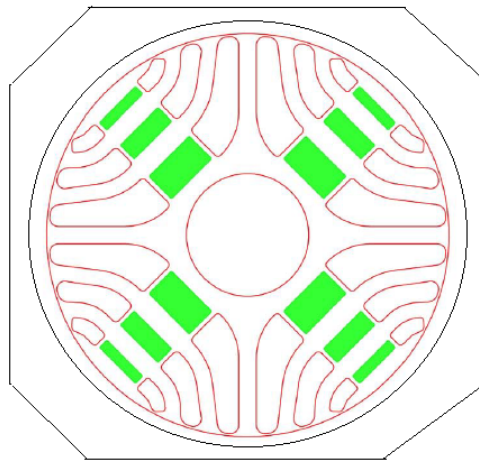


Figure 4.4: ABB stator and rotor design

Moreover, sensorless control will be negatively impacted by this situation: due to harmonic contribution, the hybrid flux observer, which uses average flux maps in current model estimate, does not provide the exact value of estimated flux, inducing an oscillating position error $\tilde{\theta}$.

In the following subsections additional useful motor data, for the success of the adopted sensorless control strategy, will be presented.

4.1.1 Flux maps

As mentioned in subsection 3.2.1, flux maps are necessary in order to estimate d and q flux linkage: in fact, they relate machine current and flux. In anisotropic electrical machines this relation is non-linear because of saturation behaviour of ferromagnetic materials and for the cross-coupling between d and q axes [35]. Figure 4.5 illustrates flux maps characteristic: this information is provided as an input because it is not the focus thesis.

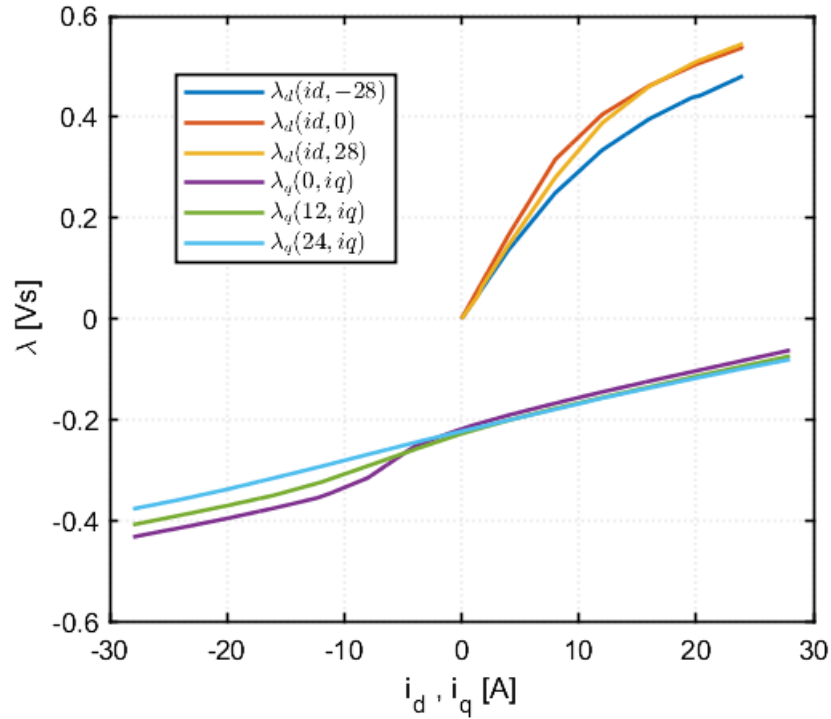


Figure 4.5: ABB motor flux maps

These flux maps are retrieved by an experimental approach. As said before, they are averaged: harmonic contribution is not taken into account. Therefore, it causes a problem in the HFO because the estimated flux will not include harmonic effect of the real machine used in the experiment.

In particular, Figure 4.5 represents six trajectories: three for λ_d , changing i_q ($-28A, 0A, 28A$), and three for λ_q , changing i_d ($0A, 12A, 24A$). In this way, cross-coupling is highlighted. From this figure, it can be observed the following:

- When $i_d = 0A$ and $i_q = 0A$, $\lambda_q = \lambda_m = -0.2189Vs$: this is the

permanent magnets flux contribution. Therefore, it demonstrates PMs are located along q -axis, in fact in the same conditions $\lambda_d = 0Vs$;

- Cross saturation effect cannot be trivial;
- The differential anisotropy is relevant. However it tends to disappear when d -axis is deep saturated.

Figure 4.6 illustrates current and flux vectors in $d - q$ frame. Unlike the synchronous reluctance motor, which presents flux vector (orange) in the first quadrant, the PM-assisted SyR motor, due to PM contribution, shows a total flux vector in the fourth quadrant (green), near d -axis.

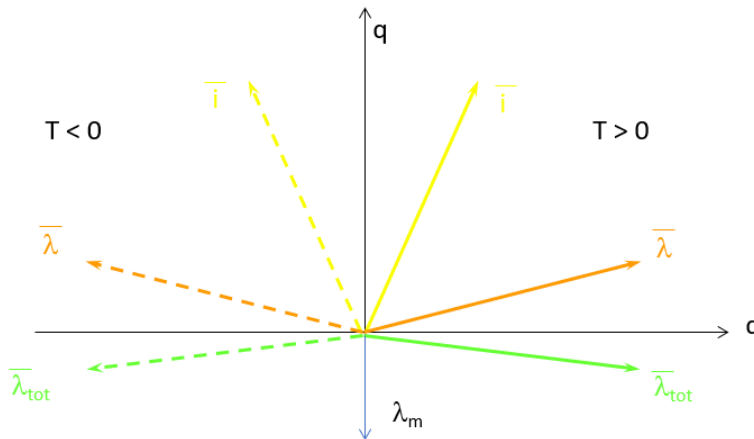


Figure 4.6: Diagram vector of a PM-assisted SyR motor

As it can be seen, i_q component must be always opposite to PM flux contribution: if i_q is negative, the effect of the magnets would be such as to worsen the situation, by moving further away from the MTPA operating point. Therefore, inverse torque is obtained changing the sign of i_d current component. As a consequence, the situation is symmetrical in the second quadrant, obtaining a negative torque.

In conclusion, flux locus versus i_d or i_q axis is showed in Figure 4.7.

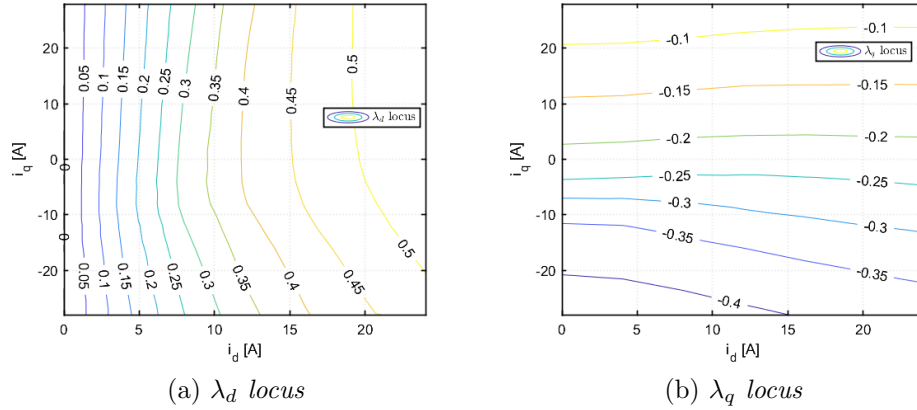


Figure 4.7: Flux locus

4.1.2 MTPA and Torque locus

A fundamental information to increase FOC efficiency is the MTPA trajectory. Thanks to it, the control will spend the minimum current amplitude to serve the torque load, minimizing Joule losses.

The MTPA curve matches for each torque value a unique i_d and i_q current component. It can be found mathematically manipulating the flux curves in Matlab environment or with an experimental iterative approach, using a torque transducer. In this thesis, MTPA is an input data. Figure 4.8 shows the MTPA trajectory (red curve) in i_d and i_q axes.

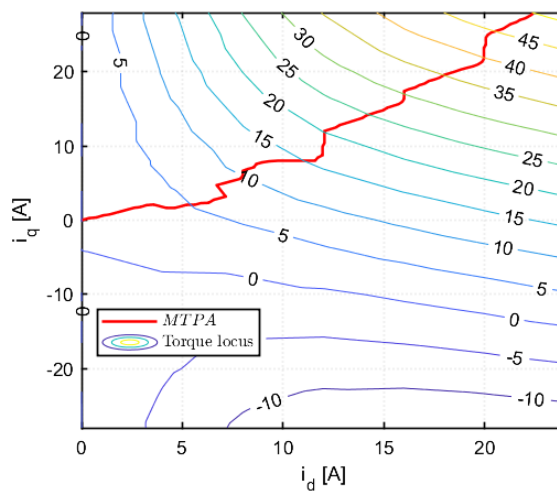


Figure 4.8: MTPA trajectory and torque locus

As mentioned in subsection 3.4.2, in order to guarantee a smooth transition from sensorless FOC to I-f control, the reference current components ($i_{d,ol}^*$ and $i_{q,ol}^*$) need to be allocated in zero torque locus during I-f control. Therefore, a torque map is requested. Figure 4.8 shows the torque map for the considered ABB motor. The zero torque locus is not allocated along x axis due to the presence of magnets.

4.1.3 Motor inductance

Knowledge of incremental and apparent inductances can be a useful information for a correct current loop tuning.

- **Apparent inductance:** it is the ratio between rated flux and rated current.

$$L_d = \frac{\lambda_d}{i_d} \quad ; \quad L_q = \frac{\lambda_{q0}}{i_q} \quad (4.1)$$

where λ_{q0} is the q -axis flux linkage related to machine current.

- **Incremental inductance:** it is the flux derivative respect to the current.

$$l_d = \frac{d\lambda_d}{di_d} \quad ; \quad l_q = \frac{d\lambda_q}{di_q} \quad (4.2)$$

According to intensity and stability of dc-link voltage supply, the maximum speed that the machine can reach in every load condition, exploiting MTPA trajectory, can be mathematically retrieved. As it will be described in the next chapter, the test bench is supplied by an autotransformer, which maintains the capacitor dc-link voltage to 360 V when the motor works at no load. Due to the weakness of the supplied grid, this voltage is not constant but it changes according to motor load conditions: the higher load the motor has to sustain, the lower is dc-link voltage. In particular, at rated torque load, the dc-link voltage goes to 333 V. Considering steady state condition, the maximum speed is retrieved by:

$$\omega_{max} = \frac{k_v \frac{V_{dc}}{\sqrt{3}}}{\lambda} \quad (4.3)$$

where λ is the module of flux linkage and k_v is a coefficient that takes into account all voltage drops in the drive: it is reasonably fixed to $k_v = 0.93$.

Figure 4.9 shows maximum speed limit (green curves) when dc-link voltage is set to 333 V.

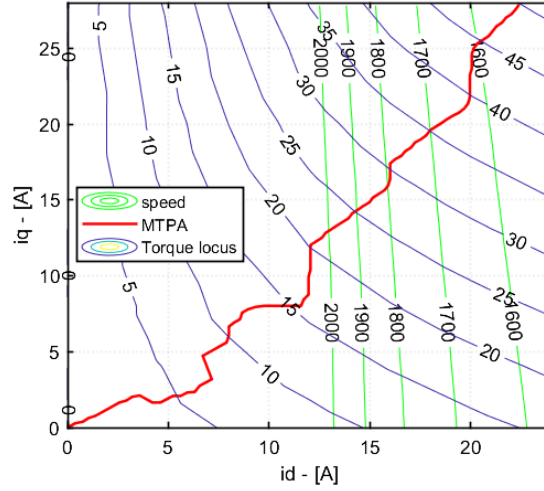


Figure 4.9: ABB speed locus when $V_{dc} = 333V$

As it can be seen from the above figure, in this particular test bench configuration with a weak grid supply, motor can reach a maximum speed equal to 1800 rpm when it work at rated torque load (29.8 Nm). This deduction will be validated by experimental results (see subsection 5.3.3).

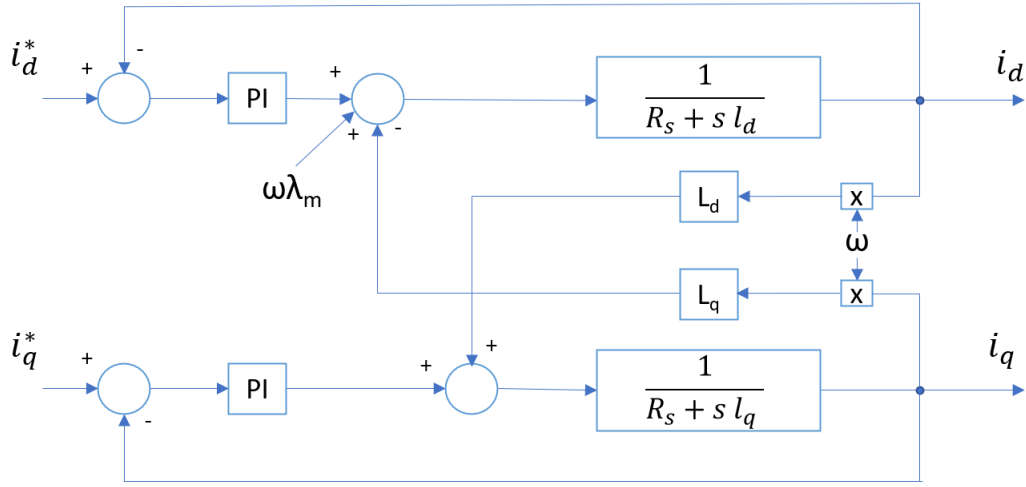
4.1.4 Current loop

The control strategy adopted in this thesis requires three PI controllers during sensorless FOC stage: two of them are used to regulate d and q current components.

The electrical model of PM-assisted SyR motor, represented in equation 2.1, can be also expressed using inductances:

$$\begin{cases} v_d = R_s i_d + l_d \frac{di_d}{dt} - \omega(L_q i_q - \lambda_m) \\ v_q = R_s i_q + l_q \frac{di_q}{dt} + \omega L_d i_d \end{cases} \quad (4.4)$$

As it can be seen from equation 4.4 and Figure 4.10, the system model of the considered machine presents cross-couplings between q and d axes: $\omega(L_q i_q - \lambda_m)$ and $\omega L_d i_d$. Therefore, feed-forward voltages control will be used in order to decouple the two axes.

Figure 4.10: Current loop block diagram in dq coordinates

Considering v_d^* and v_q^* as the PI current controllers outputs, the new inputs of *PWMduty* block, with dynamic decoupling implementation, are:

$$\begin{cases} v_d = v_d^* - \omega(L_q i_q - \lambda_m) \\ v_q = v_q^* + \omega L_d i_d \end{cases} \quad (4.5)$$

The PI controller involves only two parameters for the tuning: proportional term (k_p) and integral term (k_i). Therefore, the closed-loop transfer function of a PI controller is:

$$H(s) = k_p + \frac{k_i}{s} \quad (4.6)$$

Once the two axes are decoupled and neglecting stator resistance voltage drop, the closed-loop transfer function for each axis is:

$$H_d(s) = \frac{k_p s + k_i}{l_d s^2 + k_p s + k_i} \quad (4.7)$$

$$H_q(s) = \frac{k_p s + k_i}{l_q s^2 + k_p s + k_i} \quad (4.8)$$

The system poles are the roots of denominator equation $D(s) = 0$:

$$s_d = \frac{-k_p \pm \sqrt{k_p^2 - 4l_d k_i}}{2l_d} \quad (4.9)$$

$$s_q = \frac{-k_p \pm \sqrt{k_p^2 - 4l_q k_i}}{2l_q} \quad (4.10)$$

The approach used to calibrate current loop is directly based on experimental trial and error method on the real test bench. The best tuning parameters retrieved for both axes are:

$$k_p = 20 \quad ; \quad k_i = 2000 \quad (4.11)$$

Therefore, considering rated conditions, $i_d = 16A$ $i_q = 16.5A$ (see Figure 4.8) and $l_d = 14$ mH $l_q = 5$ mH, the poles position in d and q axes are:

- $s_{d,1} = -108$ rad/s, $s_{d,2} = -1320$ rad/s;
- $s_{q,1} = -102$ rad/s, $s_{q,2} = -3900$ rad/s.

As it can be deduced, poles are located in the real negative axis, thus the current loop behaviour is over-damped. There is further room for improvement in terms of tuning: for example the adaptive gain, which uses the l_d and l_q of the operating point for a uniform dynamics.

4.1.5 Challenges motor

The ABB motor adopted in this thesis is a low voltage configuration PM-SyR machine and it has some peculiar challenges that are hitherto not been encountered for other machines, in particular if it will be controlled with a sensorless strategy. In fact, the chosen sensorless method is based on a fundamental model sensorless technique where a sufficient back-EMF is needed to obtain a successful control.

Typically, the PM machines have sufficient no load flux to not require additional excitation for reliable back-EMF at no load. Hence, the low speed threshold ω_{up} is usually set to 20% of the rated speed.

However, from experiments/simulations, it was found that for this machine, 400 rpm (22.22%) is a better choice due to the small quantity of magnets ($\lambda_m = -0.21$ Vs). If lower speeds are required, a deviation from MTPA towards the fourth quadrant for low loads can be investigated.

4.2 Simulink environment

Before implementing the control code directly on the test bench, it is a good practice to test it in simulink environment. In this way, if a fatal error is committed, real drive components are not destroyed. However, some motor aspects could be neglected to not weigh down the simulation.

Figure 4.11 emulates the complete real machine drive, in simulink environment.

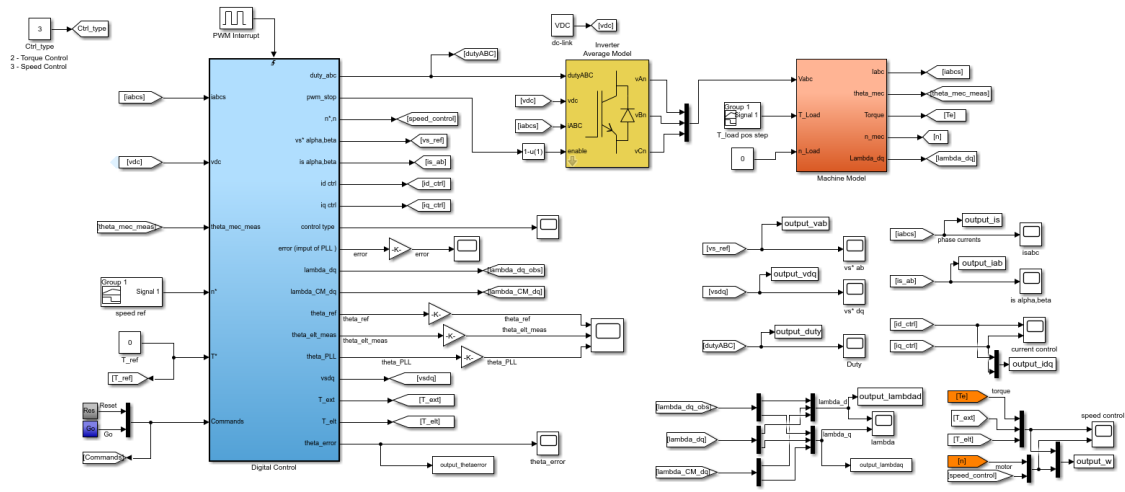


Figure 4.11: Simulink model

There are three principal blocks:

- Digital control:** its purpose is to simulate the behaviour of a micro-controller and therefore it contains the control algorithm written in C language. Going inside the block (Figure 4.12), it can be seen the useful inputs signals and the main outputs used for the next subsystems or to plot some waveforms. In particular, z^{-1} block emulates the execution delay of the digital control. The control code is contained in *S-Function* block. The digital control block is triggered at the sampling/switching frequency (10 kHz) while the simulation time step is $2\mu s$.
- Inverter average model:** The 3-phase inverter model is a custom-built block based on a S-Function named *inverter.c*. The benefits of an average model is less complexity and faster time simulation, maintaining anyway a tolerable converter dynamic accuracy. Such S-Function generates phase to neutral voltage signals, starting from the duty-cycle and dc-link voltage supply. Moreover, having the phase currents as input, the model includes the dead-time and ON-state voltage effects.
- Motor model:** mathematical equations of a PM-SyR machine are implemented in this subsystem in order to emulate the behaviour of motor under test. This system includes the average *inverse flux map* of the real machine, therefore harmonics contribution is neglected in simulink environment.

$$k_p = 2\Omega_s J \quad k_i = \Omega_s^2 J \quad (4.12)$$

Speed-loop position pole is set to 0.5 Hz or 1 Hz, obtaining respectively 1.25 Hz and 2.5 Hz speed bandwidth. In addition, the maximum output of the PI controller is fixed to $44.5Nm$ (1.49 p.u.), in order to not stress too much the motor.

In order to obtain a sufficient back-EMF amount for the fundamental model sensorless technique, threshold speed are fixed to: $\omega_{up} = 400$ rpm and $\omega_{down} = 300$ rpm.

Once speed and current PI controllers are tuned, the best speed dynamic machine behaviour is obtained with the following acceleration and deceleration slew-rate:

- 100 rpm/s during acceleration in I-f control;
- 15000 rpm/s during acceleration in sensorless FOC;
- 800 rpm/s during deceleration in sensorless FOC, but when the reference speed reaches 500 rpm, deceleration slew-rate is fixed to 100 rpm/s;
- 100 rpm/s during deceleration in I-f control.

Unless high dynamics are necessary, a lower slew-rate is generally recommended to avoid stability problems.

Taking in account the hybrid flux observer, the unique parameter that can be calibrated is the crossover angular frequency: it is set to $g = 2\pi 10$ rad/s.

Finally, PLL tuning is considered. As shown in subsection 3.2.3, critical damping behaviour is chosen, fixing the poles position to 15 Hz. In order to avoid huge input discontinuities, ϵ is limited to $\pm 20^\circ$. Moreover, the threshold speed to enable the PLL ω_{act} is imposed to 100 rpm/s: if reference speed is less than this value, PLL is partially active, where the position error signal is artificially set to zero to avoid saturating the integrator. Eventually, estimated speed is low-pass filtered: cut-off frequency is set to 25 Hz.

In conclusion, the similar settings are used both in simulation and experimental environment.

4.3 Simulation results

Several simulations are carried out in order to verify robustness of the adopted control strategy:

- Acceleration and deceleration tests at no load, under three different scenarios:
 - Using reference current vector allocated in zero torque locus;
 - Using reference current vector on d -axis;
 - With no dead-time compensation;
- Tests under nominal torque load.

In the following subsections, simulation results are reported using the settings mentioned in the 4.2.1. In particular, we are focused on these variables:

- **Speed:** estimated speed $\hat{\omega}$, reference speed ω^* and measured speed ω ;
- **Torque:** estimated torque \hat{T} , reference torque T^* and measured torque T ;
- **Current:** reference current i_{dq}^* and measured current i_{dq} ;
- **Flux:** estimated flux $\hat{\lambda}_{dq}$ and measured flux λ_{dq} ;
- **Position error $\tilde{\theta}$:** difference between measured and estimated electrical rotor position angle: $\tilde{\theta} = \theta - \hat{\theta}$.

The estimated torque and flux $\hat{\lambda}_{dq}$, which comes from the HFO, are only reliable at speeds greater than w_{act} .

4.3.1 Acceleration and deceleration tests at no load

In order to verify the speed dynamic, two tests with a different speed-loop bandwidth are carried out: 1.25 Hz and 2.5 Hz.

These tests are focused on stability of the control strategy at no load condition and rated speed (1800 rpm), being also careful on the two transition stages (in up and down). Figure 4.13 refers to the test with the lowest speed bandwidth case.

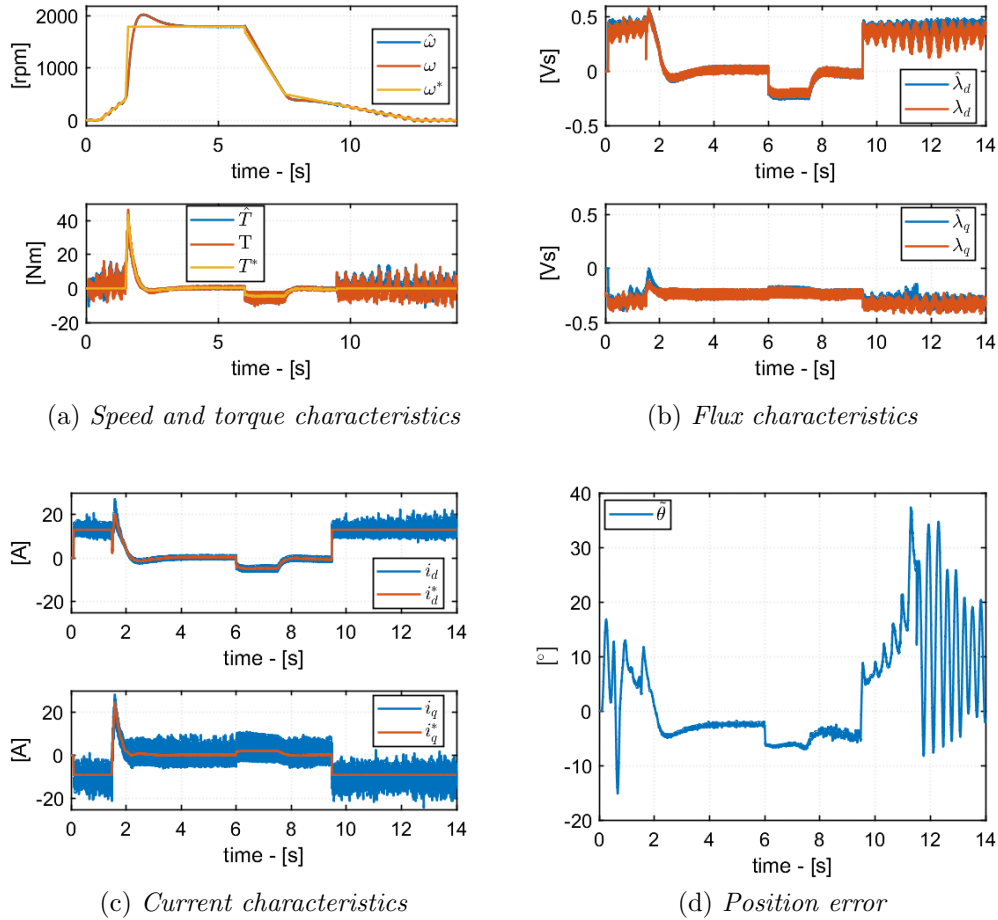


Figure 4.13: Acceleration and deceleration test at rated speed and no load, with 1.25 Hz speed bandwidth

As it can be seen, estimated speed and real motor speed present a smooth behaviour, also during transition stage. Therefore, the adopted precautions are successful. The low speed bandwidth causes a big velocity overshoot, reaching 2000 rpm. During deceleration, in particular when the implemented algorithm jumps to I-f control, the real motor speed presents a little oscillatory waveform, due to the inherent nature of open-loop speed control.

Due to the no load condition at rated speed, current is very low, almost zero. The cross-product method in simulink environment provides good results also in this condition, avoiding lost of convergence.

In order to verify the robustness of the adopted strategy, position error angle is assessed. It should be as small as possible. In this way, the estimated rotor position angle is almost the same of the real one. As it can be seen

from figure (d), during steady state sensorless FOC, $\tilde{\theta}$ is around -3° : it means that sensorless control is working well, but we would have expected zero position error signal in ideal simulation environment. However, this problem is correlated to digital discretization, discussed in subsection 3.2.2: in fact, if we increase the switching/sampling frequency, the position error signal will reduce at steady state.

Figure 4.14 presents the same aforementioned test but with 2.5 Hz speed bandwidth.

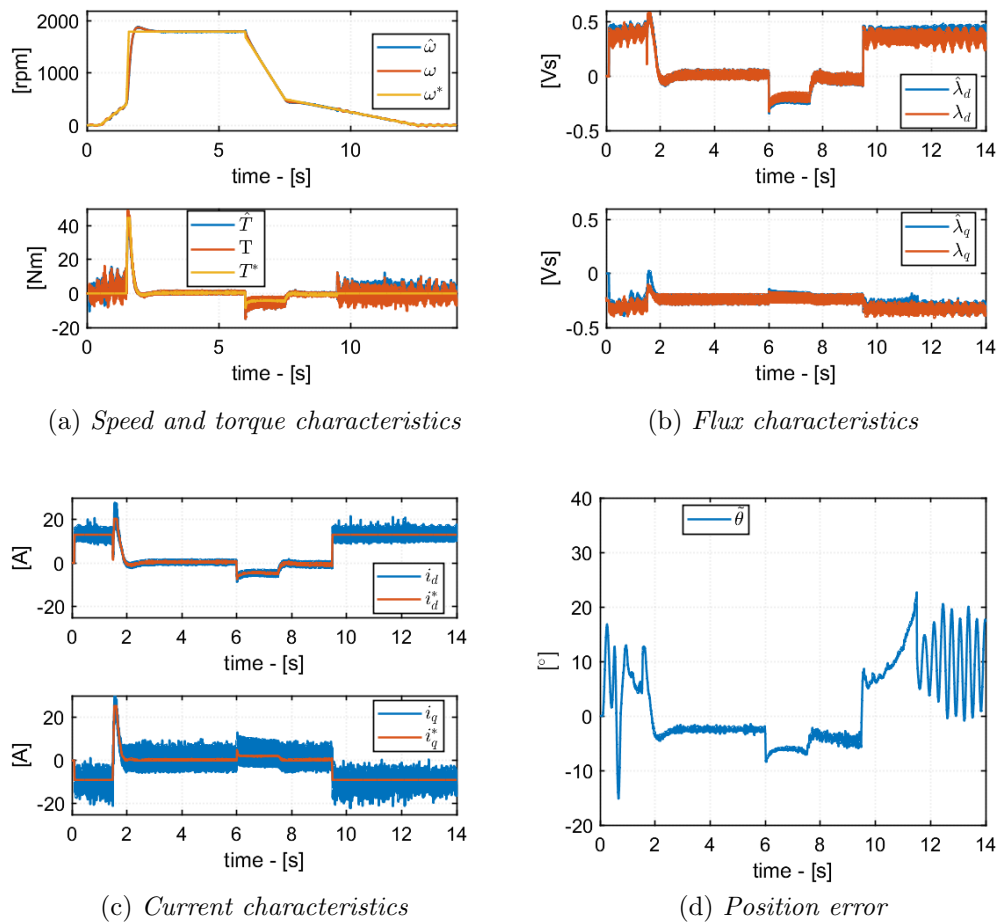


Figure 4.14: Acceleration and deceleration test at rated speed and no load, with 2.5 Hz speed bandwidth

Obviously, increasing speed bandwidth, speed overshoot during acceleration is limited, reaching 1900 rpm. The speed dynamic is faster and it is visible both during acceleration and deceleration. The success of the control

is not invalidated by the higher dynamic, in fact the control is just as stable for the higher bandwidth of 2.5 Hz as it is for 1.25 Hz.

4.3.2 Reference current vector along d-axis

In order to demonstrate the importance of the chosen reference current during I-f control, Figure 4.15 presents the same test shown in 4.3.1 with 1.25 Hz speed bandwidth, but with a reference current vector located along d^* -axis during I-f control. In particular, for coherence, it is chosen a vector current with the same amplitude ($16A_{pk}$) of the one usually used in other tests.

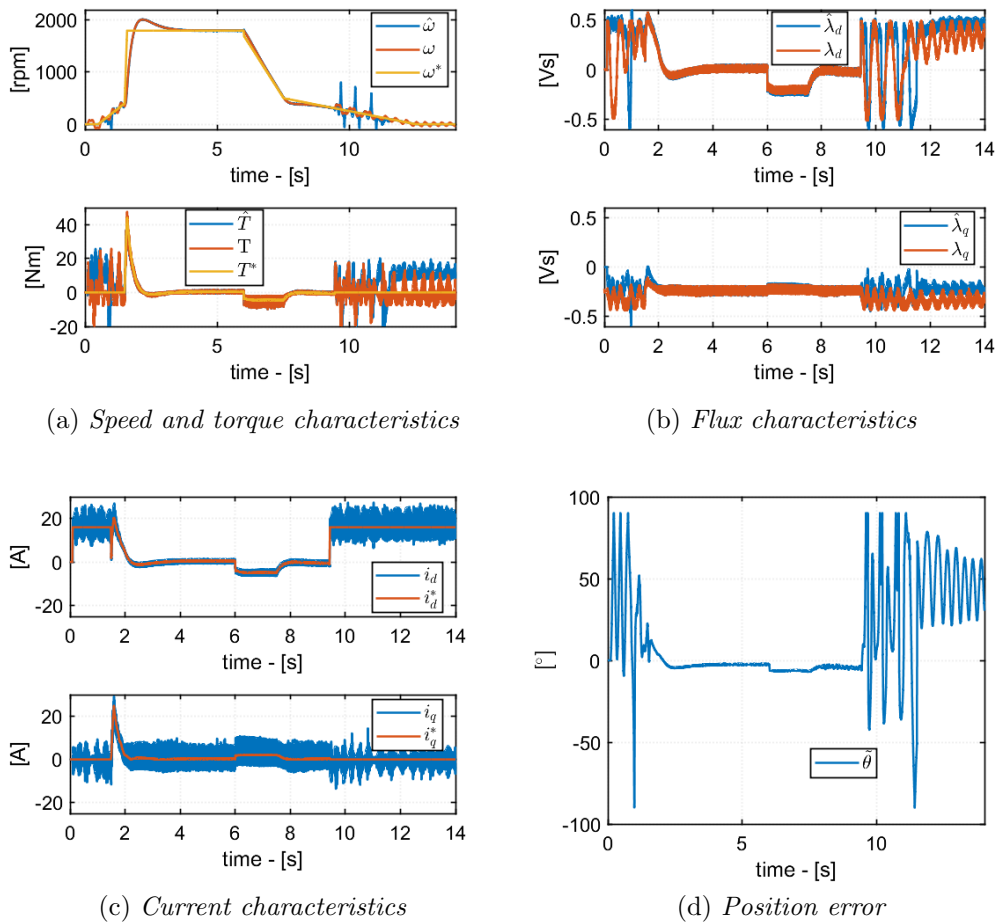


Figure 4.15: Acceleration and deceleration test at rated speed and no load, using a reference current vector along d -axis during I-f control

As it can be seen from figure (a), during the first 0.5s of simulation, the

real motor speed oscillates around zero value. However, this behaviour would be damped if the motor speed is controlled to $0rpm$ for an higher range time (eg. 5s), thanks to the motor friction and inertia.

The real problem is when the control jumps from sensorless FOC to I-f control, in fact due to the new chosen reference current vector, a large torque ripple can be observed at the moment of transition. However, the control eventually stabilizes and do not diverge. Despite the high torque ripples in the real torque, the real speed remains relatively smooth: the torque oscillations are a high frequency which is probably filtered by the inertia.

In conclusion, if torque map information is known, it is always better to impose a reference current vector in zero torque locus during I-f control. This statement will be also validated in experimental results.

4.3.3 Dead-time compensation OFF

The purpose of this subsection is to verify if dead-time compensation is useful for the success of the adopted control strategy. In fact, in all the above tests, the control algorithm implements dead-time compensation in order to properly estimated the stator voltage used as input in hybrid flux observer.

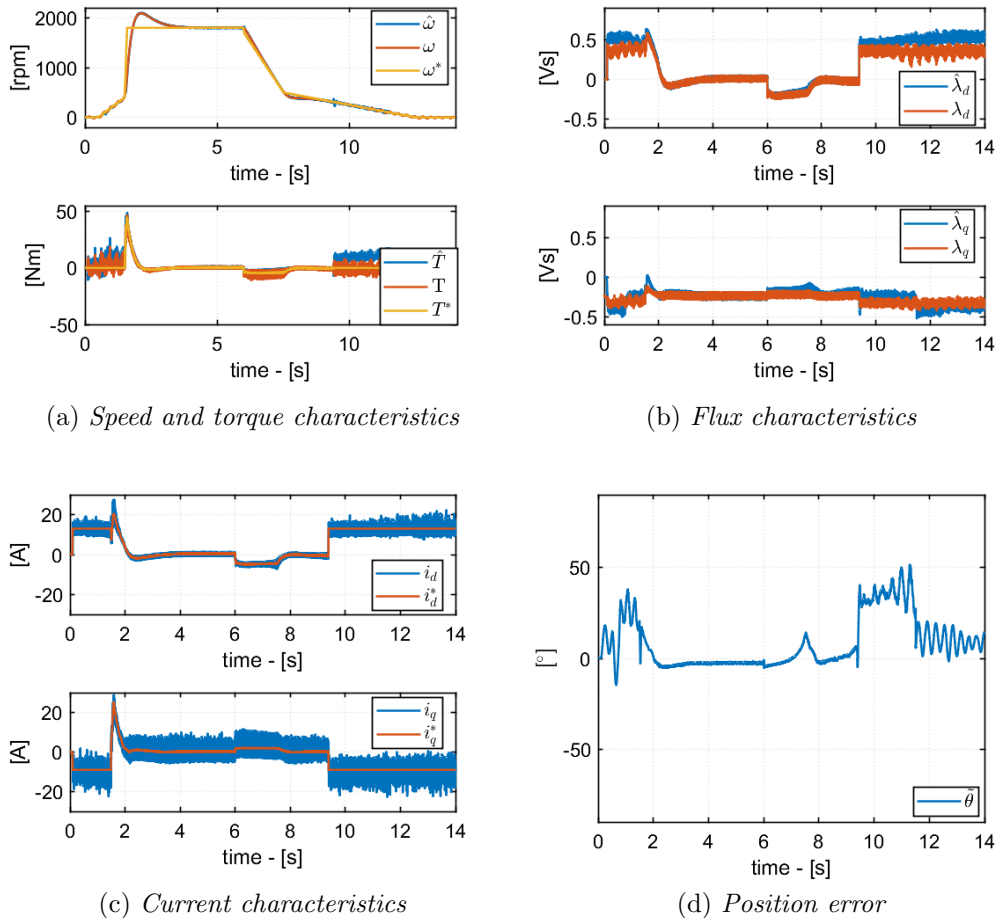


Figure 4.16: Acceleration and deceleration test with no dead-time compensation ($2\mu s$)

In Figure 4.16, inverter deadtime is fixed to $2\mu s$ while the the control code does not compensate it. As it can be seen, such dead-time does not cause evident problems during sensorless FOC, in fact position error is almost the same of the compensated case (see Figure 4.13): this further suggests the steady-state position is not due to voltage errors such as dead-time or

resistance (which are anyway less significant at rated speed) but because of the discretization.

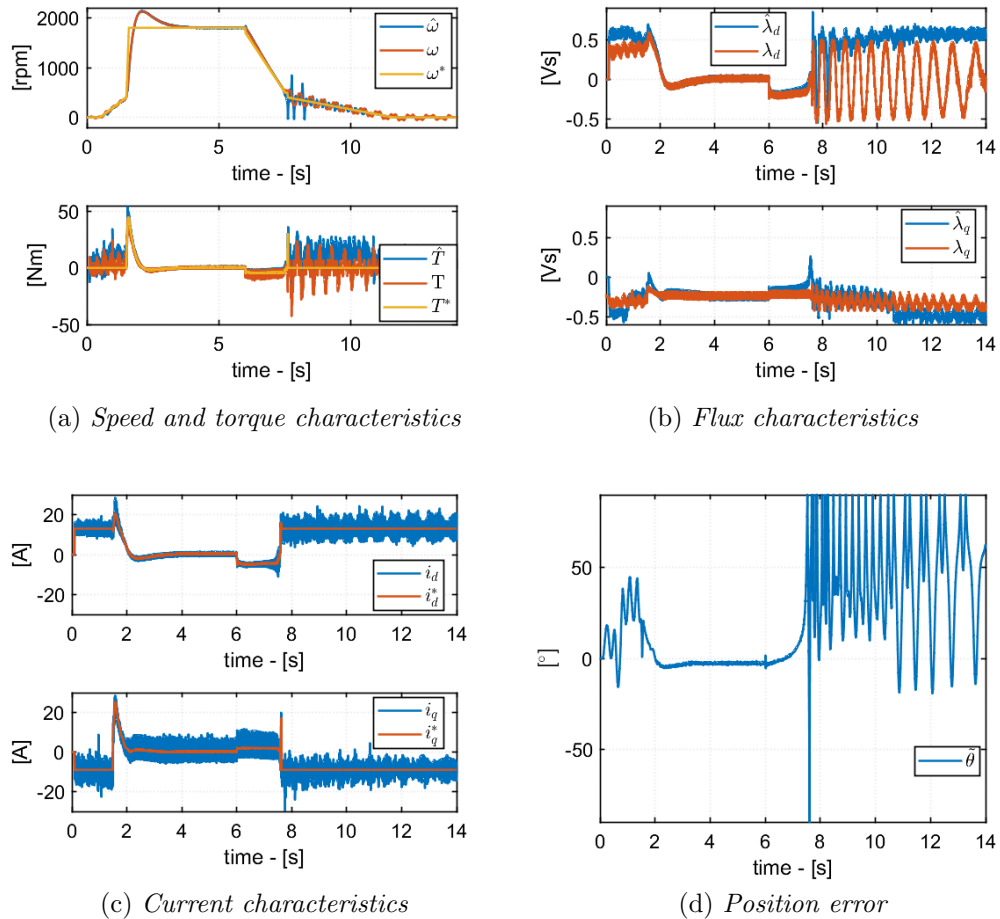


Figure 4.17: Acceleration and deceleration test with no dead-time compensation ($3\mu s$)

In Figure 4.17, inverter dead-time is fixed to $3\mu s$ while the the control code does not compensate it. This time, the results show some problems during the transition in down. However, during sensorless FOC stage, there is no evident difference with compensated dead-time test. This is true only if the motor speed is quite high so dead-time voltage is only a small percentage of the total back-EMF. In fact, dead-time voltage drop can be retrieved as:

$$\Delta V_{d-t} = \frac{4}{3} f_{sw} V_{dc} t_{d-t} \quad (4.13)$$

If $t_{d-t} = 2\mu s$, $\Delta V_{d-t} = 9.6V$, whereas if $t_{d-t} = 3\mu s$, $\Delta V_{d-t} = 14.4V$. At no load rated speed condition, back-EMF is around $82.5V$, therefore in the worst condition illustrated, voltage drop due to dead-time is less than 20%.

In conclusion, it is always better to properly compensate dead-time into implemented algorithm in order to obtain a higher control accuracy.

4.3.4 Nominal load test

The dynamic motor difference between the two aforementioned speed bandwidths is highlighted when the load is imposed or removed. Now, simulation tests are carried out in order to see if the sensorless control strategy is successful also when the motor works with its rated conditions: rated speed 1800 rpm and rated torque 29.8 Nm.

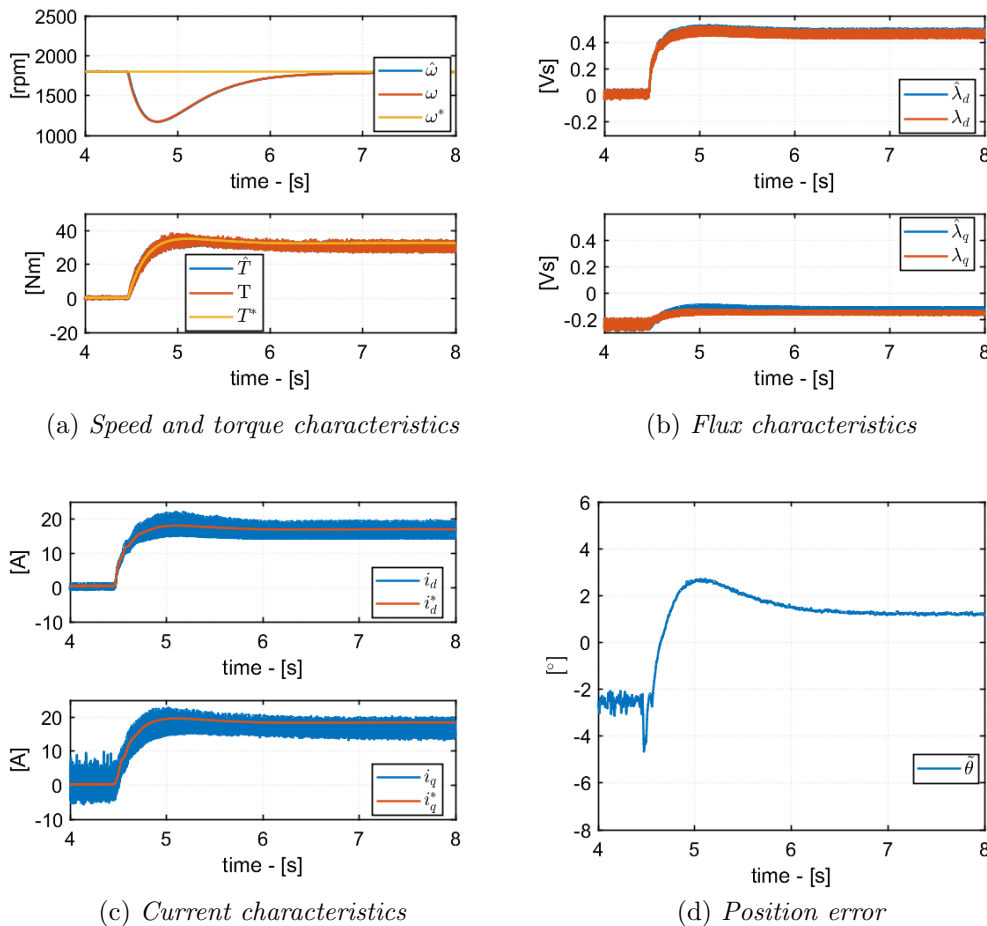


Figure 4.18: Imposing rated torque load with 1.25 Hz speed bandwidth

Figure 4.18 and 4.19 are respectively focused on imposing and removing rated torque load at rated speed, having fixed 1.25 Hz speed bandwidth.

As it can be seen in Figure 4.18, the speed transient is quite slow: when the load is imposed, speed sag is pretty evident, reaching the minimum value of 1200 rpm and returning to the rated speed in 2.5s. The under load position error signal $\hat{\theta}$ is less than the one at no load condition: sensorless control works better with no zero current.

When the torque load is removed, motor speed reaches 2450 rpm, returning to the rated speed in 2.5s. During this transient the absolute value of position error is always less than 8° . Therefore, stability of the proposed sensorless control is verified also under load condition.

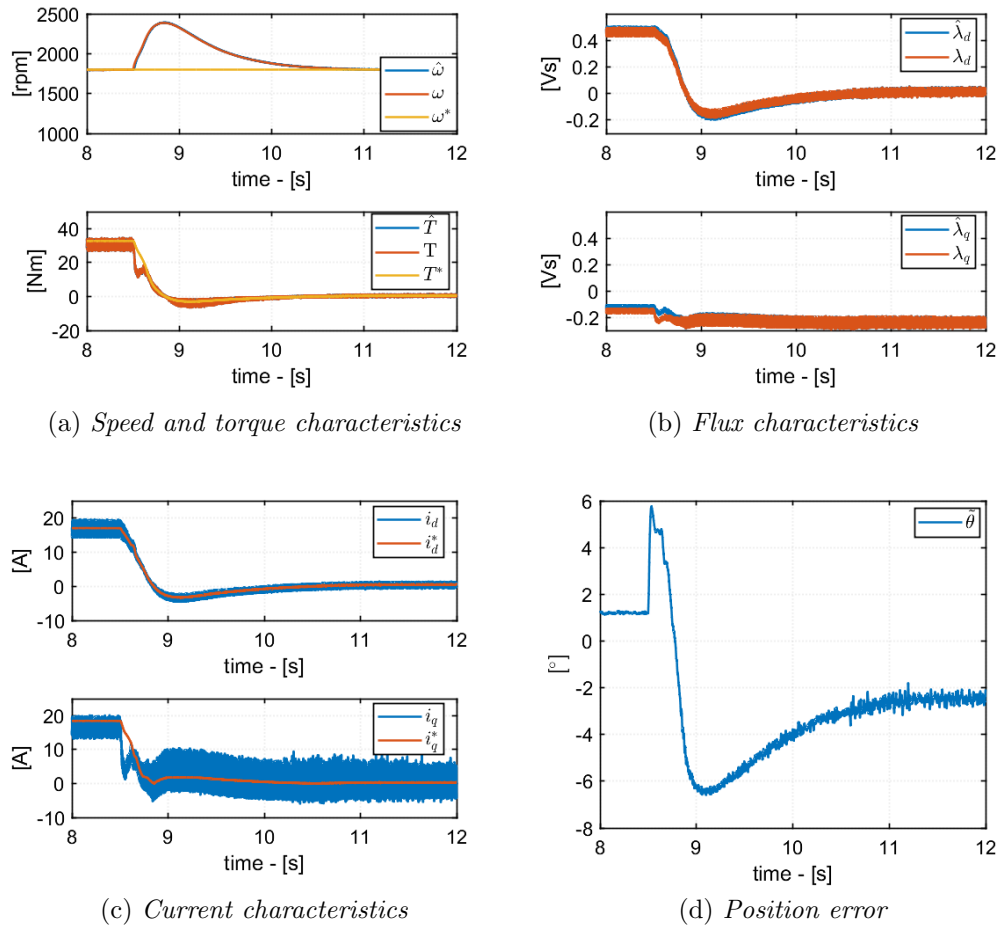


Figure 4.19: Removing rated torque load with 1.25 Hz speed bandwidth

In order to improve speed dynamic, 2.5 Hz speed bandwidth test is carried

out, focusing on imposition and removal of rated torque load (Figure 4.20 and 4.21, respectively).

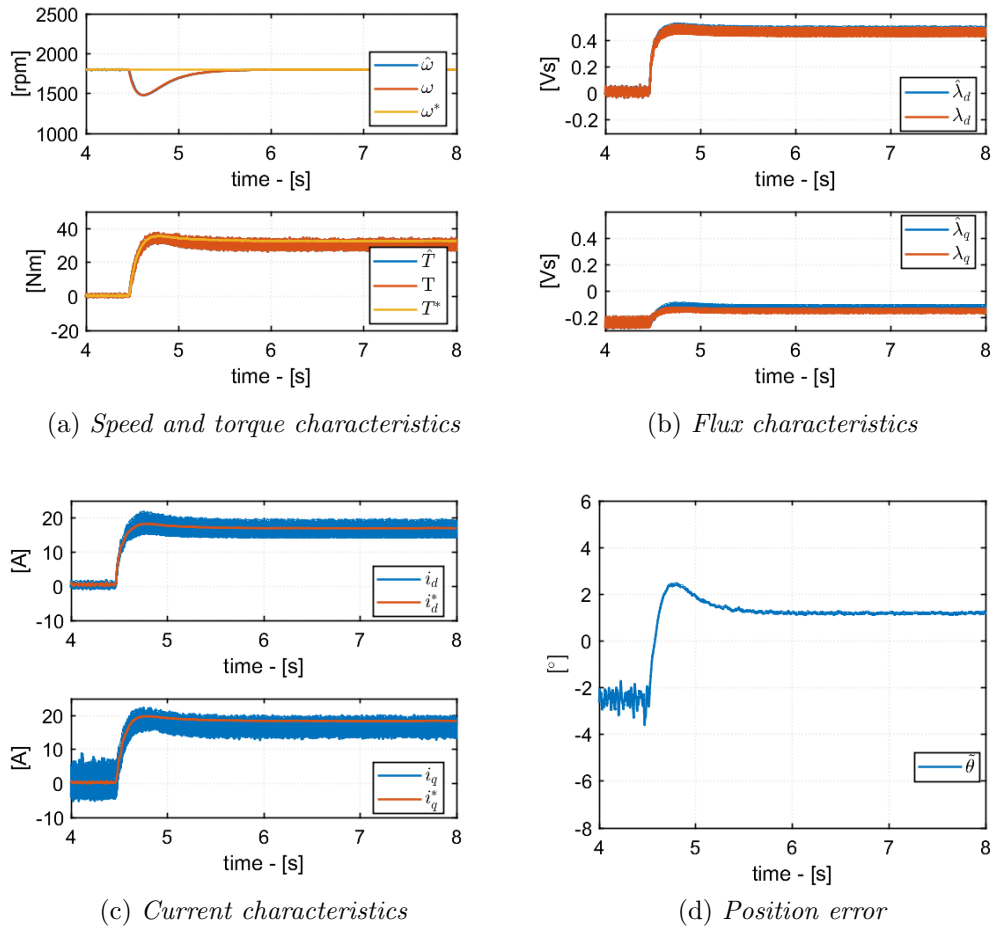
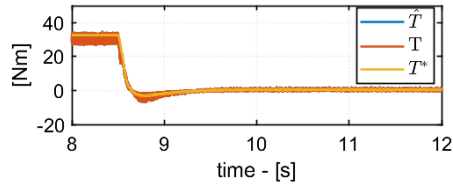
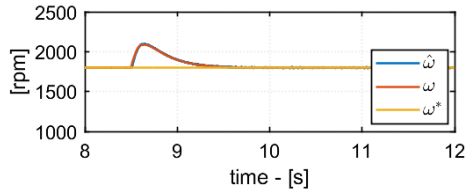


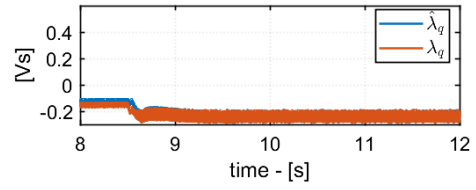
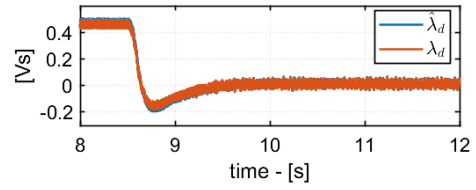
Figure 4.20: Imposing rated torque load with 2.5 Hz speed bandwidth

As it can be seen, these results are better than 1.25 Hz case: speed transient is faster both when the load is imposed and removed, taking only 1.5s. In addition, during transient, speed reaches a minimum value of 1500 rpm and a maximum value of 2100 rpm.

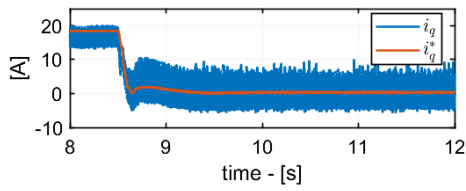
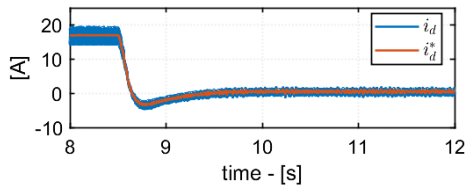
In conclusion, the second speed bandwidth case is preferable in simulink environment because it presents a faster dynamic with no additional noise in all electrical and mechanical motor waveforms.



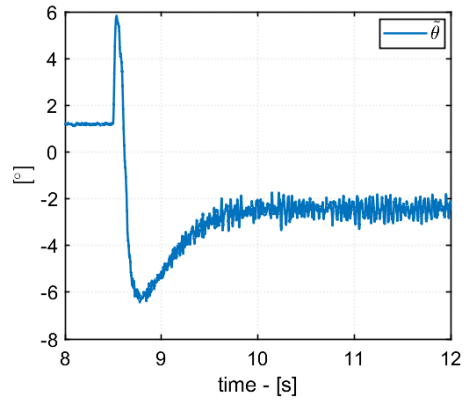
(a) Speed and torque characteristics



(b) Flux characteristics



(c) Current characteristics



(d) Position error

Figure 4.21: Removing rated torque load with 2.5 Hz speed bandwidth

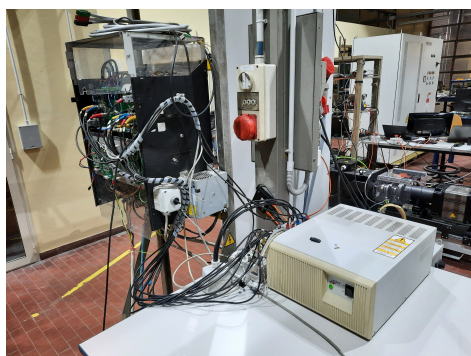
Chapter 5

Experimental results

The purpose of the following chapter is to validate the adopted sensorless control strategy, described in Chapter 3, with experimental tests directly carried out on the test bench. The experimental platform used in this thesis will be briefly described, focusing on both software and hardware components. Besides, experimental results will be presented and discussed in order to understand strengths and weaknesses of flux cross-product position observer this specific test bench, taking into consideration different tuning choices.

5.1 Test bench overview

All experimental tests were carried out at Polytechnic of Turin, in particular the used test bench is located in Enertronica Lab. As shown in Figure 5.1, it is composed by:



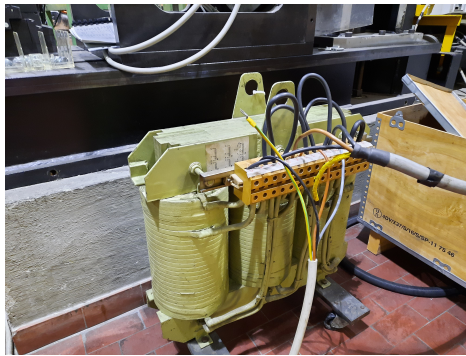
(a) *Inverter - Controller board - DSP*



(b) *Load Inverter - Motor load - ABB motor - PC*

Figure 5.1: Test bench

- **Autotransformer:** the aim of this component is to adapt the output voltage of the Lab transformer in order to obtain the desired dc-link voltage (360V) for the following inverter. Figure 5.2a shows the used autotransformer;
- **Inverter:** it is a three-phase two-level voltage source inverter (VSI). It is composed by three power modules (1200V IGBT), controlled by a PWM 10 kHz switching frequency. This inverter, shown in Figure 5.2b, supplies the ABB motor under test. Besides, it provides, as output, the measured currents and the dc-link voltage signals. On the other hand, it routes the position signal from magnetic encoder to the control platform dSPACE.



(a) Autotransformer



(b) Inverter

Figure 5.2: Autotransformer and custom-made inverter

- **Controller board:** the output signals of the above inverter are connected to a *dSPACE* controller board. It is an High-Speed A/D Board, used for digitizing analog input signals at high sample rates. The 16-bit A/D converters are equipped with differential inputs. As it can be seen from Figure 5.3a, it is made of three components:
 - DS3002 incremental encoder board: it acquires the magnetic encoder signal;
 - CP4002 for Multi purpose digital I/O: inverter analog signals are acquired;
 - DS2004 A/D board: the aforementioned analog input signals are converted into digital ones. Then, they will be provided to DSP.
- **DSP:** The digital signal processor used in this work is produced by *dSPACE* (Figure 5.3b). It elaborates information coming from the

controller board, using $100\mu s$ sampling rate, and exchanges data with the PC: communication is bidirectional.

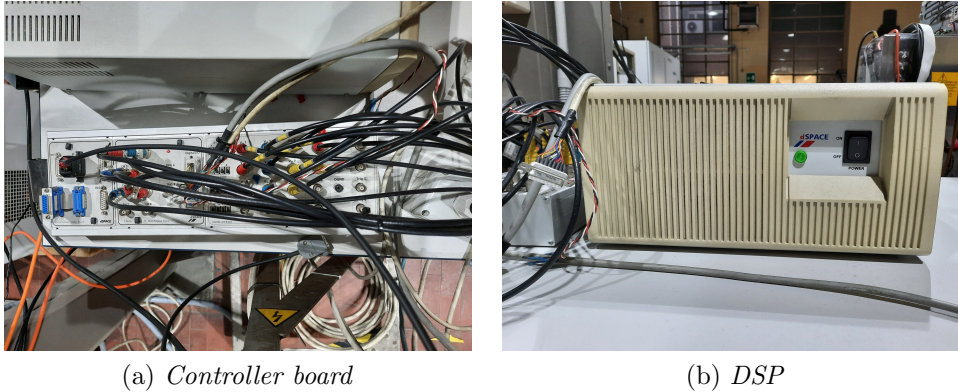


Figure 5.3: dSPACE Controller board and DSP

- **PC:** in order to interface machine drive and human, a PC is used. Two software are operated to real-time control the test bench:
 - **Simulink:** it is a powerful program capable of, among the many features, elaborate information coming from the DSP. In fact, installing the real time interface (RTI) dSPACE library in simulink and creating the desired model, it will be possible to communicate with DSP platform and ControlDesk software. In particular, RTI 1005 has been used in this work. Figure 5.4 shows the used simulink model: it had already been created in the past for other tests on the same ABB machine. *Function-call Subsystem* also contains the same C-algorithm implemented in simulation environment, but with the appropriate changes.

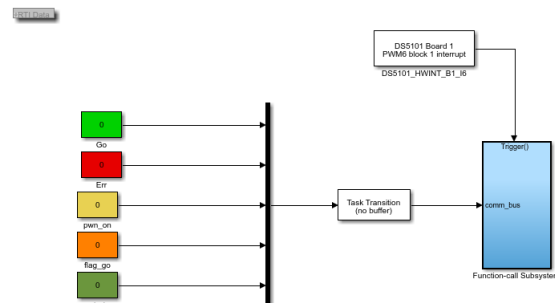
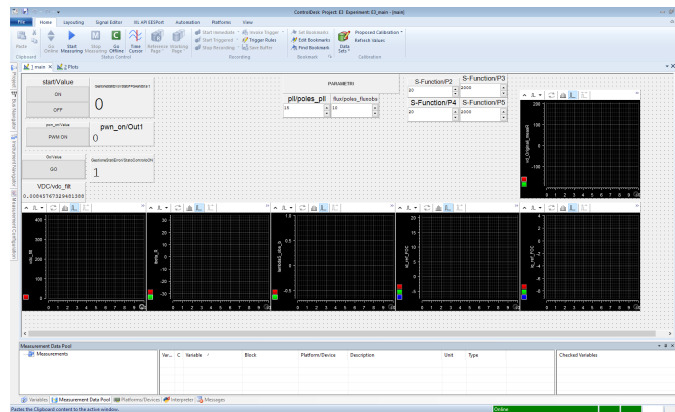
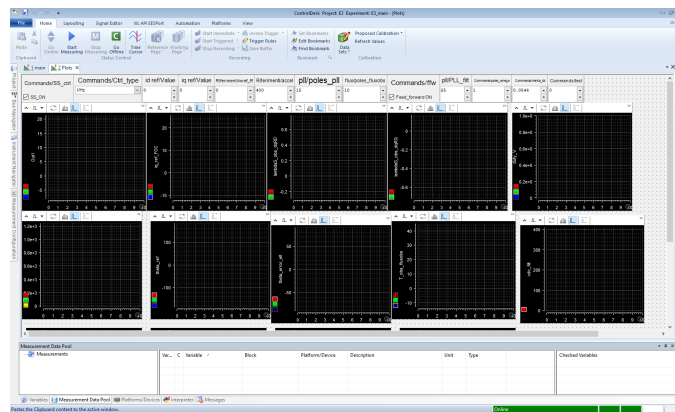


Figure 5.4: RTI-1005 simulink model

- **ControlDesk:** it is the dSPACE experiment software for seamless ECU development. It performs all the necessary tasks in order to real-time control several parameters and desired output characteristics (eg. speed). In addition, it is possible to plot the main waveforms in a single working environment. Figure 5.5 shows the project layout created to properly control the motor's speed and see the measured characteristics or tune parameters, in real-time.



(a) Main layout



(b) Plot layout

Figure 5.5: dSPACE controldesk

- **Machine load:** in order to emulate a variable load, another electric machine (Figure 5.6a) is mechanically connected to the principal one, thanks to a crankshaft coupler. This machine is also manufactured by ABB: it is a synchronous three-phase motor, with 16 kW rated power.
- **Inverter load:** the aforementioned machine is supplied and controlled

by an electronic power converter: ABB Selivector. In addition, a specific software was built ad hoc in order to impose the desired torque or speed command. In this case, ABB Selivector's aim is to torque control this machine in order to test the main ABB motor in different load conditions.

(a) *Inverter*(b) *Load*

Figure 5.6: ABB Selivector: inverter and machine load

- **ABB motor under test:** a detailed description was provided in Chapter 4.

5.2 Summary of the settings

A brief recap of the main parameters and settings used to properly sensorless control the test bench is provided in the following tables. All these data have already been shown in the above subsection 4.2.1, but a summary can be useful in order to understand the next results.

Table 5.1: Experimental platform

Parameter	Value
DC-link voltage	360 V
Switching frequency (f_{sw})	10 kHz
Sampling frequency (f_s)	10 kHz

Table 5.2: I-f control and Sensorless FOC

Parameter	Value
Current k_p	20
Current k_i	2000
$i_{d,ol}^*$	10 A
$i_{q,ol}^*$	-7 A
Speed bandwidth	2.5 Hz
Acceleration slew-rate	see 4.2.1
ω_{up}	400 rpm
ω_{down}	300 rpm

Table 5.3: Flux observer and PLL

Parameter	Value
g	$2\pi 10$ rad/s
ω_{act}	100 rpm
PLL position poles	$2\pi 15$ rad/s
Speed frequency cut-off	25 Hz

5.3 Experimental results

Once all parameters are fixed, the following tests will be shown in the next subsections:

- Acceleration and deceleration test at no load;
- Acceleration and deceleration test under load;
- Nominal load test;
- Overload test;
- Harmonics analysis.

In order to understand the behaviour of the adopted sensorless control before described test bench, the main useful waveforms we are focusing on are:

- Mechanical speed and torque: reference speed ω^* , measured speed ω , estimated speed $\hat{\omega}$, reference torque T^* (PI speed controller output) and estimated torque \hat{T} ;
- Flux linkage: observed flux $\hat{\lambda}_{dq}$ and estimated flux $\hat{\lambda}_{dq}^i$ (LUT flux maps output);
- Current: measured current i_{dq} and reference current i_{dq}^*
- Error: PLL input ϵ and error angle $\tilde{\theta}$;
- Voltage: measured motor voltage v_{dq} and dc-link voltage v_{dc} ;
- Duty cycles d_{uvw} .

All these characteristics are expressed in time domain. However, when discussing the harmonics analysis, an $xy - plot$ will be used to understand behaviour of α, β measured and reference current and observed flux.

5.3.1 Acceleration and deceleration test at no load

The aim of this subsection is to test the reliability of the adopted sensorless control during start and stop, without any torque load. The used slew-rate acceleration is the one described in 4.2.1: it is the best choice but only for this configuration, that is with this load and inertia.

As far as concern the down transition strategy, a fundamental precaution is the imposition of reference current allocated into zero torque locus during I-f control: as it can be seen from Figure 4.8, $i_{d,ol}^* = 10A$ and $i_{q,ol}^* = -7A$ is a valid choice, providing only a half of the rated motor current. In order to validate the precaution adopted, there will be carried out a test where the reference current during open-loop control is fixed along d -axis.

Besides, also 1.25 Hz speed bandwidth test will be presented to highlight advantages and drawbacks of 2.5 Hz case.

Acceleration at no load

Figure 5.7 shows acceleration and deceleration test at 1800 rpm with no load, using reference current into zero torque locus during I-f control.

As it can be seen, control strategy is successful in these conditions: estimated speed, as well as measured one, is quite smooth during transitions and it does not present spikes. During steady state, estimated speed noise oscillates between 1750 rpm and 1850 rpm while the measured one can be considered trivial: ABB motor did not emit any strange acoustic noise.

Moreover, all other electrical waveforms present visible noise at no load steady state condition. The cause of this "problem" lies on high speed bandwidth: it amplifies the noise also caused by used average flux maps, which does not consider harmonics contribution of the real motor. Therefore, $\tilde{\theta}$ oscillates and it induces noise in other characteristics, for example flux linkage, motor voltage and current.

Besides, it has already been illustrated that sensorless controls do not work well near no load condition. In fact, signal noise ratio (SNR) of flux and position error is lower in this condition: in particular, it is proportional to the load.

However, the control strategy is stable and robust: error angle does not exceed $\pm 10^\circ$ during sensorless FOC.

Non-zero torque locus I-f reference

If reference current vector is located in d-axis during I-f control (Figure 5.8), the only difference with respect to the above test is found during the downwards transition: imposing 13A only on d-axis leads to a torque ripple, as it can be deduced from Figure 4.8. Therefore, estimated speed has a spike while the measured one oscillates around the desired speed. During the aforementioned transient, all the other shown characteristics are not as smooth as before but nevertheless the convergence is not lost. However, if the torque map is known, it is always preferable to impose a reference current vector on zero torque locus.

Bandwidth analysis

In order to reduce the noise amount showed in the before tests, speed bandwidth can be decreased to 1.25 Hz. Figures 5.9 and 5.10 are the same tests showed respectively in Figure 5.7 and 5.8, but with a lower speed dynamic.

As announced before, the main benefit is the noise reduction in all illustrated waveforms, at no load steady state condition. However, due to the low speed loop dynamic, deceleration slew-rate during sensorless FOC must be reduced to 500 rpm/s: on this way, reference and estimated speed will be equal when the transition occurs and thus the precaution described in subsection 3.4.2 is satisfied.

As explained in Chapter 4, the lower the speed bandwidth, the higher is the speed overshoot when there is a "step" reference speed. In experimental test, the real motor speed reaches a peak of 2100 rpm if the speed-loop dynamic is fixed to 1.25 Hz.

Same considerations retrieved for Figure 5.8 can be done for Figure 5.10, where only d reference current component is imposed during I-f control. The most important deduction is control strategy does not diverge also in this situation.

For completeness, Figure 5.11 shows the case in which the deceleration slew-rate is maintained to 800 rpm/s, although speed bandwidth is too low (1.25 Hz). As a consequence the control is too slow with respect to the reference speed and so not all precautions for transition in down are respected. Therefore, after the transition to I-f, the estimated speed starts to oscillate around reference speed while the real motor speed lags behind. Acoustic noise can be heard during this phase.

Figures

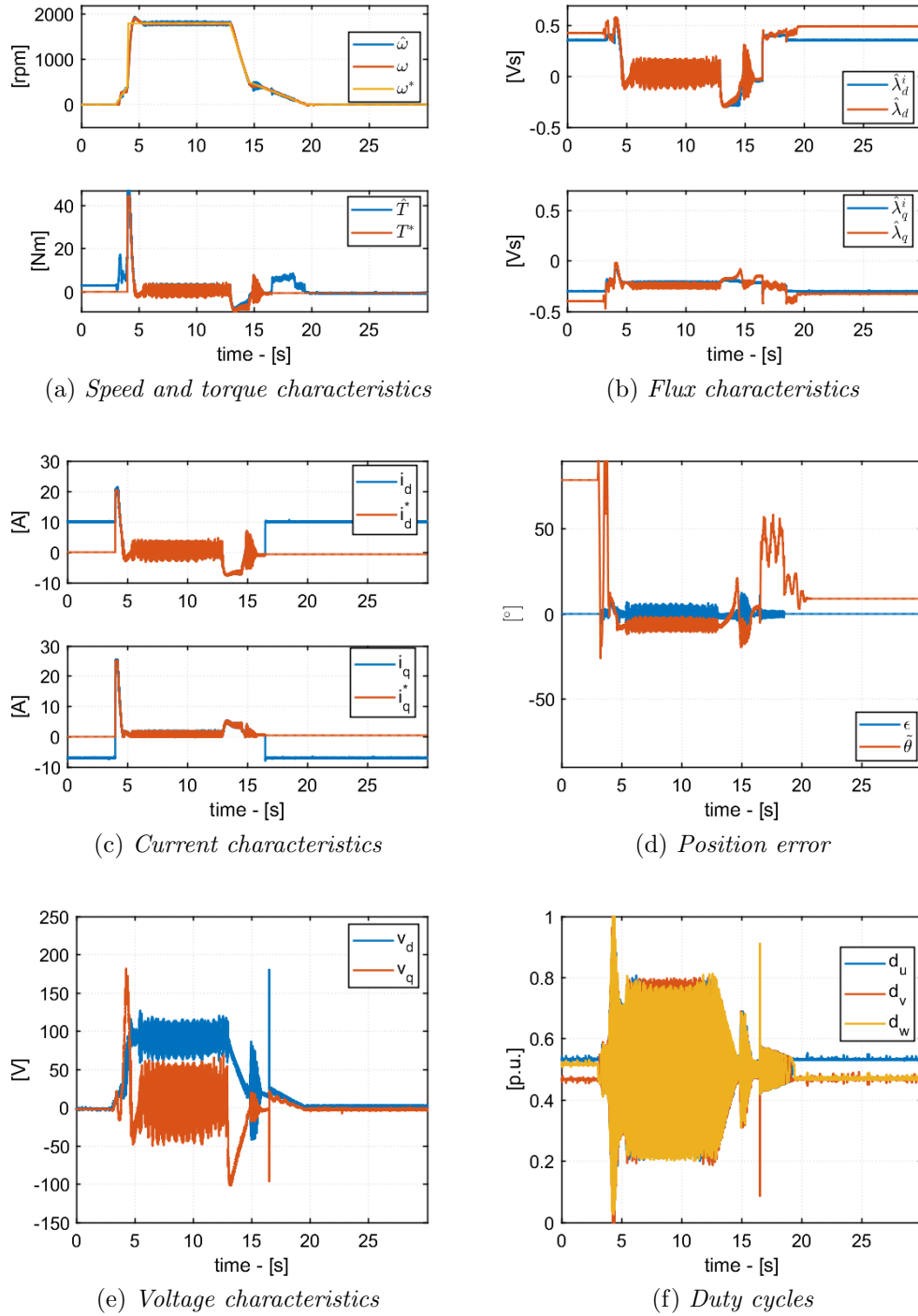


Figure 5.7: Acceleration and deceleration test at no load

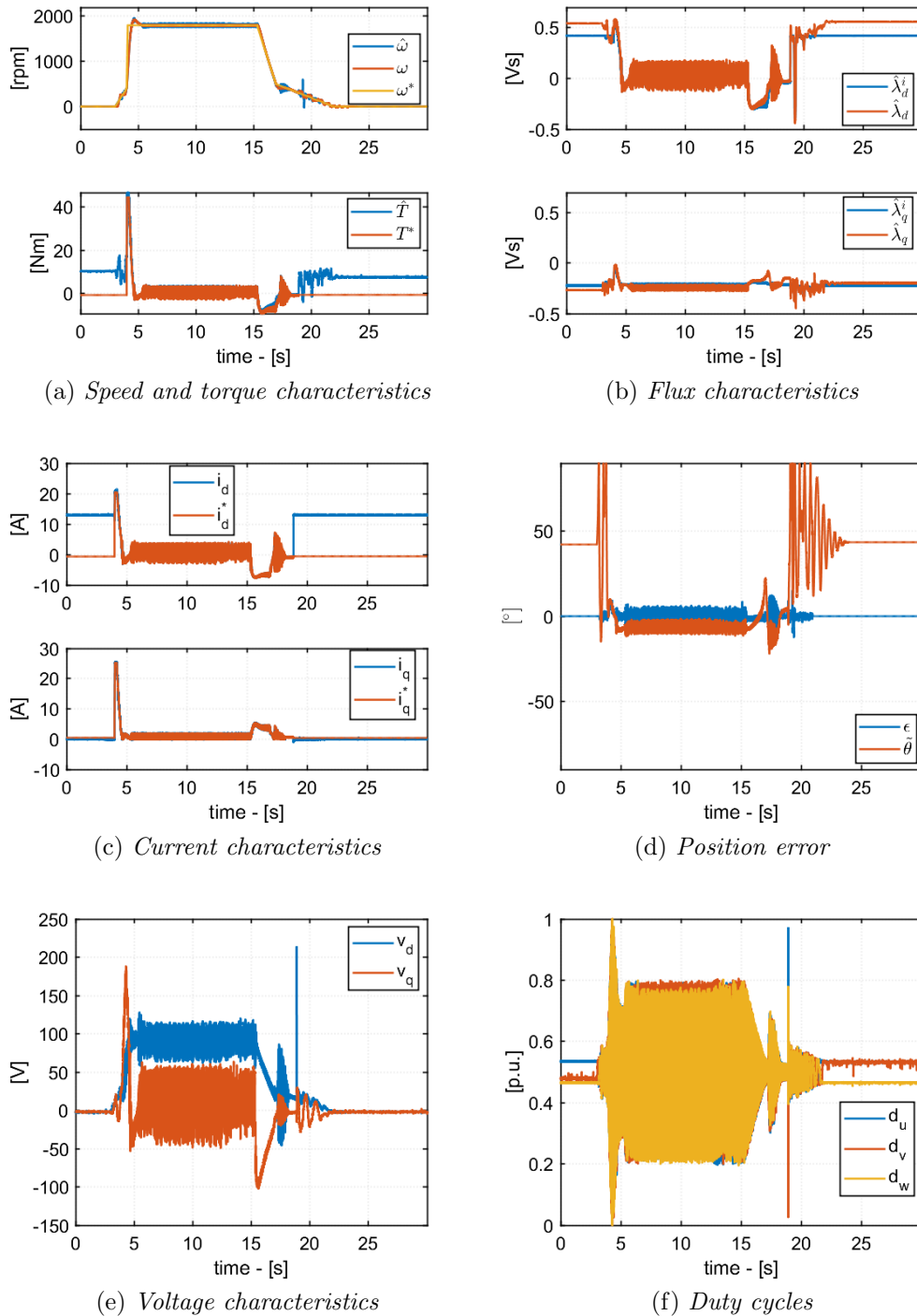


Figure 5.8: Acceleration and deceleration test at no load, using a reference current vector located on d-axis during I-f control

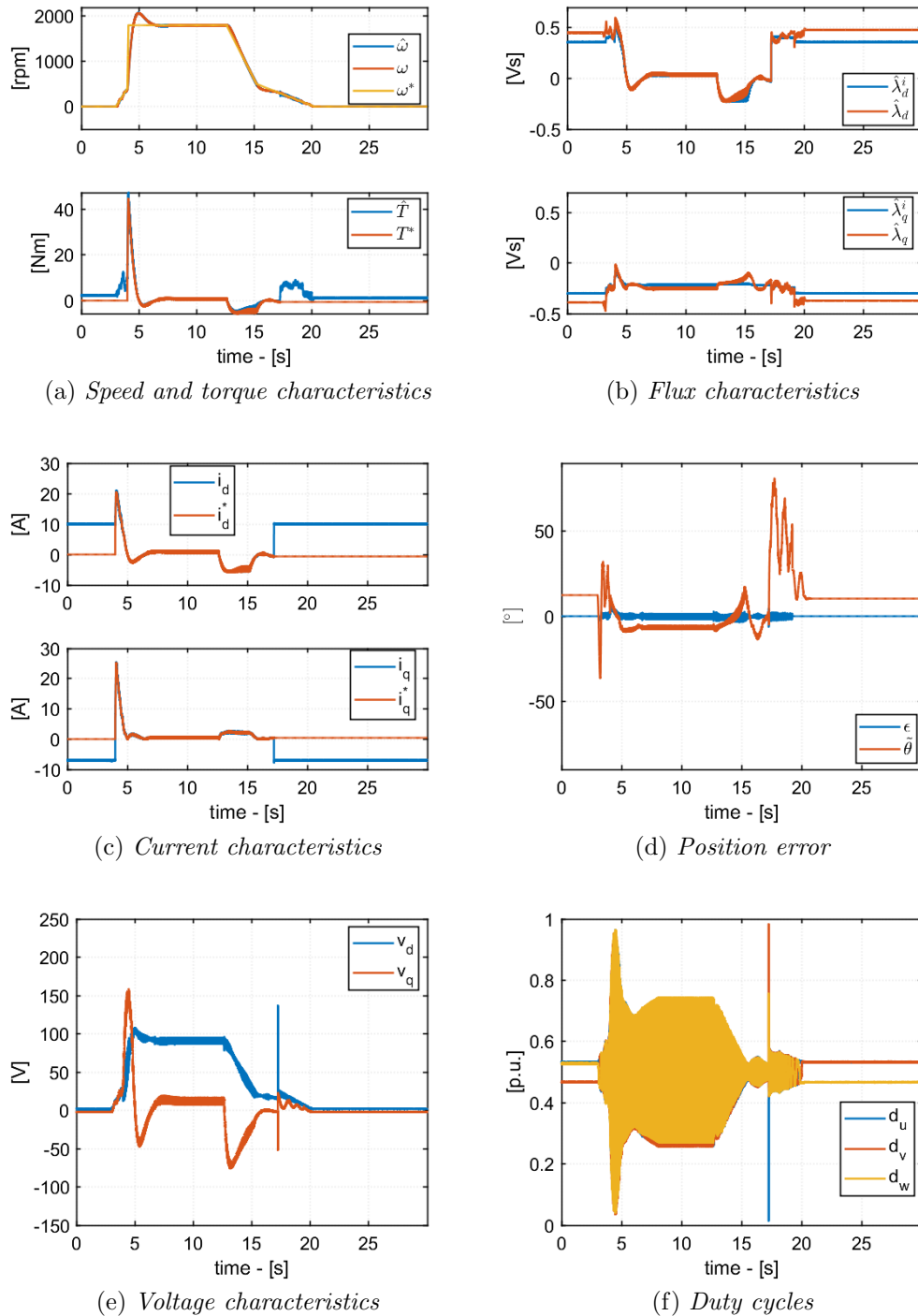


Figure 5.9: Acceleration and deceleration test, using 1.25 Hz speed bandwidth

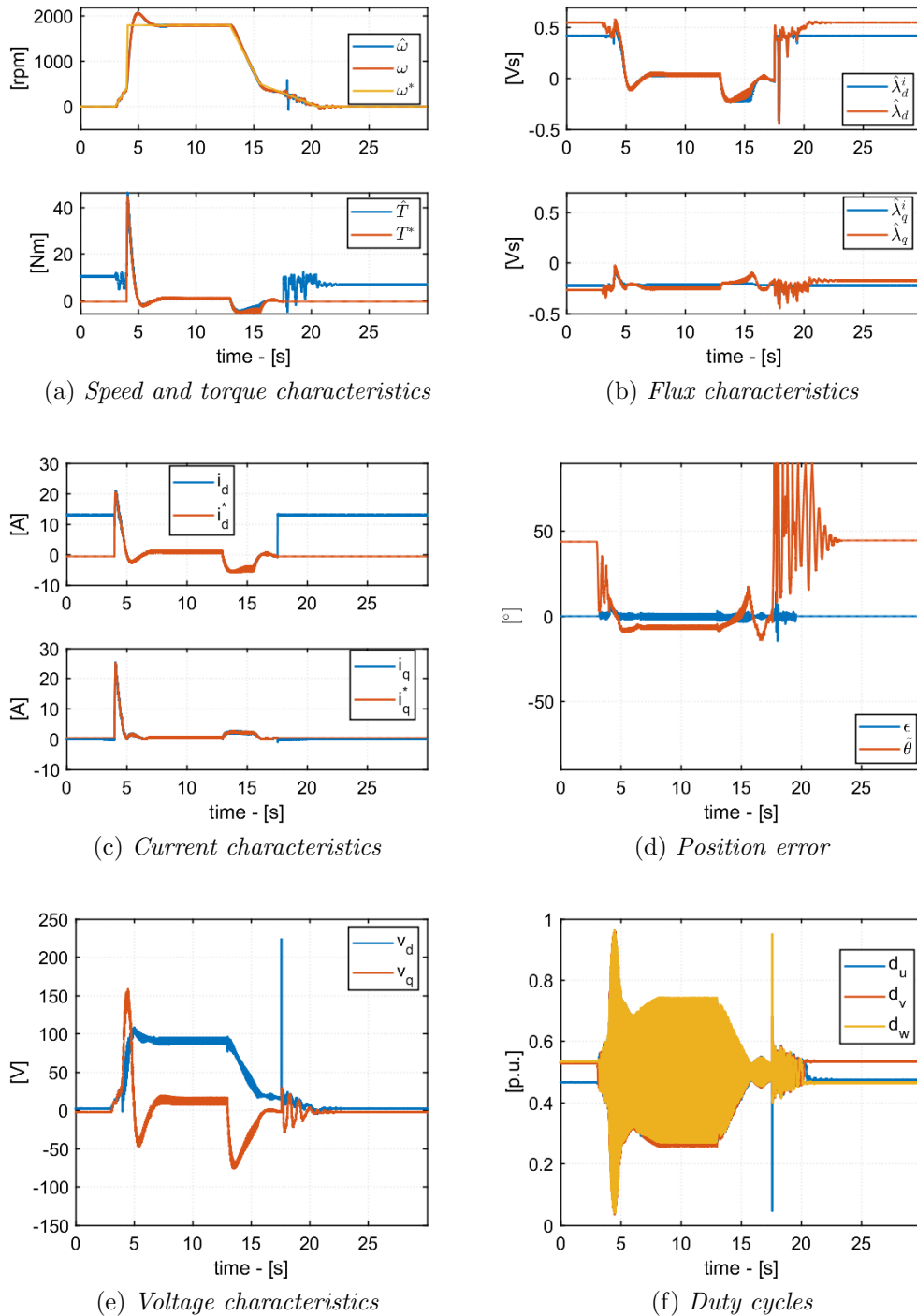


Figure 5.10: Acceleration and deceleration test at no load with 1.25 Hz speed bandwidth, using a reference current vector located on d-axis during I-f control

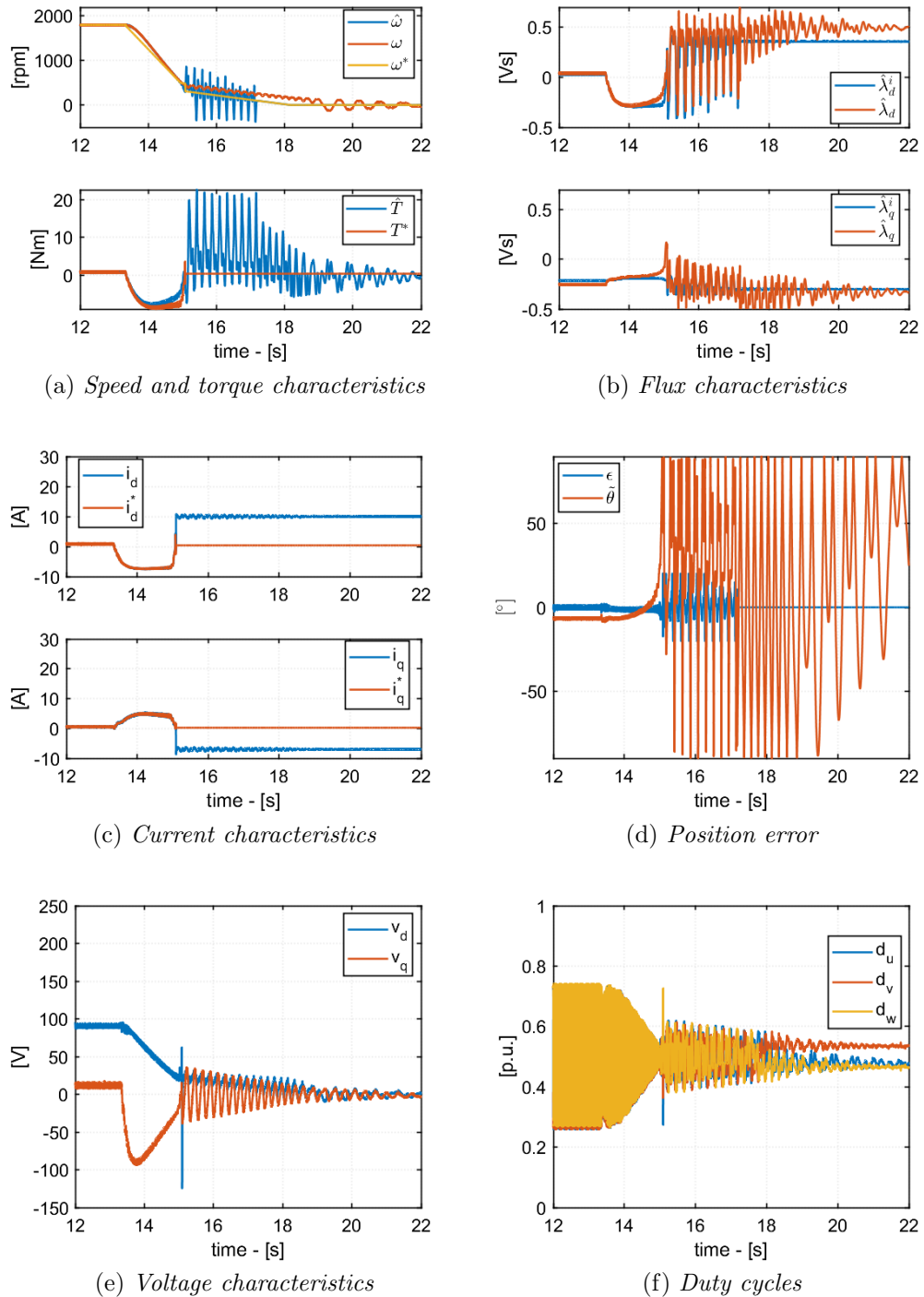


Figure 5.11: Focus on deceleration test at no load with 1.2 5Hz speed bandwidth, using a 800 rpm/s deceleration slew-rate

In conclusion, as far as acceleration and deceleration test at no load in industrial environment are concerned, the best solution is obtained adopting a higher speed bandwidth (2.5 Hz) and using zero torque locus reference current during I-f control.

5.3.2 Acceleration and deceleration test under load

As known from literature, I-f control does not lend itself well to carrying load due to the few degrees of freedom. Nevertheless, we wanted to test the load bearing capacity in the electric motor start and stop phase.

Using the configuration described in section 5.2, three acceleration and deceleration tests are carried out, adopting three different torque loads and imposing a speed reference to half rated speed (900 rpm).

In the first test, showed in Figure 5.12, 15% of the rated torque is required. During I-f control, the current vector amplitude is fixed $12.2A_{pk}$, almost a half of the rated one. As it can be seen, the chosen current is enough to bear the imposed 4.5 Nm torque load. During all the phases, estimated and measured speed are quite smooth, ensuring control convergence.

In the second test, showed in Figure 5.13, torque load is imposed to the 27.5% of the rated one. Once again, the chosen $12.2A_{pk}$ amplitude current can bear the imposed 8.2 Nm torque load. Despite the real motor speed oscillates a little bit during I-f control deceleration, convergence is not lost, so the control strategy can be considered successful also in this condition.

In the last test, showed in Figure 5.14, the imposed torque load is the 40.2% of the rated one. This time, $12.2A_{pk}$ amplitude current vector during I-f control is not sufficient, therefore it is chosen $i_d = 13A$ and $i_q = -9A$, reaching an amplitude of $15.8A_{pk}$.

As it can be seen, the only critical situation is during deceleration, in particular when the control strategy jump to I-f control. In fact, the open loop speed control cannot guarantee a high speed accuracy, so the measured speed oscillates around the desired value. However, control strategy ensures convergence also this time.

As far as speed noise at steady state condition is concerned, it is strongly reduced with respect to no load case due to non zero current components during sensorless FOC, thanks to the imposed torque load. This aspect will be analysed in the next subsection.

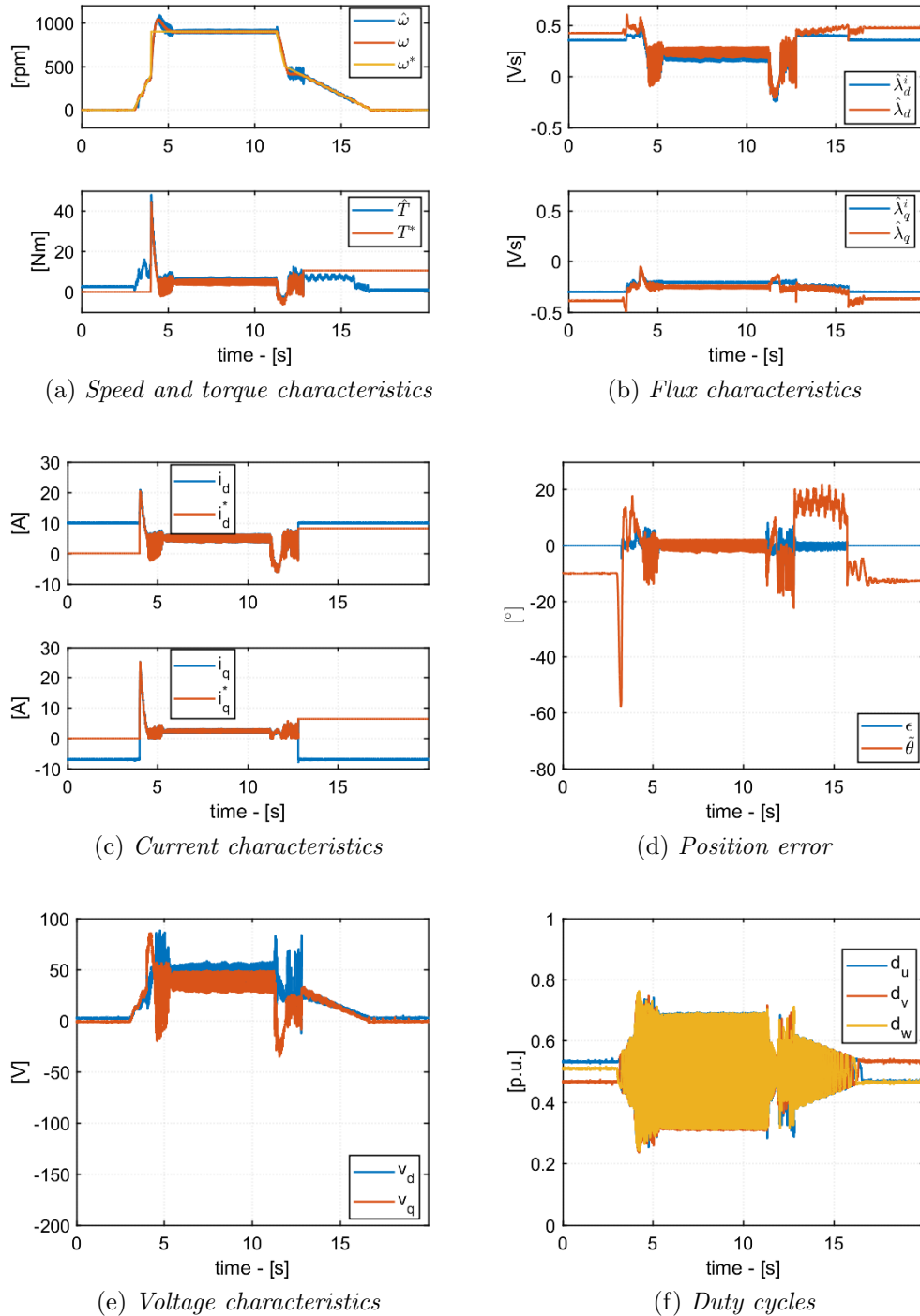
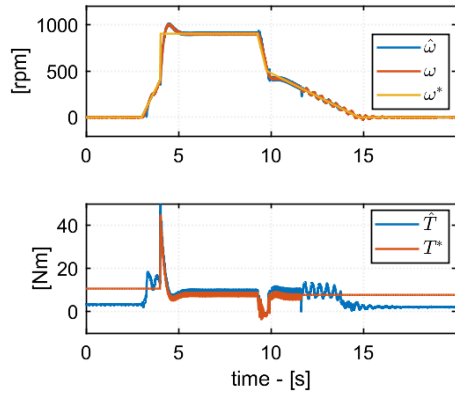
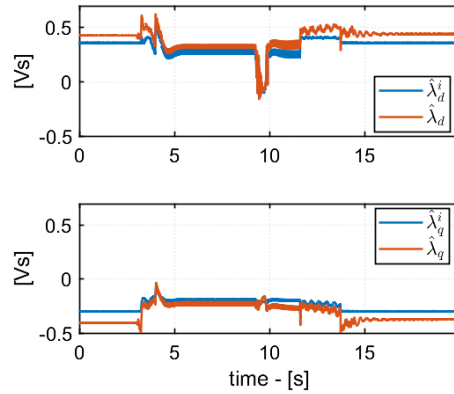


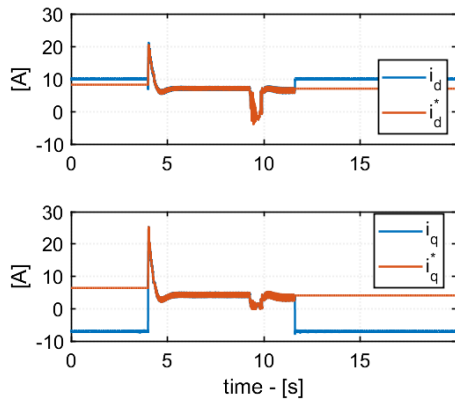
Figure 5.12: Acceleration and deceleration test at 900 rpm with 15% of rated torque load



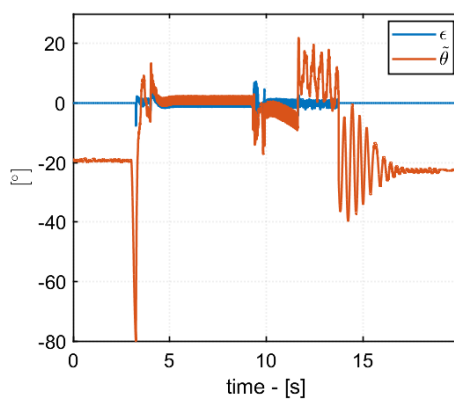
(a) Speed and torque characteristics



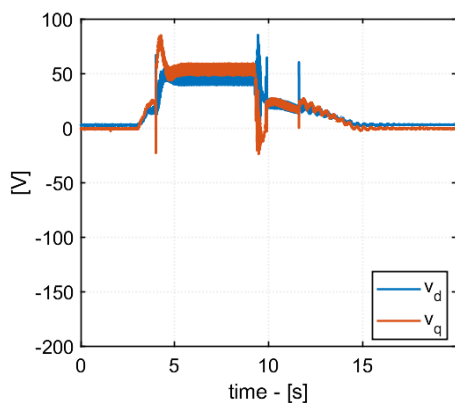
(b) Flux characteristics



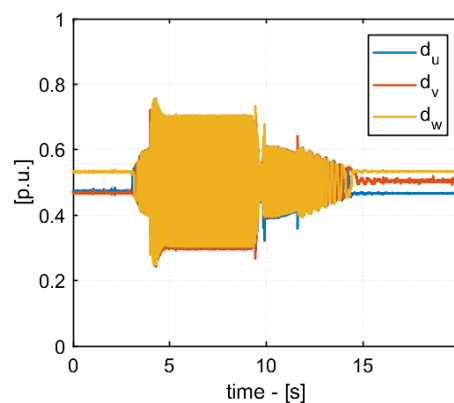
(c) Current characteristics



(d) Position error



(e) Voltage characteristics



(f) Duty cycles

Figure 5.13: Acceleration and deceleration test at 900 rpm with 27.5% of rated torque load

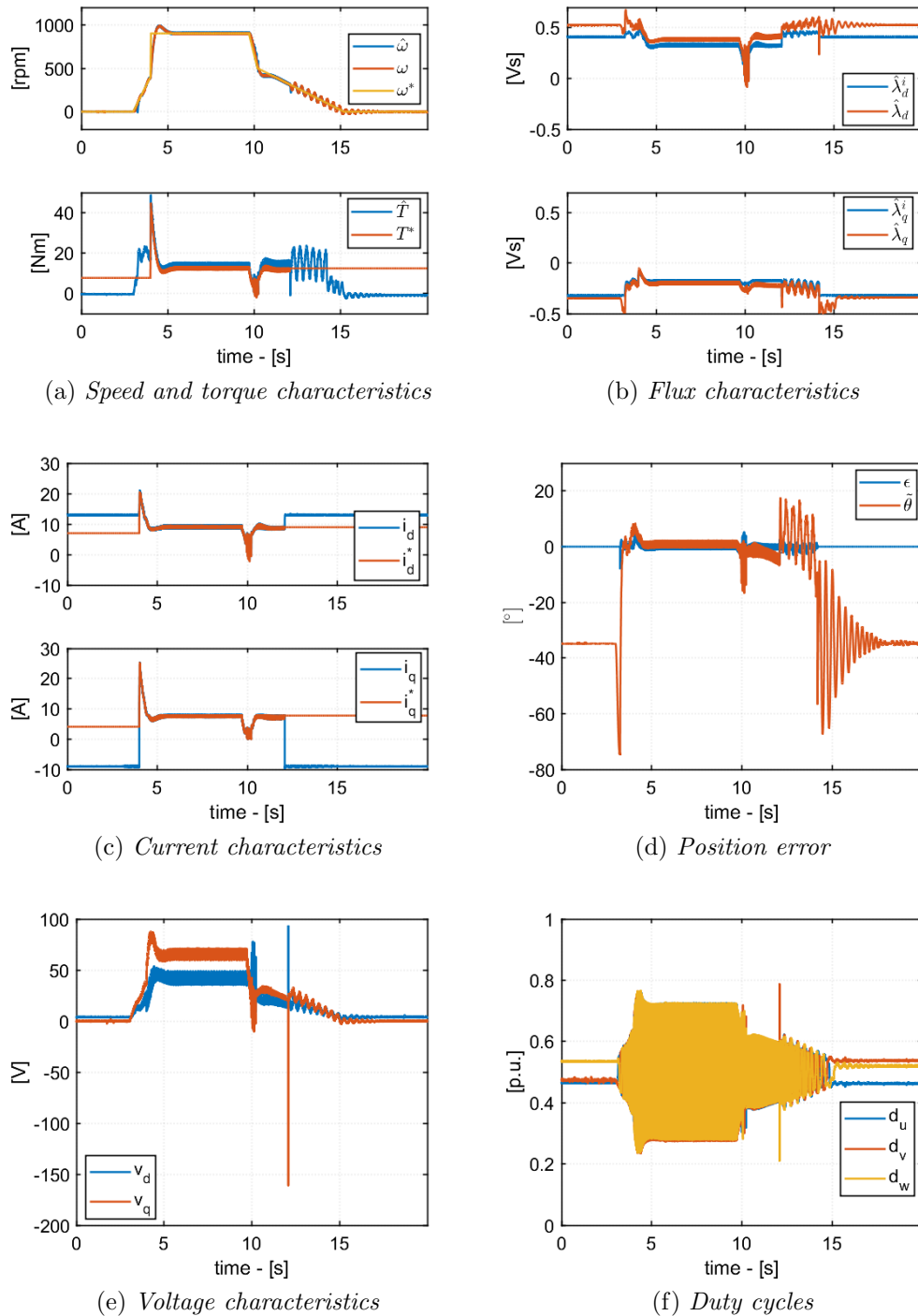


Figure 5.14: Acceleration and deceleration test at 900 rpm with 40.2% of rated torque load

5.3.3 Nominal load test

Once acceleration and deceleration tests at no load and reduce load are carried out, it is time to test ABB motor under its rated conditions: 1800 rpm and 29.8 Nm.

Figure 5.15 and 5.16 highlight respectively imposition and removal of the rated torque when the motor is rotating at its nominal speed.

The first thing that can be noticed is the reduction of estimated speed noise when the rated torque is imposed: this is the umpteenth confirmation of the best performance of a sensorless control when the motor current is not zero.

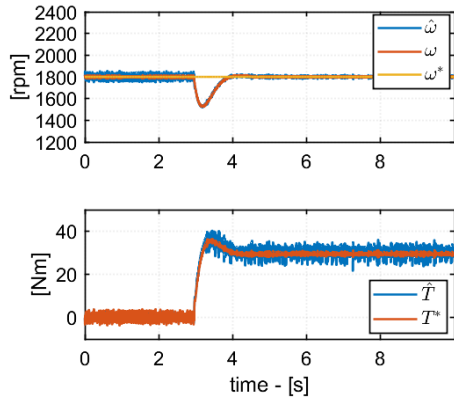
As soon as torque load is imposed, current components go to the values provided by MTPA LUT. However, the measured ones seem a little bit shaky. Looking at duty cycle characteristics, they reach maximum value. Therefore the origin of this problem lies in the voltage supply: dc-link voltage changes according to machine operating point because it depends from the absorbed power: the higher power is absorbed, the higher voltage drop in supply is obtained. In fact, we are using a weak grid supply which cannot guarantee a constant dc-link voltage. As showed in Figure 5.15g, supply voltage falls down to 333V. Two possible solutions could be used: increase dc-link voltage, operating to the autotransformer number of turns or directly use a stronger voltage supply.

Nevertheless, the adopted sensorless control strategy properly works when the rated torque is imposed. In fact, error angle $\tilde{\theta}$ oscillates around zero, not exceeding $\pm 5^\circ$.

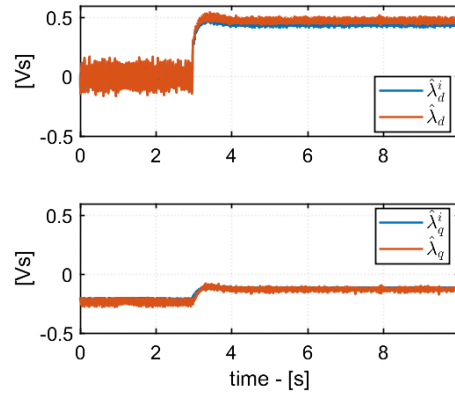
As discussed in the above subsection, it is evident that sensorless FOC works better when a torque load is imposed. In fact, in this case, current and flux magnitudes are not trivial, thus SNR of these quantities increase, bringing benefits to the control, such as reduction of noise in the shown waveforms. Once the rated load is removed (Figure 5.16), the shown waveforms increase their noise, while dc-link voltage returns to 360V.

What happen if speed bandwidth is reduced to 1.25Hz? Imposition and removal of rated torque (respectively Figure 5.17 and 5.18) do not cause any significant problem: during imposition, the motor speed sag reaches 1250 rpm with a settling time of 2s, while during removal, the speed overshoot achieves 2400 rpm.

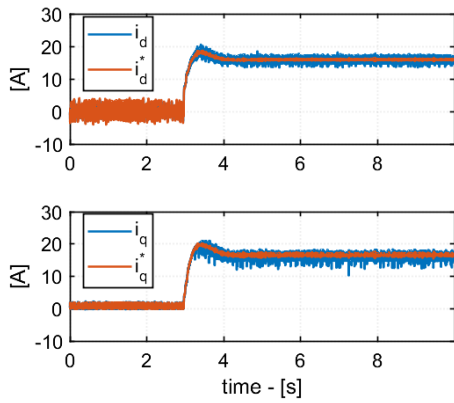
However, in order to obtain a better speed dynamic, it is recommended to impose a speed bandwidth equal to 2.5 Hz.



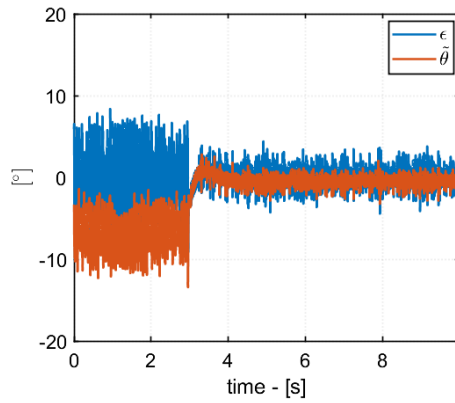
(a) Speed and torque characteristics



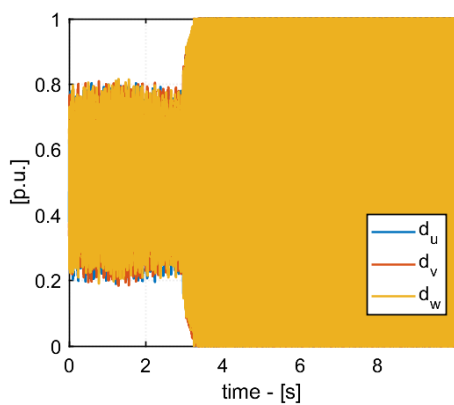
(b) Flux characteristics



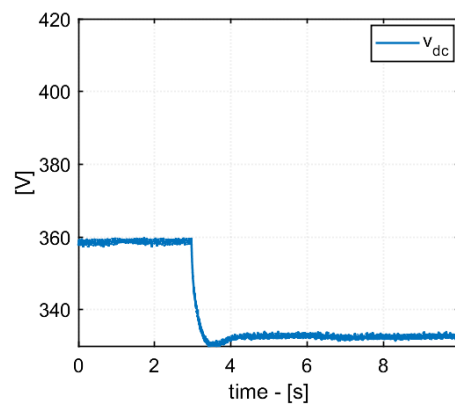
(c) Current characteristics



(d) Position error

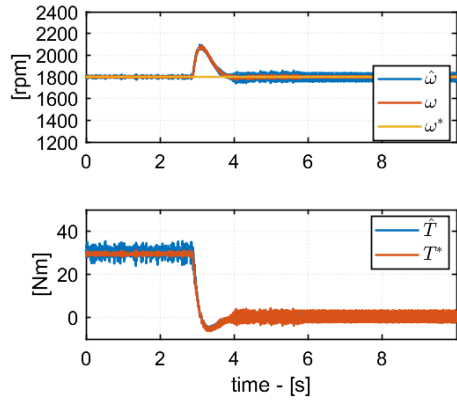


(e) Duty cycles

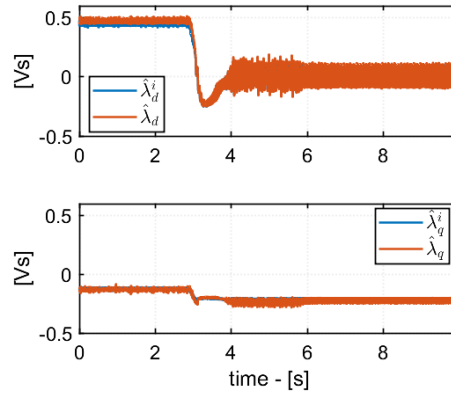


(f) DC-link voltage

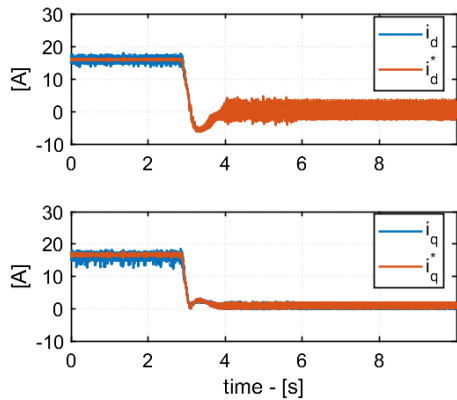
Figure 5.15: Rated torque load imposition at rated speed



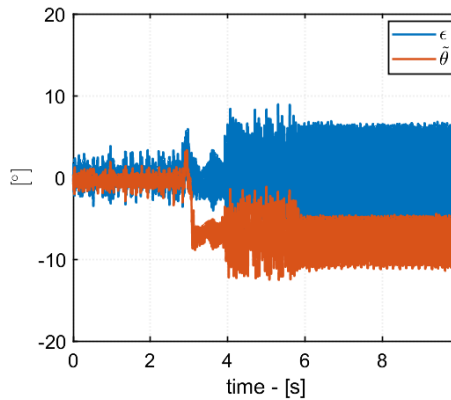
(a) Speed and torque characteristics



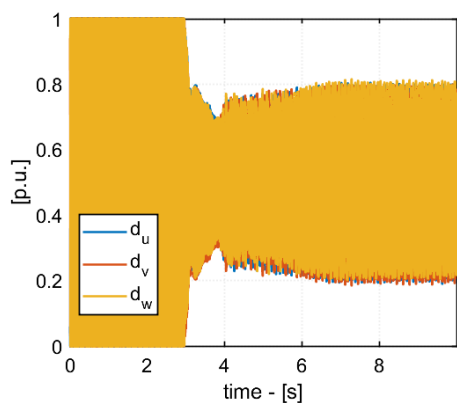
(b) Flux characteristics



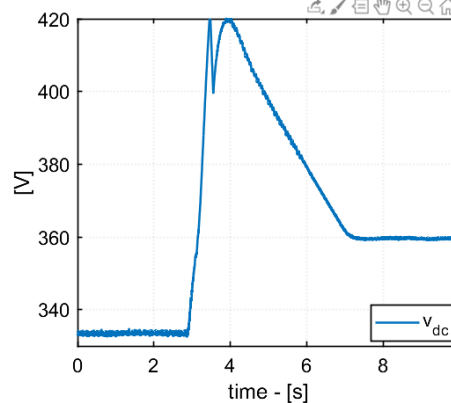
(c) Current characteristics



(d) Position error



(e) Duty cycles



(f) DC-link voltage

Figure 5.16: Rated torque load removal at rated speed

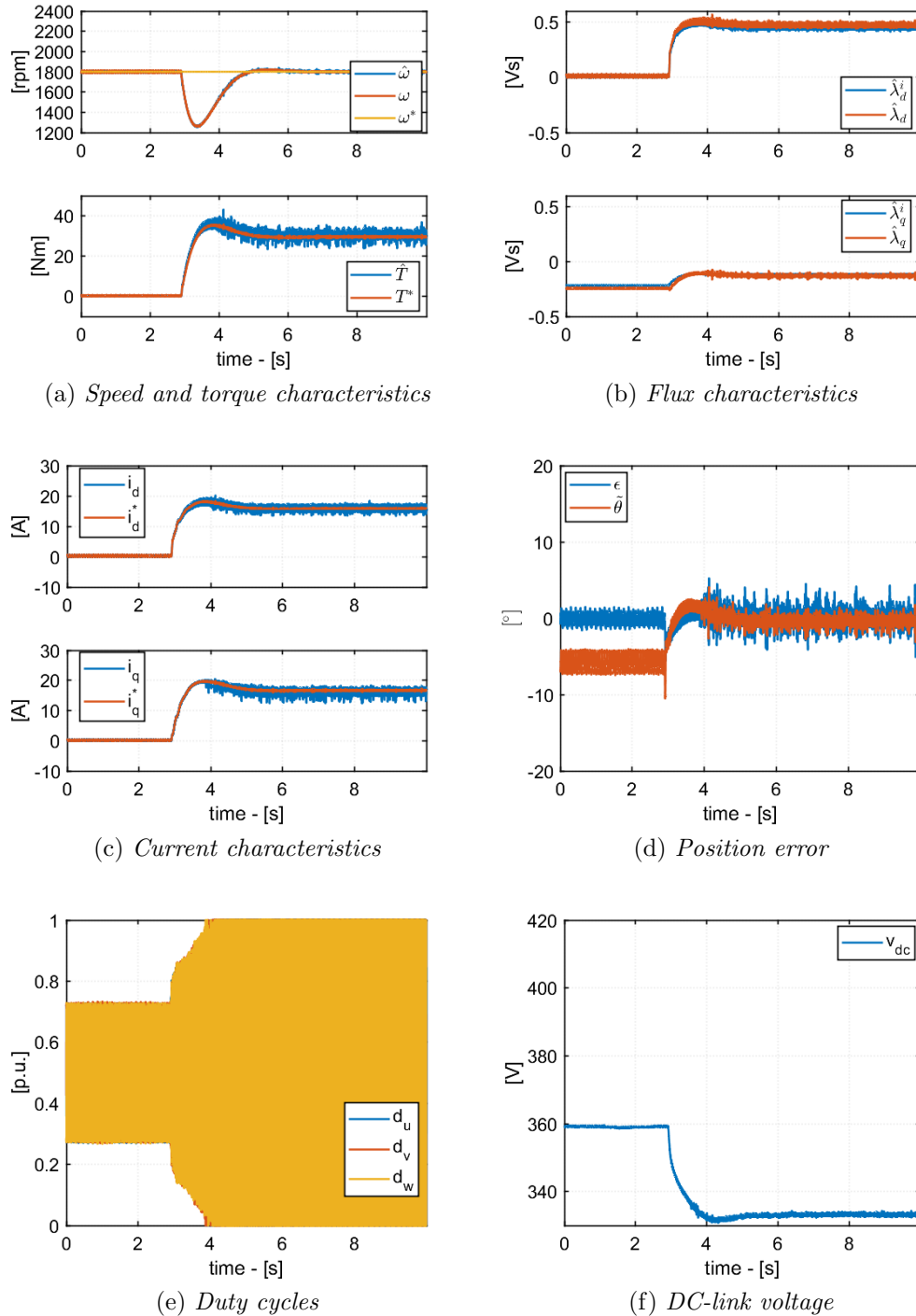
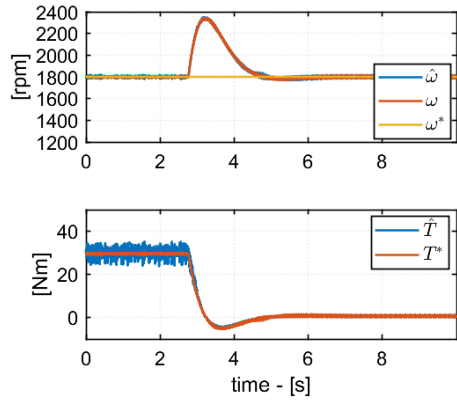
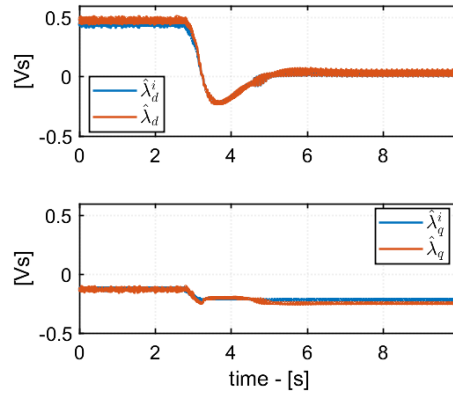


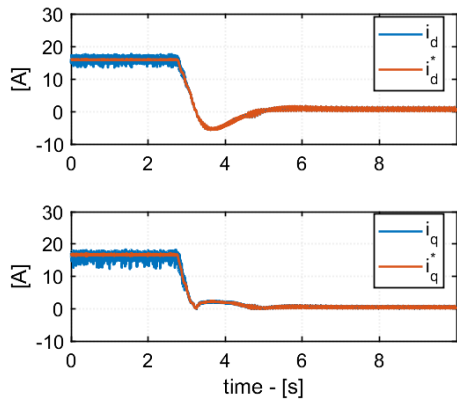
Figure 5.17: Rated torque load imposition at rated speed, using 1.25 Hz speed bandwidth



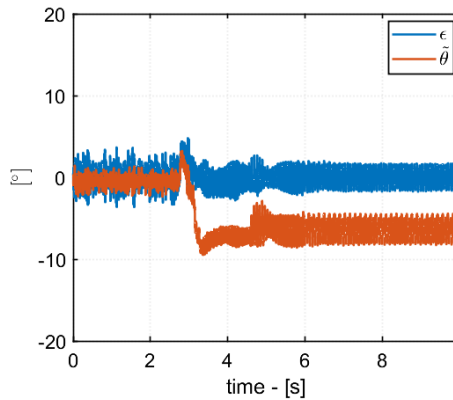
(a) Speed and torque characteristics



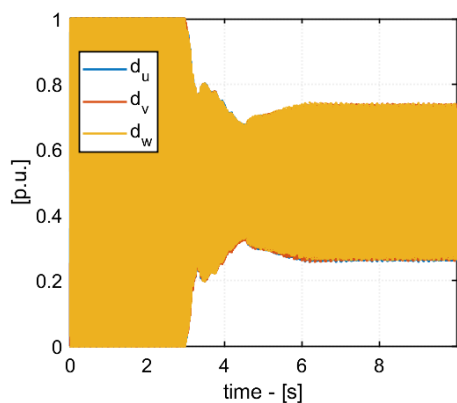
(b) Flux characteristics



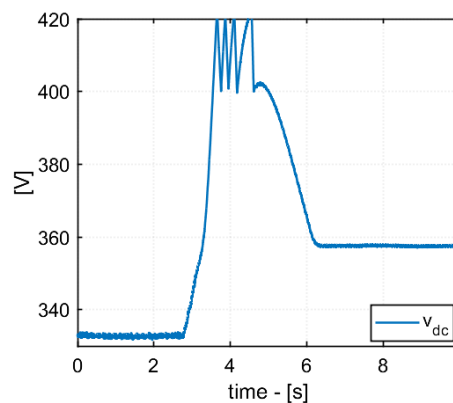
(c) Current characteristics



(d) Position error



(e) Duty cycles



(f) DC-link voltage

Figure 5.18: Rated torque load removal at rated speed, using 1.25 Hz speed bandwidth

Nominal load test at 80% of rated speed

All the tests before presented are again carried out at 80% of rated speed.

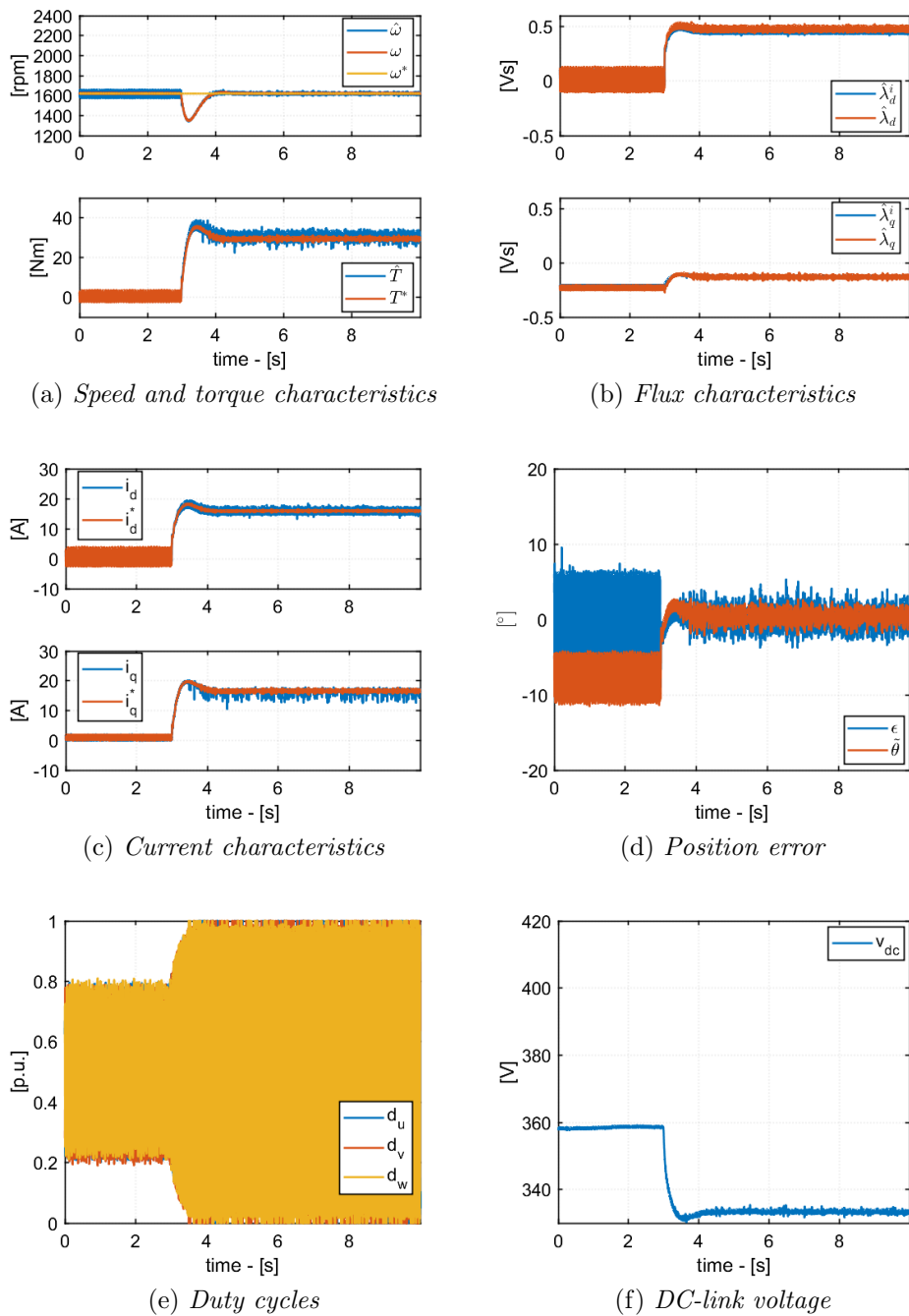
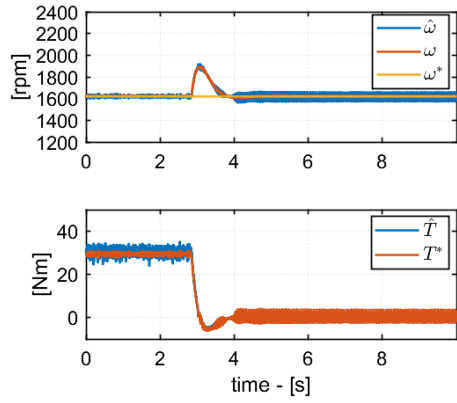
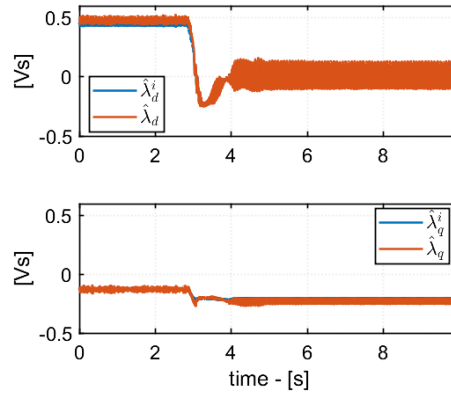


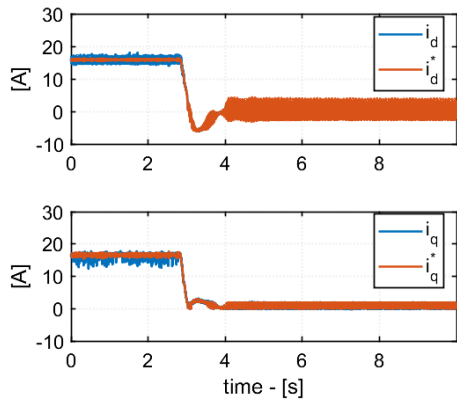
Figure 5.19: Rated torque load imposition at 80% rated speed



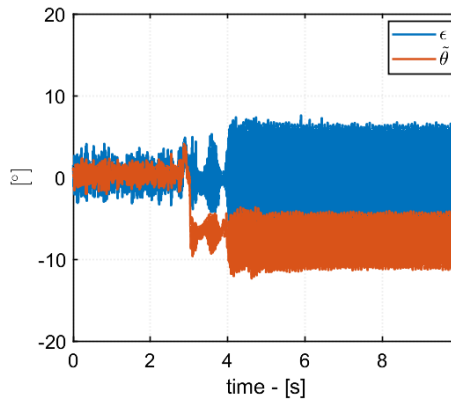
(a) Speed and torque characteristics



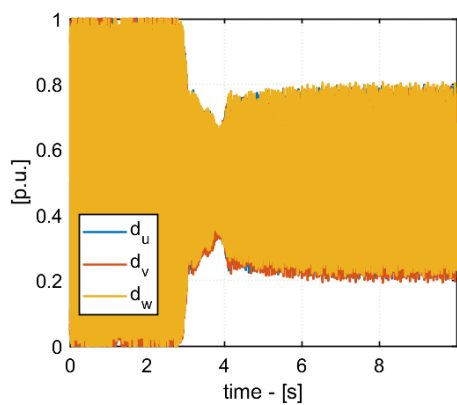
(b) Flux characteristics



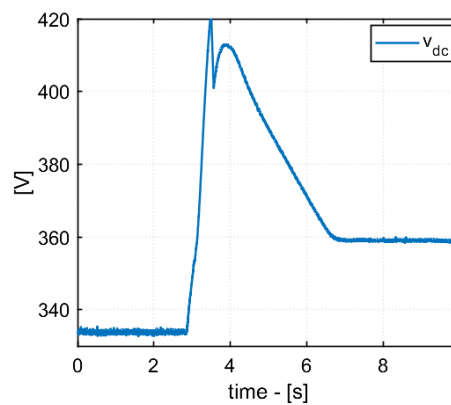
(c) Current characteristics



(d) Position error



(e) Duty cycles



(f) DC-link voltage

Figure 5.20: Rated torque load removal at 80% rated speed

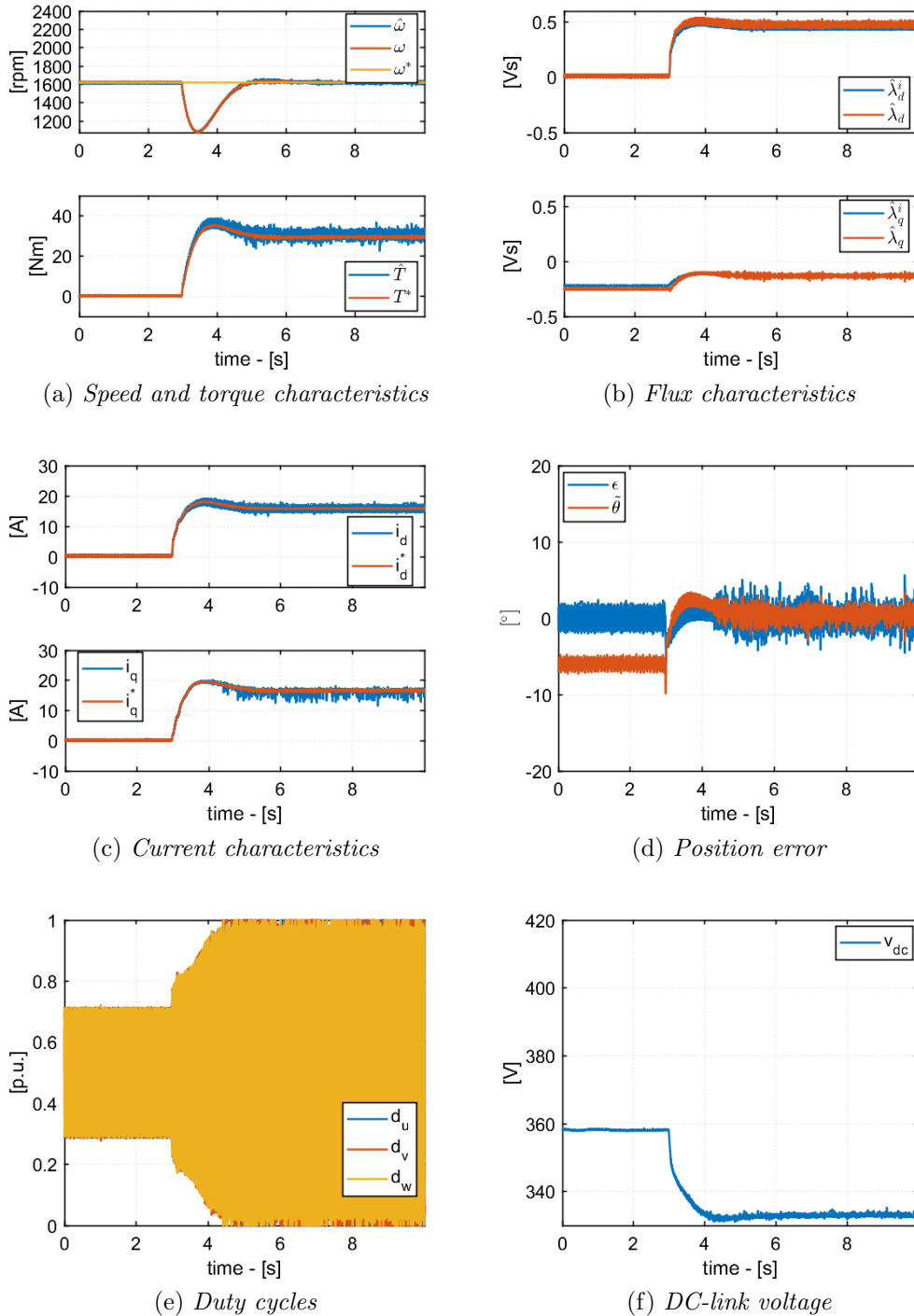


Figure 5.21: Rated torque load imposition at 80% rated speed, using 1.25 Hz speed bandwidth

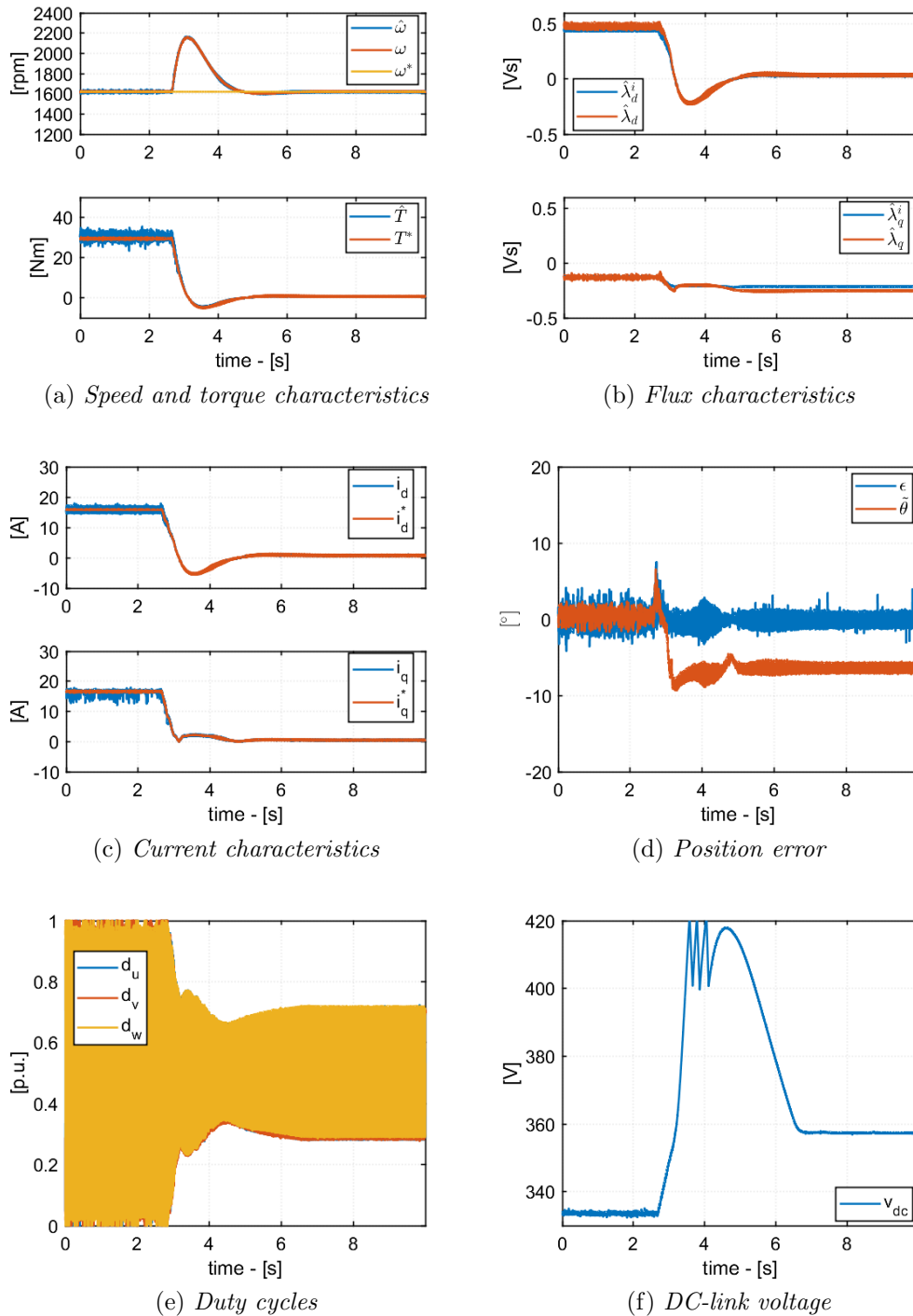


Figure 5.22: Rated torque load removal at 80% rated speed, using 1.25 Hz speed bandwidth

The same deductions for 1800 rpm case are valid for 1620 rpm case (Figure 5.19 5.20 5.21 5.22). Therefore, also with regards to rated conditions, the best solution is 2.5Hz speed bandwidth.

5.3.4 Overload test

The maximum torque that ABB motor can sustain is equal to 49.9 Nm, as shown in Figure 4.8. In fact, motor nameplate contains information about Service Factor, fixed to 1.5. The SF is the percentage of overloading the motor can handle for short periods. Therefore, the maximum current that motor can thermally withstand is:

$$\hat{I}_{max} = \sqrt{2} \cdot I_r \cdot SF = 35.4 A_{pk} \quad (5.1)$$

Using MTPA trajectory information, the maximum torque that the motor can provide with this current amplitude is around 49.7 Nm (Figure 5.23).

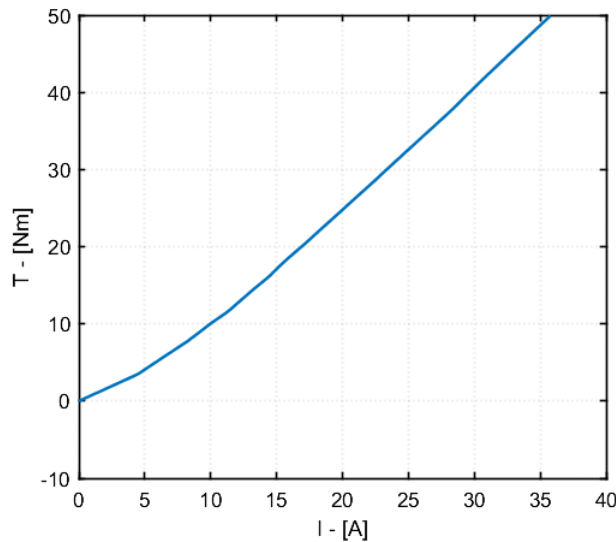
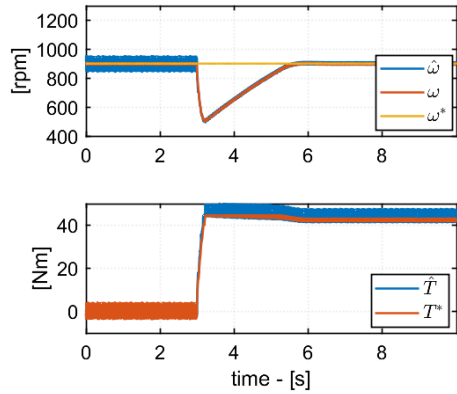


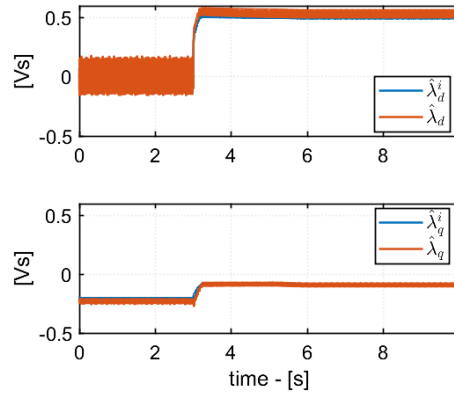
Figure 5.23: Torque characteristic

However, the motor will not be subjected to excessive thermal stress in order to prevent reduction of life. For this reason, PI speed controller output is limited to 44.5 Nm (1.49 p.u.).

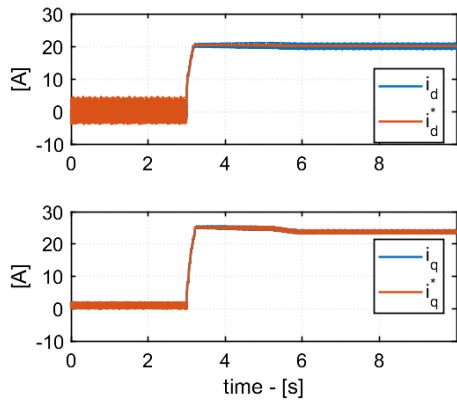
In order to understand if the adopted control strategy can bear an overload condition, a quick test is carried out, controlling the motor speed to 900 rpm and focusing on imposition and removal of 43 Nm torque load (1.45 p.u.) (Figure 5.24 and 5.25, respectively).



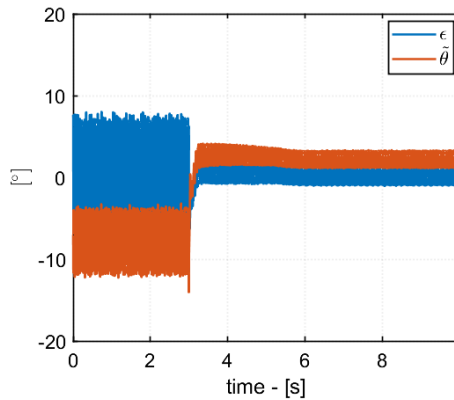
(a) Speed and torque characteristics



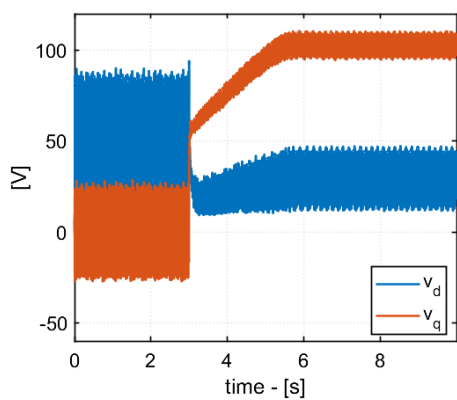
(b) Flux characteristics



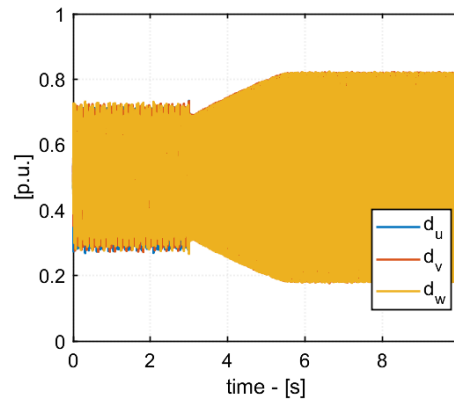
(c) Current characteristics



(d) Position error



(e) Voltage characteristics



(f) Duty cycles

Figure 5.24: Imposition of 43 Nm torque load at half rated speed

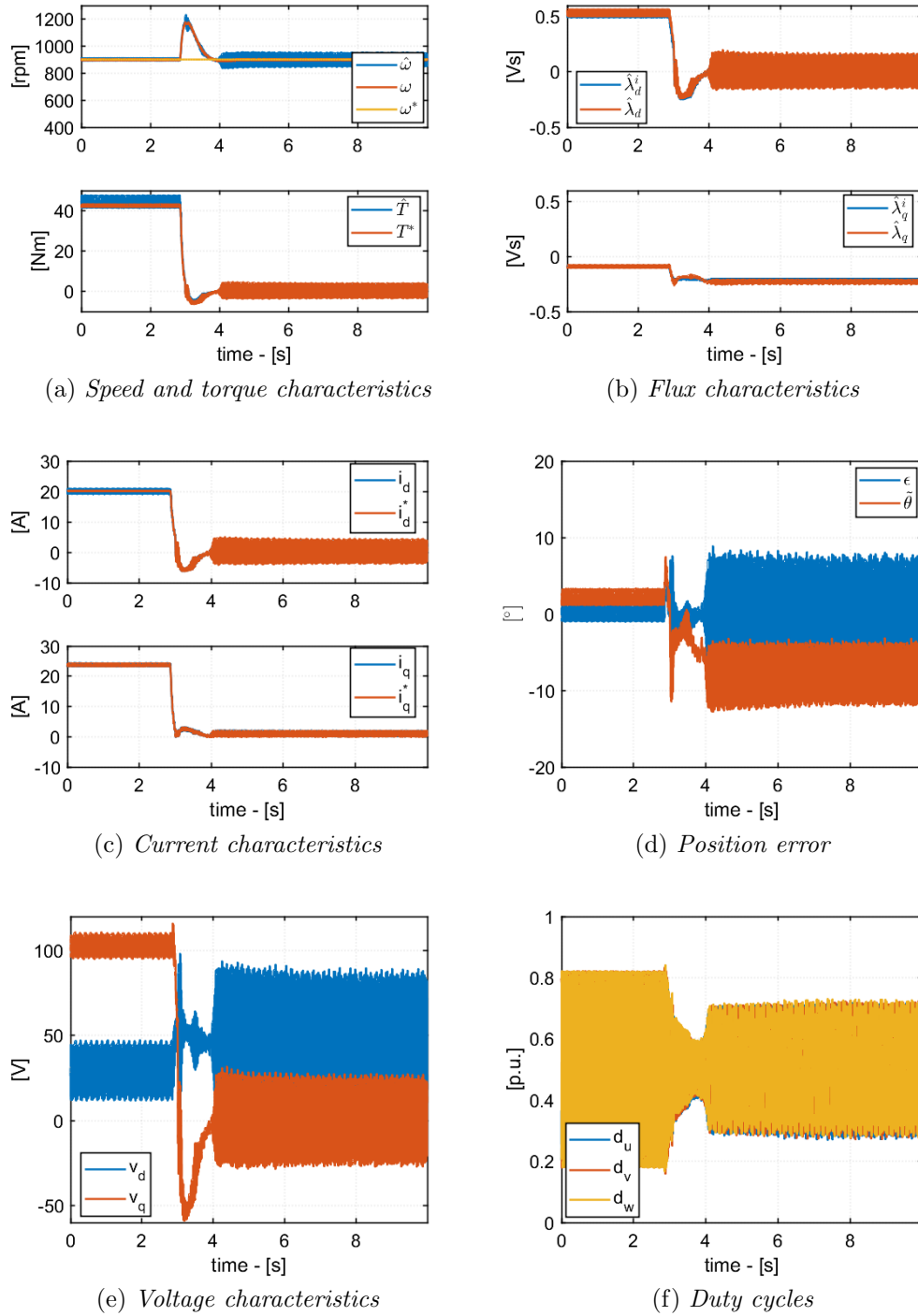


Figure 5.25: Removal of 43 Nm torque load at half rated speed

As can be seen, sensorless control properly work also in this condition, ensuring an error angle $\tilde{\theta}$ around zero degrees. Besides, reference torque does not exceed the maximum value, safeguarding motor life.

The control success was made possible also thanks to the choice of speed bandwidth. Opting for 2.5 Hz allowed to obtain a good speed dynamic during transient, ensuring a minimum speed no lower than 500 rpm. If a lower bandwidth had been chosen (for instance 1.25 Hz), motor speed would have been too low during transient and the control would not have achieved the desired convergence.

5.3.5 Harmonics Analysis

As alluded in Chapter 4, the motor under test presents a non isotropic stator shape. For this reason, electrical waveforms are not perfectly sinusoidal.

In order to try to understand causes and effects of this phenomena, the following figures illustrate motor current and flux waveforms, acquired for 200ms at steady state and in different motor conditions.

Despite stator design contributes to the non sinusoidal electrical waveforms, also the sensorless control strategy could accentuate this phenomena. Therefore, sensed FOC strategy results are compared to the sensorless one.

All the following tests are carried out imposing a reference speed equal to 900 rpm. What changes is the imposed load (4.5 Nm and rated torque), the speed bandwidth (1.25 Hz and 2.5 Hz) and the control strategy (sensed and sensorless). In the case of sensed control, it is chosen a FOC, described in section 3.1.

First of all, 4.5 Nm load case is considered. Taking into account the sensorless tests, it can be seen a first mechanical harmonic contribution in i_{dq} and i_{dq}^* : current oscillation is much higher in 2.5 Hz speed bandwidth case. A sixth electrical harmonic contribution is slightly visible in i_q : it is caused by the slot effect.

The first mechanical harmonic disturbances come from speed controller and not from current one: in fact, as it can be seen from $\alpha\beta$ plot, the reference current has the same track of the measured one. However, additional investigations are needed in order to understand the physical origin.

On the other hand, considering the sensed case, the first mechanical contribution cannot be appreciated, while the sixth electrical harmonic is barely visible in i_q . Besides, the fourth electrical harmonic contribution is evident in i_d : it is caused by the four stator cuts of the under test motor.

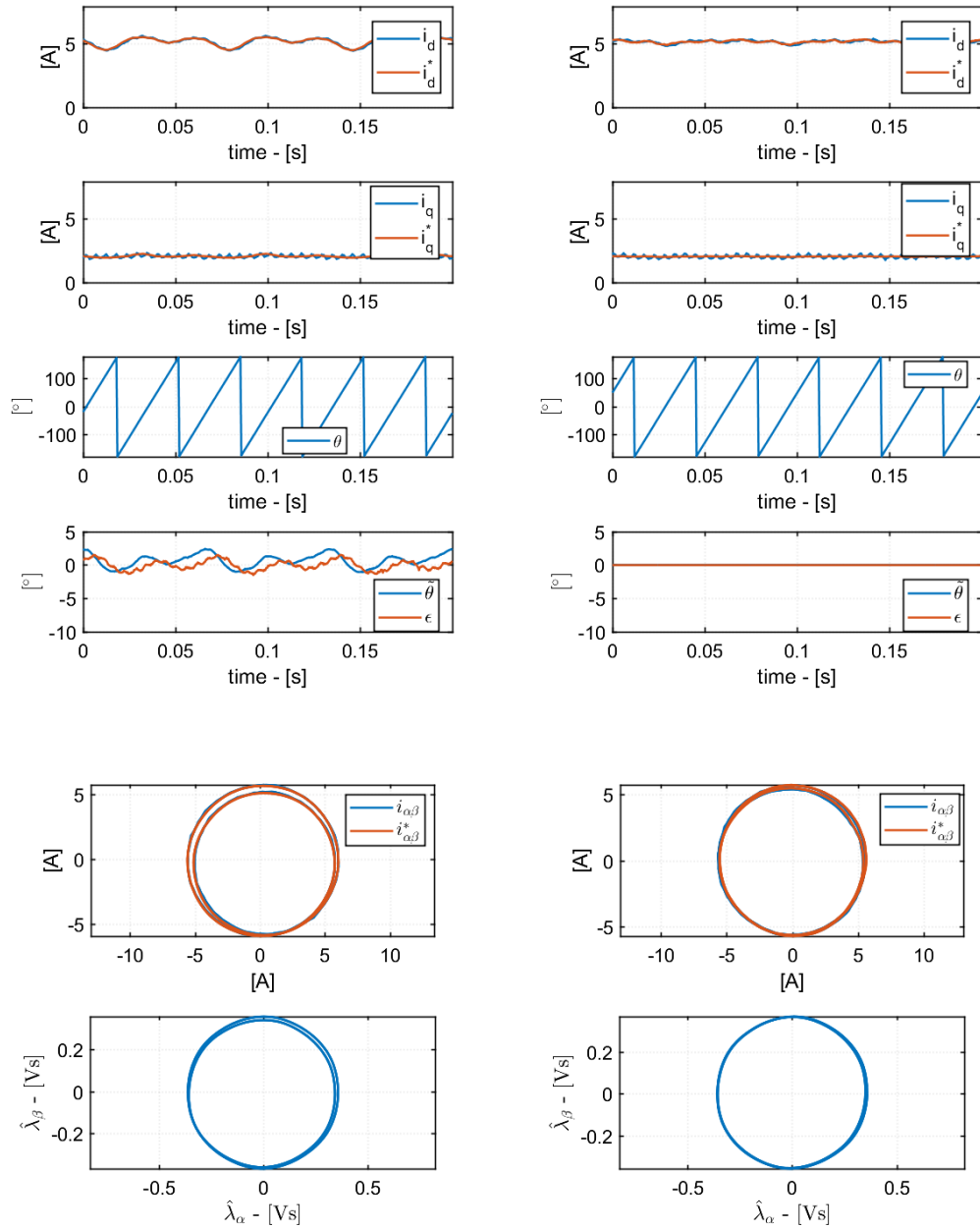


Figure 5.26: 4.5 Nm torque load sensorless (left) vs sensed (right) control, with 1.25 Hz speed bandwidth

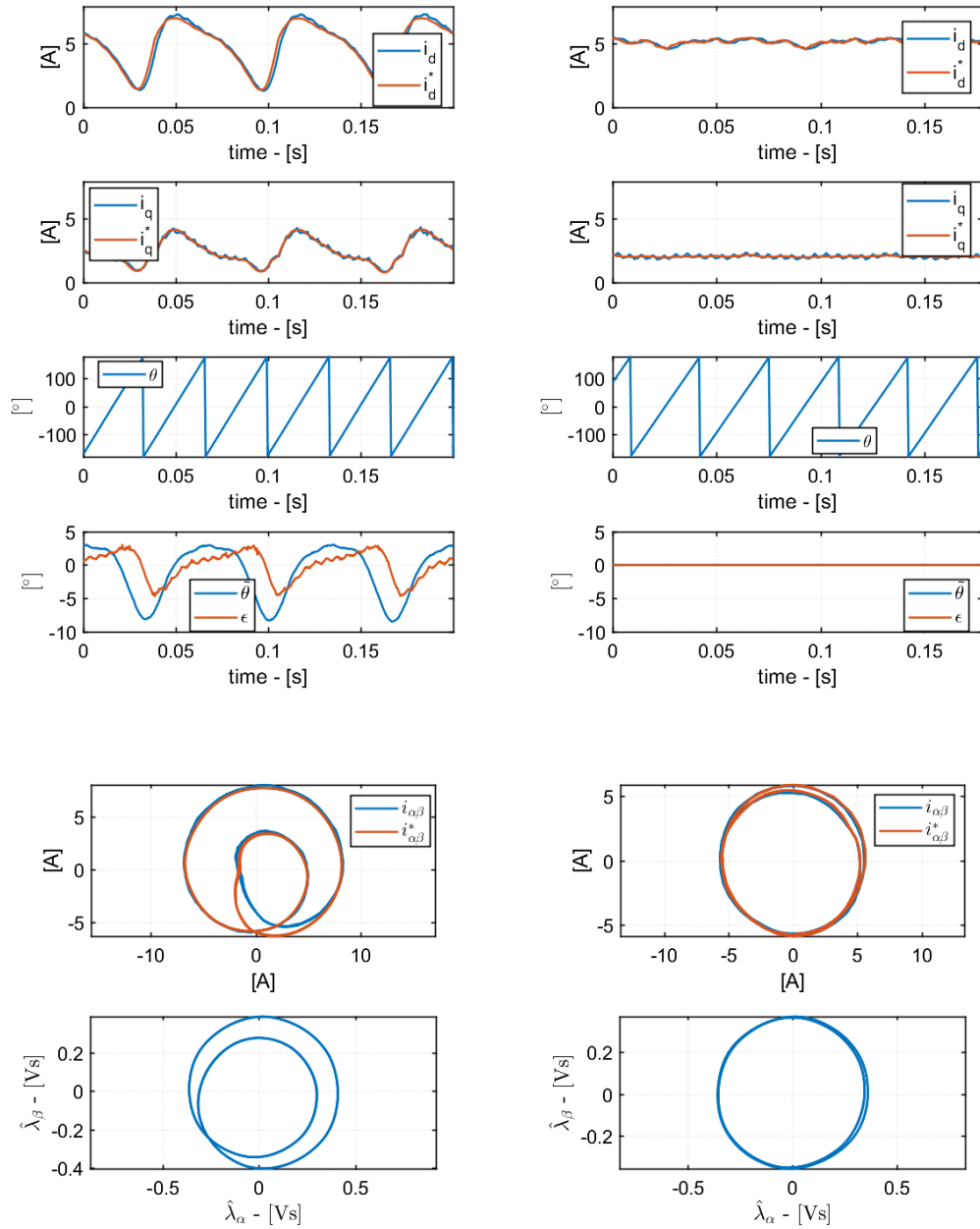


Figure 5.27: 4.5 Nm torque load sensorless (left) vs sensed (right) control, with 2.5 Hz speed bandwidth

In the last case, ABB motor bears its rated torque.

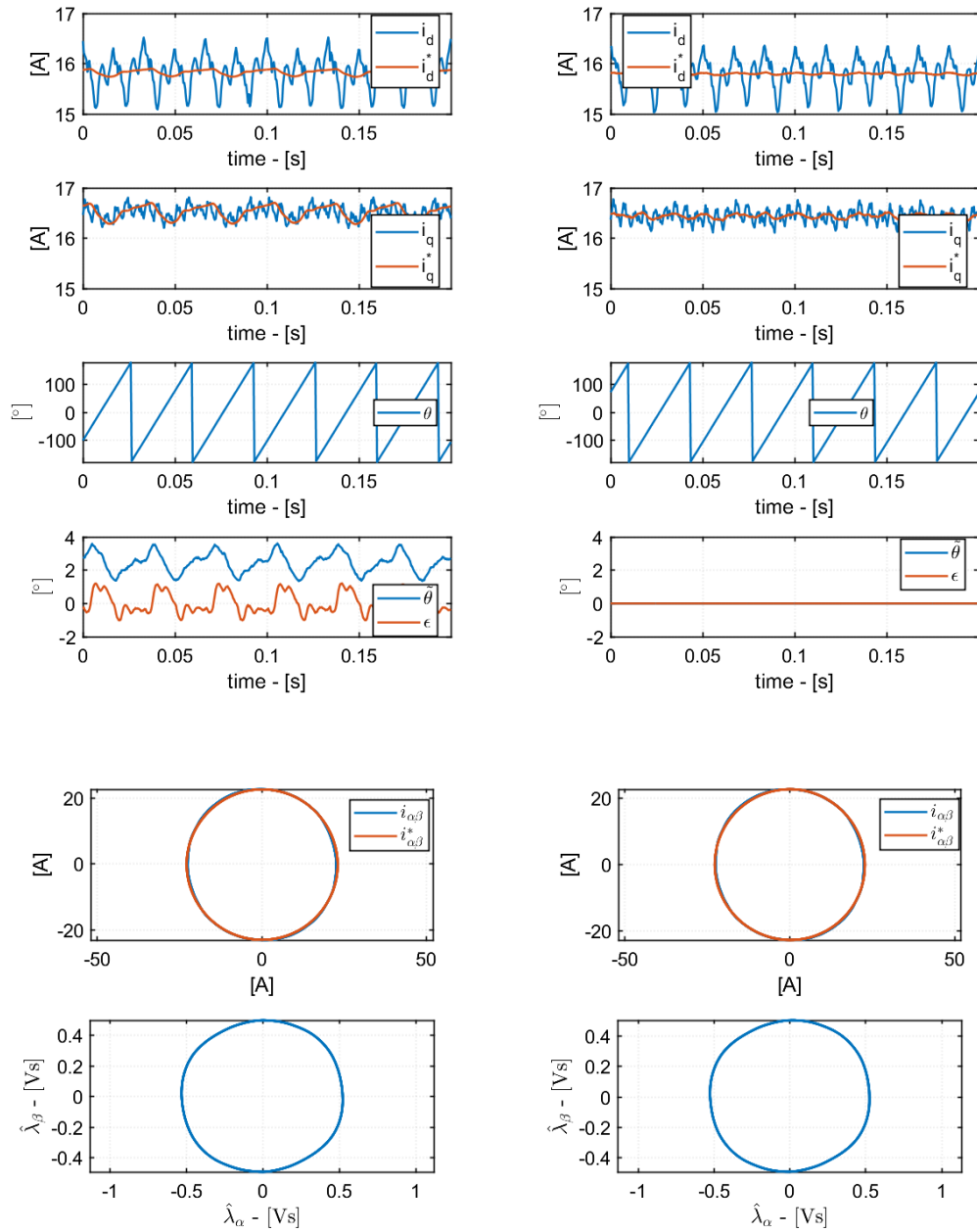


Figure 5.28: Rated torque load sensorless (left) vs sensed (right) control, with 1.25 Hz speed bandwidth

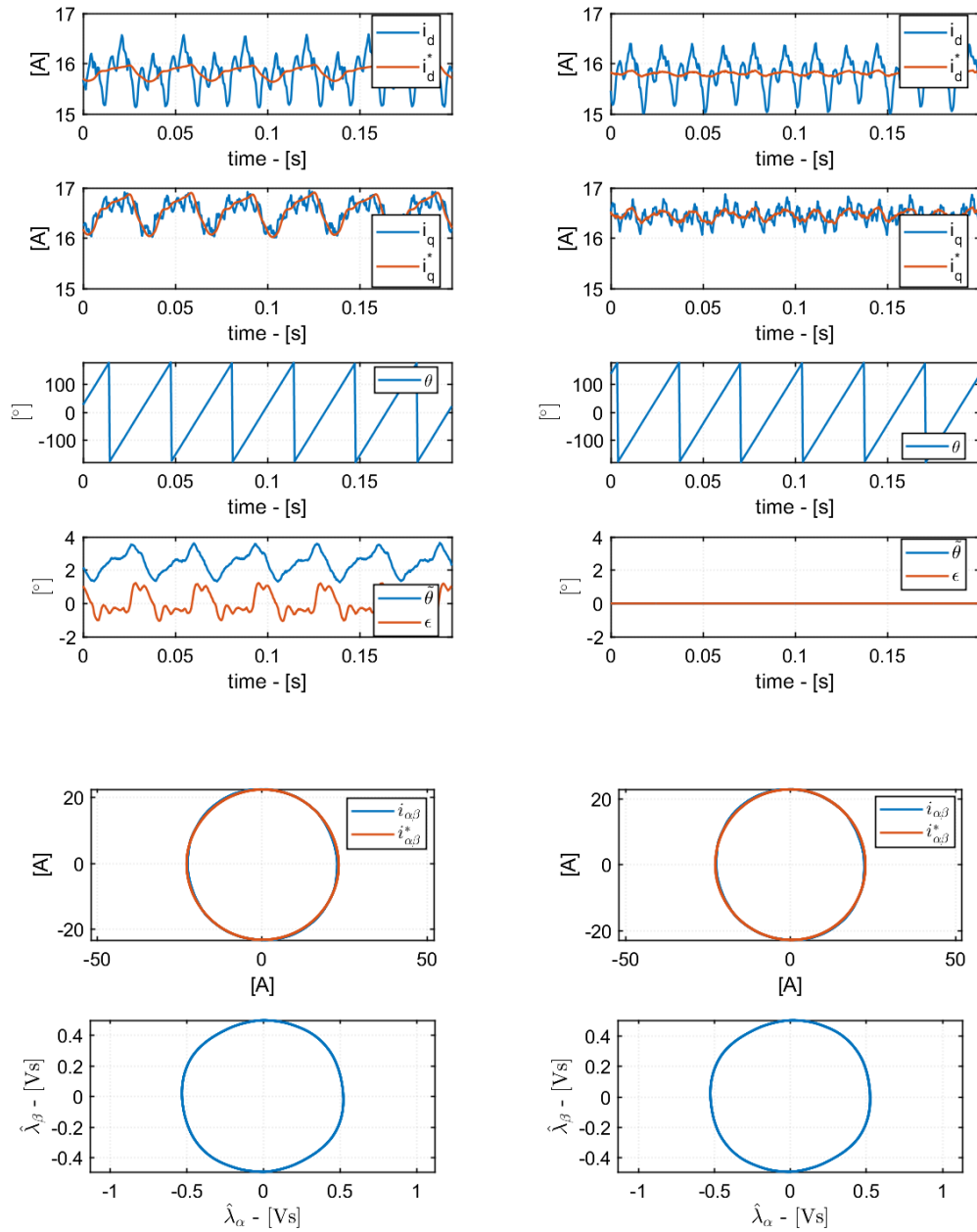


Figure 5.29: Rated torque load sensorless (left) vs sensed (right) control with, 2.5 Hz speed bandwidth

Considering the sensorless case, the first electrical harmonic contribution is present in i_d^* , i_q^* and i_d , but now there is not much difference between

1.25 Hz and 2.5 Hz speed bandwidth cases. Moreover, the fourth electrical harmonic is visible in i_q . As far as sensed case is concerned, the second electrical harmonic contribution is slightly evident in i_d^* and i_q^* , if speed bandwidth is fixed to 2.5 Hz.

Besides, for completeness the no load and 12.5 Nm torque load tests will be presented in the appendix B because they do not contain any relevant additional information.

In conclusion, focus of this thesis is not about harmonics investigation, however some experimental results were presented in order to permit further future developments about this aspect, trying to understand causes and effects.

Chapter 6

Conclusions

This work proposes a hybrid sensorless control system for PM-SyR drives, based on I-f starting method and a fast jump from open-loop speed control to sensorless field oriented control, when the machine reaches the threshold speed.

- I-f control ensures a suitable motor starting and stopping, minimizing complexity of these phases. In fact, it needs only information about measured current, whereas frequency of the rotating reference frame is arbitrary imposed. On the contrary, speed dynamic is modest.
- Sensorless FOC uses estimated speed information as feedback for the external speed loop, whereas rotor position is estimated and then exploited for Park transformation. Flux cross-product position observer permits to retrieve rotor position information, starting from the knowledge of flux linkage which is estimated thanks to a sensorless hybrid flux observer. At the end, a classical PLL filters the rotor position and calculates the electrical speed machine.
- In order to guarantee the success of the adopted strategy, several precautions have been conceived and adopted during the fast jump between the two main controls:
 - The main constraint during up transition is to properly set the initial value of the integrative part of the PI speed regulator, to avoid discontinuities in the control.
 - Downwards transition is more delicate: during the jump instant, arbitrary reference frame in I-f control must be imposed in the same position of the estimated rotor angle. Moreover, reference and estimated speed need to be almost equal when the jump is

occurred. Finally, in order to obtain a smoother transition, it is recommended to use reference current allocated into zero torque locus: in fact, I-f control is inherently unstable for dq operating points on and over the MTPA trajectory. Therefore, it is desirable to move as far away from MTPA as possible when jumping to I-f.

Compared to many methods, which use a smooth and gradual transition, the proposed strategy opts for a fast and abrupt jump between I-f control and sensorless FOC, obtaining very good results thanks to the adoption of several specific precautions, before, during and after the jump.

The good performance and robustness of this method has been widely demonstrated by both simulation and experimental results:

- Simulation tests, in simulink environment, were conducted in order to verify the feasibility and the prospects of the proposed control. According to the final motor application, acceleration and deceleration tests with different conditions (load, reference current during I-f control and dead-time compensation) are carried out.
- Experimental tests were conducted on a test bench in order to validate the proposed control strategy. It is tested in its frequent working condition, focusing on acceleration and deceleration with no load or reduced load. In addition, the proposed method can afford nominal load and overload conditions. Motor dynamic can be considered satisfactory, taking into account motor dimensions and characteristics of the typical used sensorless control in literature.

Motor application does not request a control strategy capable of working at zero speed. In fact, the adopted method exploits I-f control only as a starting procedure. Therefore, in order to guarantee also zero speed control, a high frequency injection method could be implemented, substituting I-f control. This way, sensorless FOC will use rotor position information coming from cross-product method when motor voltage is enough, otherwise from HF injection. The suggested method will guarantee a wider operating area, but increasing strategy complexity.

In conclusion, an easy and successful method to sensorless control PM-SyR motor is found. Thanks to the precautions adopted and the chosen tuning, convergence is always guarantee. Speed dynamic is quite good, imposing 2.5 Hz speed bandwidth. Moreover, there is no limit slew-rate during acceleration in sensorless FOC, whereas during I-f control it is limited to 400 rpm/s. As far as starting under load is concerned, despite not requested by application, machine drive can bear 40.2% of its torque load, using 68.5% of

the motor rated current during I-f control. All these results are supported by experimental tests carried out directly on ABB drive.

Appendix A

Implemented control code

This appendix presents c-algorithm used to sensorless control PM-SyR motor. In particular, the showed code highlights the *control routine*, which includes:

- I-f control;
- Sensorless FOC;
- Sensorless HFO;
- Cross-product.
- PLL;

```
18 void Control_Routine()
19 {
20     //speed and angle ref
21     ramp(wrpmRef_R * rpm2rad , accel * rpm2rad *Tsw, &omega_ref_ramp); //rad/s mec
22     Gen_theta_ref(omega_ref_ramp * pR, &theta_ref, &SinCos_ref); //theta elt ref
23     if (theta_ref<=-pi) // saturo in modo da avere un angolo tra -pi e pi
24         theta_ref+=two_pi;
25     if (theta_ref>=pi)
26         theta_ref-=two_pi;
27
28     //clarke curr
29     Clarke(&iUVW_R, &iabR); //calcolo iabR
30
31     //Flux obs
32     FluxObserver();
33
34     //CROSS PRODUCT
35     SinCos_obs.sin = (lambdaS_est_dqR.d * lambdaS_obs.b - lambdaS_obs.a * lambdaS_est_dqR.q) * (inv_amp_fluxobs * inv_amp_fluxobs);
36     SinCos_obs.cos = (lambdaS_est_dqR.d * lambdaS_obs.a + lambdaS_obs.b * lambdaS_est_dqR.q) * (inv_amp_fluxobs * inv_amp_fluxobs);
37
38     //PLL
39     PLL();
40
41     //CONTROL TYPE - 0:CURRENT CONTROL 1:TORQUE CONTROL 2:I/Hz 3:SPEED CONTROL
42     switch (Ctrl_type)
43     {
```

```

114
115
116
117
118
119
120
121
122
123
124
125
126
127
128
129
130
131
132
133
134
135
136
137
138
139
140
141
142
143
144
145
146
147
148
149
150
151
152
153
154
155
156
157
158
159
160
161
162
163
164
165
166
167
168
169
170
171
172
173
174

case 2:

    //rot corr
    Rot(&iabR,&idqR,&SsinCos_ref); //I Hs

    // * Anello asse d
    id_var_R.ref = idqRefInput_R.d;
    id_var_R.actual = idqR.d;
    id_var_R.lim = SQRT1OVER3 * vdc_filt;
    id_var_R.vfw = 0.0;
    PIReg(&id_par_R, &id_var_R);
    vdqR.d = id_var_R.out;
    // * Anello asse q
    iq_var_R.ref = idqRefInput_R.q;
    iq_var_R.actual = idqR.q;
    iq_var_R.lim = sqrt(id_var_R.lim * id_var_R.lim - id_var_R.out * id_var_R.out);
    iq_var_R.vfw = 0.0;
    PIReg(&iq_par_R, &iq_var_R);
    vdqR.q = iq_var_R.out;

    // - Rotazioni tens
    InvRot(&vdqR, &vabR, &SsinCos_ref); //I Hs

    //JUMP I-f to FOC
    if (omega_ref_ramp * rad2rpm > 400.0) {
        Ctrl_type = 3;
        omega_R_var.integral = T_est_fluxobs; //inializzo integratore speed loop
        // accel = 1500000.0;
    }

    break;

case 3:

    //rot corr
    if(SS_ctrl == 1)
        Rot(&iabR,&idqR,&SsinCos_pll_elt); //sensorless
    else
        Rot(&iabR,&idqR,&SsinCos_R); //sensored

    //speed loop
    omega_R_par.kp = 2 * (2 * pi * poles_omega) * inertia_tot;
    omega_R_par.ki = (2 * pi * poles_omega) * (2 * pi * poles_omega) * inertia_tot;

    omega_R_var.ref = omega_ref_ramp; //wrpmRef_R * rpm2rad; // rad/s mec
    if(SS_ctrl == 1)
        omega_R_var.actual = omega_pll_mec; //
    else
        omega_R_var.actual = omega_meas_mecc_R_f;

    omega_R_var.vfw = 0.0;
    omega_R_var.lim = 29.7*1.5;
    PIReg(&omega_R_par, &omega_R_var);
    Tref = omega_R_var.out;

    //MTPA tables
    ReadLut(&ID_REF[0], fabs(Tref), TMAX, TMIN, DT, INV_DT, &idqR_ref.d);
    ReadLut(&IQ_REF[0], fabs(Tref), TMAX, TMIN, DT, INV_DT, &idqR_ref.q);
    if (Tref<0) idqR_ref.d = -idqR_ref.d; //d if FMSR

```

```

170 //MTPA tables
171 ReadLut(&ID_REF[0], fabs(Tref), TMAX, TMIN, DT, INV_DT, &idqR_ref.d);
172 ReadLut(&IQ_REF[0], fabs(Iref), TMAX, TMIN, DT, INV_DT, &idqR_ref.q);
173 if (Tref<0) idqR_ref.d = -idqR_ref.d; //d if PMASR
174
175 //feed forward
176 if (ffw == 1) { //feed forward ON
177     vsdq_ref_ffw.d = Rs_R * idqR_ref.d - omega_pll_elt_f * lambdaS_obs_dqR.q;
178     vsdq_ref_ffw.q = Rs_R * idqR_ref.q + omega_pll_elt_f * lambdaS_obs_dqR.d;
179 }else{ //OFF
180     vsdq_ref_ffw.d = 0.0;
181     vsdq_ref_ffw.q = 0.0;
182 }
183
184 //d-axis current control loop
185 id_var_R.ref = idqR_ref.d;
186 id_var_R.actual = idqR.d;
187 id_var_R.lim = SQRT1OVER3 * vdc_filt;
188 id_var_R.vfw = 0.0;
189 PIReg(&id_par_R, &id_var_R);
190 vdqR.d = id_var_R.out + vsdq_ref_ffw.d;
191
192 //q-axis current control loop
193 iq_var_R.ref = idqR_ref.q;
194 iq_var_R.actual = idqR.q;
195 iq_var_R.lim = sqrt(vdc_filt*vdc_filt/3 - vdqR.d * vdqR.d);
196 iq_var_R.vfw = 0.0;
197 PIReg(&iq_par_R, &iq_var_R);
198 vdqR.q = iq_var_R.out + vsdq_ref_ffw.q;
199
200 // vdqR.d = vdqR.d + vsdq_ref_ffw.d;
201 // vdqR.q = vdqR.q + vsdq_ref_ffw.q;
202
203 // - Rotazioni
204 if(SS_ctrl == 1)
205     InvRot(&vdqR, &vabR, &SinCos_pll_elt); //calcolo vab ->I-f
206 else
207     InvRot(&vdqR, &vabR, &SinCos_R); //calcolo vab ->I-f
208
209 if(omega_ref_ramp * rad2rpm > 1799.0) test=1.0;
210
211 if (test == 1.0 && omega_ref_ramp * rad2rpm <1700) {
212     accel = 500.0;
213 }
214
215 if (test == 1.0 && omega_ref_ramp * rad2rpm <500) {
216     accel = 100.0;
217 }
218
219 if(omega_pll_mec * rad2rpm < 300.0) {
220
221     Ctrl_type = 2;
222     theta_ref = theta_pll_elt;
223     test = 0.0;
224 }
225
226 break;
227 }
228
229 /*Calcolo dei duty cycle
230 InvClarke(&vabR, &V_UVW_R);
231 PWMCompute(&V_UVW_R, &duty_UVW_R, &vdc_filt);
232

```

```

239 //Sensorless hybrid flux observer
240 void FluxObserver(void) {
241
242     G_obs = TWOPI * poles_fluxobs;
243
244     lambdaS_obs_dqR_kml = lambdaS_obs_dqR; //save old flux obs dq
245     lambdaS_estR_kml = lambdaS_estR; //save old flux est ab
246
247     if(SS_ctrl == 1)
248         Rot(&iabR, &idqR_fluxobs, &SinCos_pll_elt);
249     else
250         Rot(&iabR, &idqR_fluxobs, &SinCos_R);
251
252     interp2d_flux(&FD_LUT[0][0], fabs(idqR_fluxobs.d), (idqR_fluxobs.q), DIDD, INV_DIDD, DIQD, INV_DIQD, ID_TA
253     interp2d_flux(&FQ_LUT[0][0], (idqR_fluxobs.q), fabs(idqR_fluxobs.d), DIQQ, INV_DIQQ, DIQD, INV_DIQD, IQ_TA
254     if (idqR_fluxobs.d < 0)
255         lambdaS_est_dqR.d = -lambdaS_est_dqR.d;
256
257     if(SS_ctrl == 1)
258         InvRot(&lambdaS_est_dqR, &lambdaS_estR, &SinCos_pll_elt);
259     else
260         InvRot(&lambdaS_est_dqR, &lambdaS_estR, &SinCos_R);
261
262     error_flux.a = lambdaS_estR_kml.a - lambdaS_obs.a; //(k-1)
263     error_flux.b = lambdaS_estR_kml.b - lambdaS_obs.b;
264
265     // Integration
266     lambdaS_obs.a += Tsw*(vab_fromCode_DROP_kml.a - Rs_R * iabR.a + G_obs * error_flux.a);
267     lambdaS_obs.b += Tsw*(vab_fromCode_DROP_kml.b - Rs_R * iabR.b + G_obs * error_flux.b);
268
269     if(SS_ctrl == 1)
270         Rot(&lambdaS_obs, &lambdaS_obs_dqR, &SinCos_pll_elt);
271     else
272         Rot(&lambdaS_obs, &lambdaS_obs_dqR, &SinCos_R);
273
274     amp_fluxobs=amplitude(lambdaS_obs.a,lambdaS_obs.b);
275     if(amp_fluxobs > 0.1)
276         inv_amp_fluxobs = 1.0 / amp_fluxobs;
277     else
278         inv_amp_fluxobs = 1.0 / 0.1;
279
280     T_est_fluxobs = 1.5 * pR * (lambdaS_estR.a*iabR.b - lambdaS_estR.b*iabR.a);
281
282 }

```

```

284 void PLL(void) {
285
286     //tuning
287     omega_pll_par.kp = 2* (2 * pi * poles_pll); //critical damping
288     omega_pll_par.ki = (2 * pi * poles_pll) * (2 * pi * poles_pll); //critical damping
289
290     if(SS_ctrl == 1)
291         pos_err_signal = (SinCos_obs.sin * SinCos_pll_elt.cos) - (SinCos_obs.cos * SinCos_pll_elt.sin); //cross product
292         // pos_err_signal = (lambdaS_obs_dqR.d - lambdaS_est_dqR.d)/0.2; //active flux
293     else
294         pos_err_signal = 0;
295
296     if (omega_ref_ramp * rad2rpm < 100.0) {
297         pos_err_signal = 0;
298         omega_pll_var.integral = omega_ref_ramp * pR; }
299
300     if ( pos_err_signal > 20 * deg2rad)
301         pos_err_signal = 20 * deg2rad;
302     if ( pos_err_signal < -20 * deg2rad)
303         pos_err_signal = -20 * deg2rad;
304
305     omega_pll_var.ref = pos_err_signal;
306     omega_pll_var.actual = 0.0;
307     omega_pll_var.vfw = 0.0;
308     omega_pll_var.lim = 753.0; // (2pi*60) * 2
309     PIReg(&omega_pll_par, &omega_pll_var);
310
311     if(SS_ctrl == 0)
312         omega_pll_var.integral = omega_meas_elt_R_f; //sensored speed
313
314     omega_pll_elt = omega_pll_var.out;
315
316     if(SS_ctrl == 1)
317         theta_pll_elt = theta_pll_elt + Tsw * omega_pll_elt; //sensorless elt angle
318     else
319         theta_pll_elt = enc_R.the; //sensored elt angle
320
321     if (omega_ref_ramp * rad2rpm < 100.0)
322         theta_pll_elt = theta_ref;
323
324     if (theta_pll_elt<=-pi)
325         theta_pll_elt+=two_pi;
326     if (theta_pll_elt>=pi)
327         theta_pll_elt-=two_pi;
328
329     //SinCos
330     SinCos_pll_elt.sin = sin(theta_pll_elt);
331     SinCos_pll_elt.cos = cos(theta_pll_elt);
332
333     //filt speed
334     Filter(&omega_pll_elt, &omega_pll_elt_f, PLL_filt);
335     omega_pll_mec = omega_pll_elt_f / pR;
336
337     //theta error
338     theta_error_elt = asin(sin(enc_R.the - theta_pll_elt));
339
340 }

```

Appendix B

Harmonics analysis

The following figures show current, estimated flux and position error of the ABB motor when it works at half rated speed with zero and 12.5 Nm torque load. All this data are acquired only for $200\mu s$, in order to pay attention on harmonic contribution. These tests are carried out both using the adopted sensorless method and the sensed one. Moreover, for each case, speed bandwidth is fixed to 1.25 Hz and 2.5 Hz.

B.1 No load

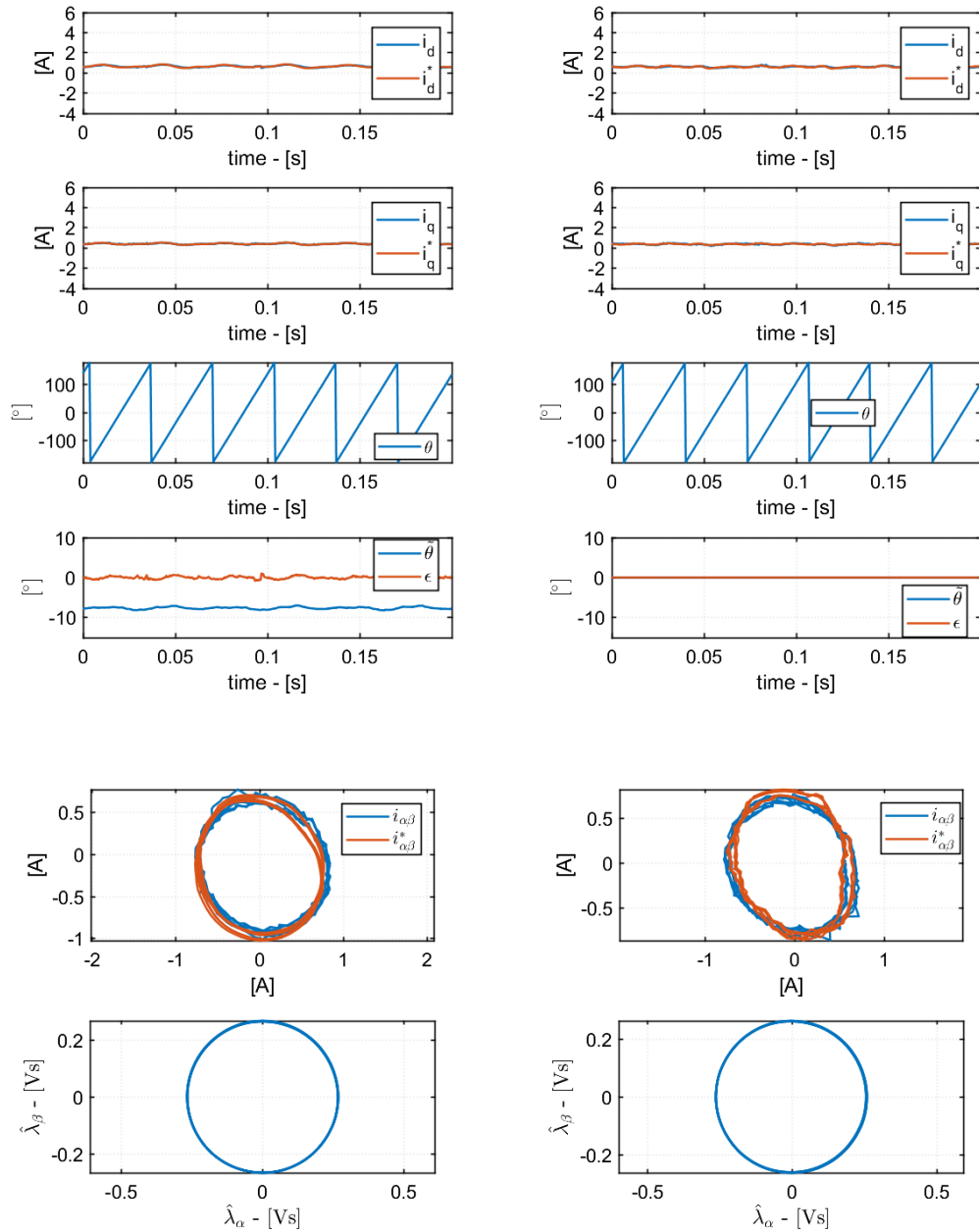


Figure B.1: No load sensorless (left) vs sensed (right) control, with 1.25 Hz speed bandwidth

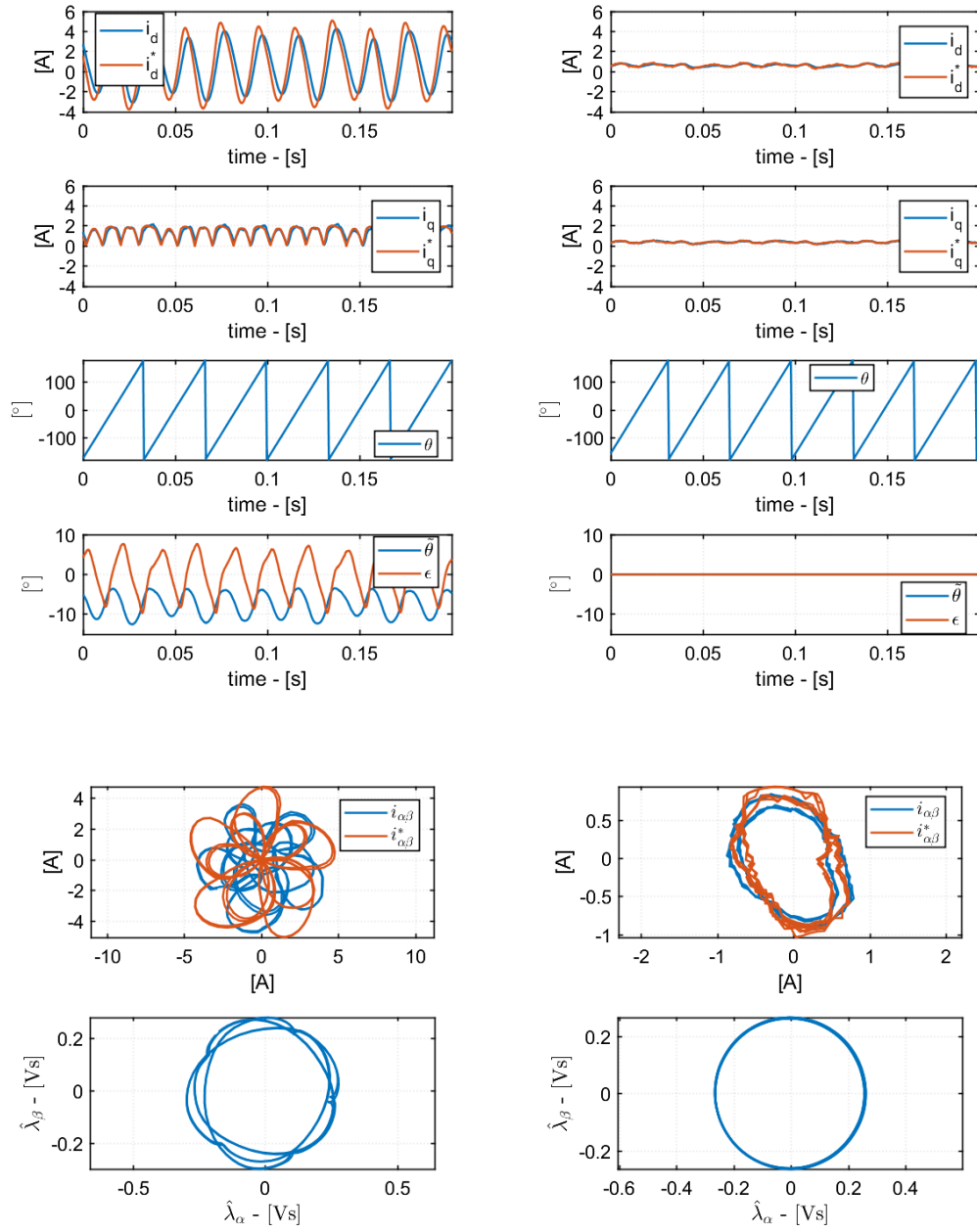


Figure B.2: No load sensorless (left) vs sensed (right) control, with 2.5 Hz speed bandwidth

B.2 12.5Nm torque load

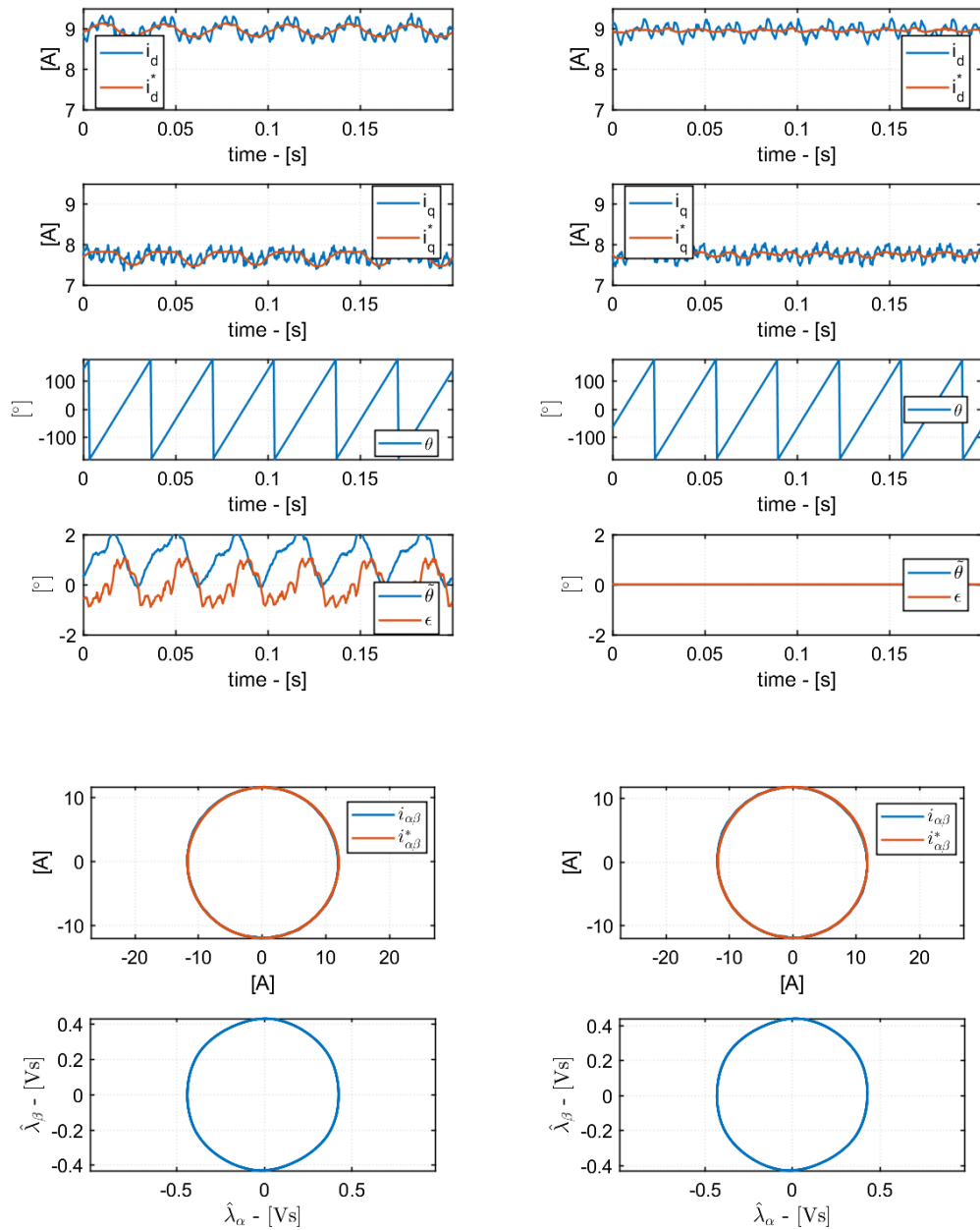


Figure B.3: 12.5 Nm torque load sensorless (left) vs sensed (right) control, with 1.25 Hz speed bandwidth

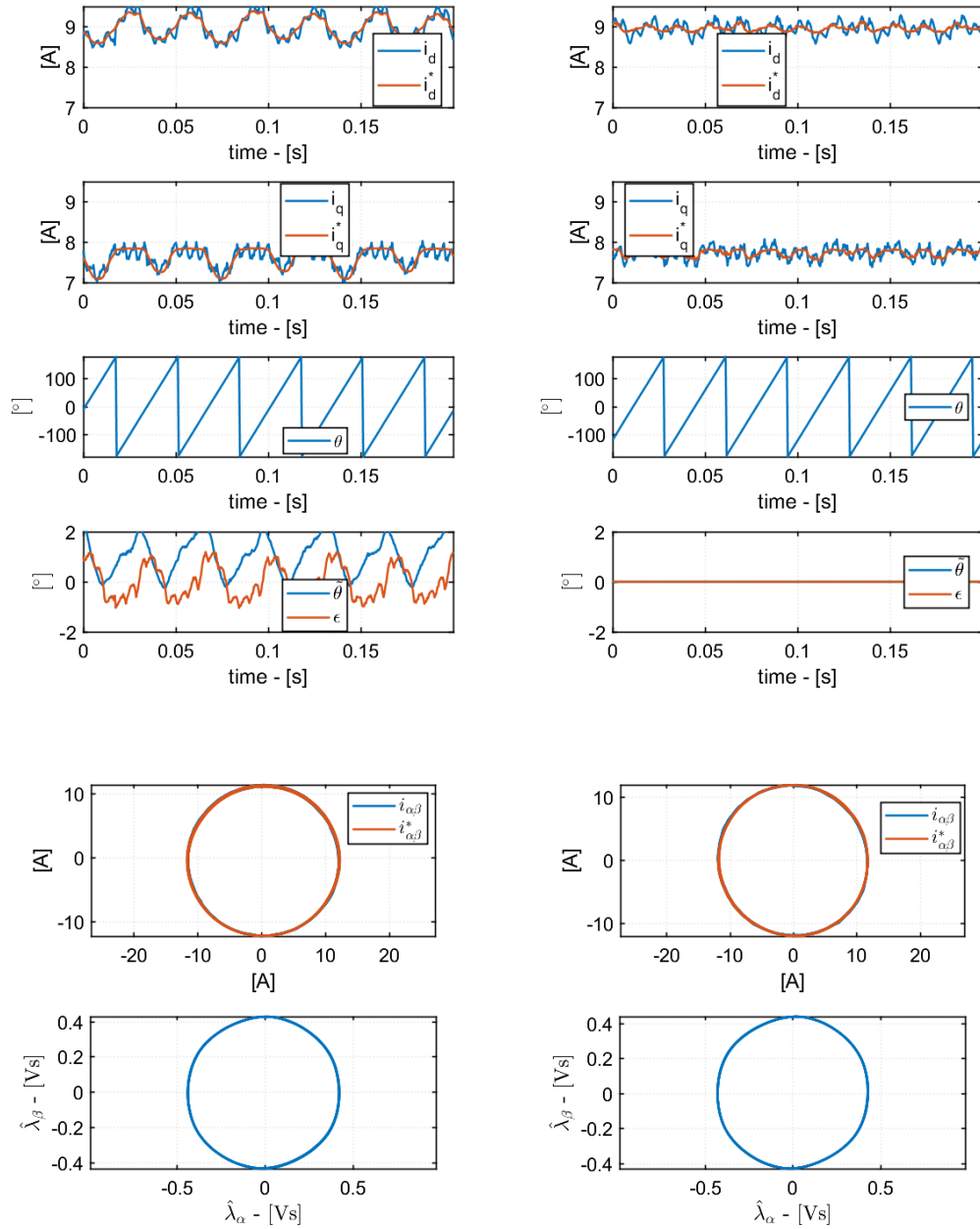


Figure B.4: 12.5 Nm torque load sensorless (left) vs sensed (right) control, with 2.5 Hz speed bandwidth

Bibliography

- [1] Enerdata. *Global Energy Statistical Yearbook*. 2020. URL: <https://yearbook.enerdata.net/electricity/electricity-domestic-consumption-data.html> (visited on 11/27/2020).
- [2] Joon Han and Sun-Jin Yun. “An analysis of the electricity consumption reduction potential of electric motors in the South Korean manufacturing sector”. In: *Energy Efficiency* 8 (Dec. 2015). DOI: 10.1007/s12053-015-9335-5.
- [3] Jorma Haataja and Juha Pyrhönen. “Permanent Magnet Assisted Synchronous Reluctance Motor: an Alternative Motor in Variable Speed Drives”. In: *Energy Efficiency in Motor Driven Systems*. Ed. by Francesco Parasiliti and Paolo Bertoldi. Berlin, Heidelberg: Springer Berlin Heidelberg, 2003, pp. 101–110. ISBN: 978-3-642-55475-9.
- [4] E. Armando et al. “Accurate Modeling and Performance Analysis of IPM-PMASR Motors”. In: *IEEE Transactions on Industry Applications* 45.1 (2009), pp. 123–130. DOI: 10.1109/TIA.2008.2009493.
- [5] E. Armando et al. “Performance of IPM-PMASR Motors with Ferrite Injection for Home Appliance Washing Machine”. In: (2008), pp. 1–6. DOI: 10.1109/08IAS.2008.19.
- [6] P. Guglielmi et al. “Position-sensorless control of permanent-magnet-assisted synchronous reluctance motor”. In: *IEEE Transactions on Industry Applications* 40.2 (2004), pp. 615–622. DOI: 10.1109/TIA.2004.824438.
- [7] R.Bojoi. *Power electronics for smart grids: fundamental concepts in static electrical energy conversion*. Version English. Italy, Nov. 2019.
- [8] Bimal Bose. “Modern Power Electronics and AC Drives”. In: Jan. 2002. ISBN: 0-13-016743-6.
- [9] Radu Bojoi et al. “Direct Flux Vector Control of Axial Flux IPM Motors for in-wheel traction solutions”. In: Dec. 2010, pp. 2224–2229. DOI: 10.1109/IECON.2010.5674955.

- [10] Hyung-Tae Moon, Hyun-Soo Kim, and Myung-Joong Youn. "A discrete-time predictive current control for PMSM". In: *IEEE Transactions on Power Electronics* 18.1 (2003), pp. 464–472. DOI: 10.1109/TPEL.2002.807131.
- [11] G.Pellegrino. *Sensorless control of synchronous motor drives - Laboratory of power converters and electrical drives*. Version English. Italy, Mar. 2020.
- [12] I.Westin. "Sensorless Control of a PMSM: Evaluation of Different Speed and Position Estimation Methods Suitable for Control of aPMSM". Master thesis. KTH ROYAL INSTITUTE OF TECHNOLOGY, 2016.
- [13] I. Boldea et al. "'Active Flux' DTFC-SVM Sensorless Control of IPMSM". In: *IEEE Transactions on Energy Conversion* 24.2 (2009), pp. 314–322. DOI: 10.1109/TEC.2009.2016137.
- [14] I. Boldea and S. C. Agarlita. "The active flux concept for motion-sensorless unified AC drives: A review". In: *International Aegean Conference on Electrical Machines and Power Electronics and Electromotion, Joint Conference*. 2011, pp. 1–16. DOI: 10.1109/ACEMP.2011.6490561.
- [15] S. Agarlita, I. Boldea, and F. Blaabjerg. "High frequency injection assisted "active flux" based sensorless vector control of reluctance synchronous motors, with experiments from zero speed". In: *2011 IEEE Energy Conversion Congress and Exposition*. 2011, pp. 2725–2732. DOI: 10.1109/ECCE.2011.6064134.
- [16] Zhiqian Chen et al. "An extended electromotive force model for sensorless control of interior permanent-magnet synchronous motors". In: *IEEE Transactions on Industrial Electronics* 50.2 (2003), pp. 288–295. DOI: 10.1109/TIE.2003.809391.
- [17] C.Mantala. "Sensorless control of brushless permanent magnet motors". PhD thesis. KTH ROYAL INSTITUTE OF TECHNOLOGY, 2013.
- [18] F. Briz and M. W. Degner. "Rotor Position Estimation". In: *IEEE Industrial Electronics Magazine* 5.2 (2011), pp. 24–36. DOI: 10.1109/MIE.2011.941118.
- [19] P. L. Jansen and R. Lorenz. "Transducerless position and velocity estimation in induction and salient AC machines". In: *Proceedings of 1994 IEEE Industry Applications Society Annual Meeting* 1 (1994), 488–495 vol.1.

- [20] A. Varatharajan, G. Pellegrino, and E. Armando. "Sensorless Synchronous Reluctance Motor Drives: Auxiliary Flux based Position Observer". In: *IEEE Journal of Emerging and Selected Topics in Power Electronics* (2020), pp. 1–1. DOI: 10.1109/JESTPE.2020.3019568.
- [21] F. Blaschke. "A New Method for the Structural Decoupling of AC Induction Machine". In: *2nd IFAC Symp. on Multivariable Technical Control Systems* (1971).
- [22] Q. Al azze. "Field-Oriented Control of Permanent Magnet Synchronous Motors Based on DSP Controller". Master thesis. Southern Illinois University Edwardsville, 2014.
- [23] R. Rossi. "Design of a PMSM Field-Oriented Control Algorithm with Flux-Weakening for Battery Electric Vehicles". Master thesis. Politecnico di Torino, 2019.
- [24] G. Pellegrino. *Control of PM and Reluctance Synchronous Machines - Laboratory of power converters and electrical drives*. Version English. Italy, Mar. 2020.
- [25] E. Armando et al. "Experimental Identification of the Magnetic Model of Synchronous Machines". In: *IEEE Transactions on Industry Applications* 49.5 (2013), pp. 2116–2125. DOI: 10.1109/TIA.2013.2258876.
- [26] P. Guglielmi et al. "Sensorless direct torque control for PM-assisted synchronous motors with injection high-frequency signal into stator flux reference frame". In: *2017 IEEE International Symposium on Sensorless Control for Electrical Drives (SLED)*. 2017, pp. 139–144. DOI: 10.1109/SLED.2017.8078444.
- [27] E. Capecchi et al. "Position-sensorless control of the transverse-laminated synchronous reluctance motor". In: *IEEE Transactions on Industry Applications* 37.6 (2001), pp. 1768–1776. DOI: 10.1109/28.968190.
- [28] G. Pellegrino. *Vector control of IM drives - Laboratory of power converters and electrical drives*. Version English. Italy, Mar. 2020.
- [29] O. Stiscia. "Position Sensorless Control of Multiphase PMSMs". MSc thesis. Politecnico di Torino, 2019.
- [30] M. Fatu et al. "I-F starting method with smooth transition to EMF based motion-sensorless vector control of PM synchronous motor/generator". In: *2008 IEEE Power Electronics Specialists Conference*. 2008, pp. 1481–1487. DOI: 10.1109/PESC.2008.4592146.

-
- [31] M. Wang et al. “An optimized I-F startup method for BEMF-based sensorless control of SPMSM”. In: *2017 IEEE Transportation Electrification Conference and Expo, Asia-Pacific (ITEC Asia-Pacific)*. 2017, pp. 1–6. DOI: 10.1109/ITEC-AP.2017.8080874.
- [32] C. L. Baratieri and H. Pinheiro. “An I-F starting method for smooth and fast transition to sensorless control of BLDC motors”. In: *2013 Brazilian Power Electronics Conference*. 2013, pp. 836–843. DOI: 10.1109/COBEP.2013.6785212.
- [33] M. Fatu et al. “I-F starting method with smooth transition to EMF based motion-sensorless vector control of PM synchronous motor/generator”. In: *2008 IEEE Power Electronics Specialists Conference*. 2008, pp. 1481–1487. DOI: 10.1109/PESC.2008.4592146.
- [34] ABB. *EC Titanium integrated motor drive*. URL: <https://new.abb.com/motors-generators/nema-low-voltage-ac-motors/variable-speed-ac/ec-titanium-integrated-motor-drive> (visited on 03/13/2021).
- [35] P. Pescetto and G. Pellegrino. “Sensorless magnetic model and pm flux identification of synchronous drives at standstill”. In: *2017 IEEE International Symposium on Sensorless Control for Electrical Drives (SLED)*. 2017, pp. 79–84. DOI: 10.1109/SLED.2017.8078434.